NASA CR-175155

SQ1

Final Report NASA Grant NAG-5-160

Remote Sensing of Floe Size Distribution and Surface Topography

D. A. Rothrock
A. S. Thorndike

Polar Science Center
University of Washington
Seattle, Washington 98195

Remote Sensing offers promise for studying sea ice conditions and the processes which change them. At present, there is too little common ground between remotely observable data and the quantities described in sea ice models. Our interest is in identifyimng measurements which can be made from satellites and which describe properties relevant to the balances of mass, heat and momentum of the ice cover. As a prerequisite, we wish to describe the random spatial structure of sea ice and its field of motion, so that adequate sampling strategies can be devised.

The research performed under this grant has been focussed on the piece-like structure of the ice pack, as described by the distribution of floe sizes. Objectives were 1) to clarify how the several useful definitions of floe size distribution are interrelated, 2) to consider the practicality of different measurement techniques, 3) to make measurements of typical distributions, and 4) to investigate the effect of sample size on the sampling error.

These objectives have been accomplished. The results are contained in a paper daringly entitled "Sea Ice Floe Size Distribution" and attached here as Appendix I. Summertime distributions of $N(\rho)$, the number of floes per unit area with diameter no smaller than ρ, behaves roughly as ρ^{α} with α ranging from -1.7 to -2.5. The sampling theory gives the variance of an estimate for the fraction g of a test area with diameter D covered by floes of diameter d as $g(1-g)N^{-1}$, where $N \approx (D/d)^2$ can be thought of as the number of independent samples in the test area. This relationship and similar ones for other test regions have been copnfirmed by measurements of sea ice images: LANDSAT visual images, U-2 aerial photgraphs, and a mosaic of NASA aerial photographs.

The basic procedures and theoretical facts are in hand for measuring floe size distribution. Different distributions can be defined and interrelated. Distributions have been measured for several stages of break-up--all of which show distinct floes. The extension to winter conditions where floes are not well defined should be pursued; a useful approach would be a study of lead geometries. Another useful step would be the application of these measurement techniques to many images of sea ice to observe the

seasonal and regional variability of floe size distribution.

The sampling theory devised for floe size distribution has application to any problem involving spatial sampling. It was applied to the sampling of ice thickness distribution, as expounded in the paper "Ice Thickness Distribution--Theory and Measurement" attached as Appendix II. The principle result is that for thick ice, samples further apart than about a hundred meters are independent, while independent samples of thin ice (thinner than one meter) must be over a kilometer apart.

The velocity field of sea ice is demonstrably the movement of rigid pieces. The consequences of this on the spatial statistics of the field are summarized in the paper "Kinematics of Sea Ice" attached as Appendix III. Included is the description of a model of the piecewise rigid body motion and its effect on the estimation of open water formation and ridging from a "large scale" measurement of deformation. The pieces are taken to be defined by a random set of lines (a Poisson field) with an average piece size of 16 km, taken from synthetic aperture radar data of Hall and Rothrock (1981). The differential movement of the pieces is given a Gaussian distribution. Many realizations of these pieces and their motion are simulated. For each, the total opening and closing at the floe boundaries is plotted versus a "large scale" estimate of deformation made from the velocity at three points. Each realization gives one data point. The scatter in the data points is several hundred percent and shows how poorly a three point strain rate estimate allows us to determine the actual small scale opening and closing.

RECOMMENDATIONS FOR FUTURE WORK

Floe size measurements should be extended into winter. The most attractive approaches are the study of the branching geometries of leads and the identification of pieces through their motion rather than their appearance. It would be useful, at this stage, to measure floe size distributions from a variety of ice conditions, and to begin to observe the spatial and temporal variability of this property of sea ice.

Further work, currently in progress, is aimed at direct observation of local (small scale) opening and closing from high resolution velocity field obtained from SAR imagery. SAR can also provide a better understanding of the statistics of the rigid body motion of pieces: for instance, whether their rotation and translation depends on floe size.

REFERENCE

Hall, R.T. and D.A. Rothrock (1981) Sea Ice Displacements from Synthetic Aperture Radar, *Journal of Geophys. Res., 86,* 11078-82.

PUBLICATIONS ISSUED DURING THIS GRANT

D. A. Rothrock and A. S. Thorndike, Sea Ice Floe Size Distribution, submitted to *Journal of Geophys. Res.*, attached as Appendix I.

D. A. Rothrock, Ice Thickness Distribution--Measurement and Theory. NATO Advanced Study Institute, Maratea, Italy; September 1981. In *The Geophysics of Sea Ice,* N. Untersteiner, editor. (In preparation, Plenum Publishing, New York.) Attached as Appendix II,

A. S. Thorndike, Kinematics of Sea Ice. NATO Advanced Study Institute, Maratea, Italy; September 1981. In *The Geophysics of Sea Ice,* N. Untersteiner, editor. (In preparation, Plenum Publishing, New York.) Attached as Appendix III.

APPENDIX I

SEA ICE FLOE SIZE DISTRIBUTION

by

D. A. Rothrock and A. S. Thorndike

Sea Ice Floe Size Distribution*

by

D. A. Rothrock and A. S. Thorndike
Polar Science Center
University of Washington

Abstract

Sea ice is broken into floes whose diameters range from meters to a hundred kilometers. This fragmentation affects the resistance of the ice cover to deformation and the melting at floe sidewalls in summer. Floes are broken by waves and swell near the ice edge, and, throughout the pack, by isostatic imbalances, thermal cracking, winds and currents. In winter, they are welded together by freezing.

Floe size can be measured by several properties p – for instance, area or mean caliper diameter. Two definitions of floe size distribution seem particularly useful: $F(p)$, the fraction of area covered by floes no smaller than p; and $N(p)$, the number of floes per unit area no smaller than p. A theorem from stereology states that $F(p)$ can be measured by sets other than areas, such as the fraction of a line or of a point set covered by floes no smaller than p. If N behaves like ρ^{α} for small ρ, where ρ is mean caliper diameter, α must be greater than -2 so that the small floes occupy finite area. If $-2<\alpha<-1$, the perimeter of small floes is infinite.

Several summertime distributions have been measured. On a log-log graph, their slopes (local values of α) range from -1.7 to -2.5. One distribution follows a power law; the others have steeper slopes for larger floes, and more gradual slopes for smaller floes. Another sampling strategy is to measure the lengths of line segments on floes. The distribution of these chord lengths is equivalent to the distribution of floe diameters.

The variance of an estimate of the fraction g of area covered by floes in any size range is $g(1-g)K^{-1}$, where K is the equivalent number of independent samples. K can be found from the autocovariance of the indicator function for the chosen size range. For line sampling of a narrow range of floe diameters, K is the ratio of the sample length to the floe diameter.

§1. Introduction

The sea ice covering the Arctic Ocean is not a uniform continuous sheet like the ice that might cover a small lake. Instead it has irregular top and bottom surfaces and is broken into distinct pieces, called floes. In the summer these floes are easily identified in remote images of the ice pack such as Figure 1: they are somewhat rounded in shape and are separated from each other by a lacey region of open water. They have diameters

---

* Submitted to *Journal of Geophysical Research*

ranging up to 100 kilometers. In the winter, floes still exist but they are less easily identified. Then the ice pack appears to be highly fractured, but the cracks, called leads, often cannot be resolved where the floes are actually in contact. To make matters worse, floes are constantly being "welded" together as new ice forms in the leads that separate them.

The division of the ice pack into floes affects its large scale geophysical properties. It seems likely, for instance, that the way the ice pack deforms in response to forces applied by the winds and the currents and at the coastline is controlled more by the geometry of the pack than by the material properties of sea ice. In this paper we discuss some of the geometric properties of the ice pack including the sizes and shapes of the ice floes, the arrangement of floes in space, and the abundance of floes of various sizes.

Physical processes that determine the floe geometry include: failure under horizontal forces applied by the winds and currents, failure during isostatic adjustment, thermal cracking, flexural failure in the presence of ocean swell, melting around the perimeter of floes, and abrasion with adjacent floes. These processes break large floes into little ones and cause floes to decrease in size. During the freezing season these processes are roughly balanced by the tendency of adjacent floes to be welded together. At present it is not known which processes are most important. Perhaps an understanding of the geometry of floes and how the geometry changes during the annual cycle will stimulate research on the governing physical processes. In any event, an understanding of the geometry of the ice pack is of interest in its own right for a number of practical applications associated with transportation in ice-covered seas and with the design of offshore structures intended to survive in the presence of ice.

The first section of this paper defines the floe size distribution, clarifying the notions of "size" and "distribution". The second section describes techniques for measuring the floe size distribution. A sampling theory in Section 3 indicates how many measurements must be taken to resolve the floe size distribution to a specified accuracy. Some measurements that test the sampling theory and others that illustrate floe size

distributions of different ice covers are presented in Section 4.

Measurements are presented primarily to illustrate points of technique or approach, and to indicate the range of distributions in different seasons. These have been made from three sources:

1) an aerial photographic mosaic of the region of the Arctic Ice Dynamics Joint Experiment (AIDJEX), 18 August 1975 (Hall, 1979), reproduced here as Figure 1,
2) part of a LANDSAT summer image, 185 km x 155 km, 18 August 1973 (No. E-1391-22283),
3) four U-2 aerial photographs of areas about 30 km on a side, taken June 21, 1974 (flight No. 74-101; frames 9635, 9637, 9639, and 9641).

The only other published observations we are aware of are in Weeks et al. (1980). Those measurements were made from airborne X-band side-looking radar data. We also mention a project currently underway at the Scott Polar Research Institute to measure floe size distribution near the ice edge from satellite imagery (A. Cowan, personal communication). Other work on this topic is reported by Losev (1972).

§2. Floe Size

Let $P(x,y,t)$ represent some measurable scalar property of the ice pack at the location (x,y) and at time t. In other contexts one might take P to be the ice thickness, the surface temperature, or some other local variable. But for our purposes we will consider P to be related to the size of the floe covering the point (x,y) at time t. If no floe covers the point, we take $P = 0$. Several measures of size are of interest:

1) area: The area of the x,y plane covered by the floe in question.
2) diameter of the largest inscribed circle: This is not as useful a measure of size as the total area of the floe, because it is not particularly easy to measure.
3) mean caliper diameter: Imagine calipers consisting of two parallel lines. A caliper diameter is the distance between the lines when each touches one side of the floe without penetrating the interior. The average of these readings as the

calipers are rotated through all orientations is the mean caliper diameter.

4) perimeter: The length of the curve defining the floe boundary, assuming the curve is smooth and its length finite. This quantity may be related to melting on the sidewalls of floes.

We now show that these properties are highly correlated so that a measurement of any one property gives an approximate value of any other. To study the relations between properties we selected the AIDJEX summer mosaic and digitized the perimeters of all floes with diameters over about one kilometer (Figure 2). All of the properties defined above were calculated for these 782 floes. The distribution of area/(mean caliper diameter)^2, for example, is shown in Figure 3. Subsamples of 45 large floes and 379 small floes have substantially the same distribution.

Table 1 summarizes these relationships; for example, a floe with a mean caliper diameter ρ has an area of $0.66\,\rho^2 \pm 0.05\,\rho^2$. Note how closely the relationship

Table 1. Statistics on certain ratios of floe properties

	Disc	Floes (Summer Mosaic)		
		Mean	Standard Deviation (σ)	σ/Mean
$\frac{\text{Area}}{(\text{Mean Caliper Diameter})^2}$	$\frac{\pi}{4} = 0.785$	0.66	0.05	0.08
$\frac{\text{Inscribed Circle Diameter}}{\text{Mean Caliper Diameter}}$	1	0.77	0.09	0.12
$\frac{\text{Perimeter}}{\text{Mean Caliper Diameter}}$	$\pi = 3.14$	3.17	0.04	0.01
$\frac{\text{Area}}{(\text{Inscribed Circle Diameter})^2}$	$\frac{\pi}{4} = 0.785$	1.14	0.21	0.18
$\frac{\text{Perimeter}}{(\text{Inscribed Circle Diameter})^2}$	$\pi = 3.14$	4.19	0.54	0.13
$\frac{\text{Area}}{(\text{Perimeter})^2}$	$(4\pi)^{-1} = 0.080$	0.065	0.005	0.08

$$\text{perimeter} = \pi \cdot \text{mean caliper diameter}$$

is satisfied. This expression is exact for any convex shape (Miles, 1978); a small concavity adds perimeter without altering the mean caliper diameter. The floes in this sample were in an intermediate stage of break-up. Floe shapes at the end of the melt season and in winter may be slightly different.

§3. Floe Size Distribution

Within some geographic region S (e.g., the Beaufort Sea) at some instant t (e.g., the first day of August), we consider the scalar property P to be a random function of space

$$P(x,y;t) \quad (x,y) \in S \, , \, t \in T \quad .$$

The observed function can be thought of as having been drawn at random from an ensemble consisting of all possible functions.

Any particular realization of P contains a full description of the P-geometry. In general, this geometry is very complicated, and much of it is irrelevant since it would not be repeated in different realizations. Our aim is to define statistical properties of the P-geometry that are common among different realizations and therefore describe the ensemble from which the realizations are drawn. Many more realizations of ice floe geometry will have to be studied before this goal can be reached. The present emphasis is to develop the general statistical concepts, not to document the full range of possible geometries.

We assume that the process is ergodic in whatever statistic is of interest to us. This means that one realization over a sufficiently large region S can teach us all we could learn by looking at numerous realizations.

Fractional Area

Suppose P is a property of an ice floe, so that P is constant over any particular floe. Then one can define the fractional area F in S covered by floes for which the property P is no less than p. Formally, use the Heavyside function $H(q) = 1$ if $q \geq 0$, and 0 if $q < 0$,

to write

$$F(p,S) = \frac{1}{S}\int_S\int H[P(x,y)-p]\,dx\,dy \quad . \tag{1}$$

S denotes both a region of the plane and its area without confusion. This definition avoids problems with "edge effects". If a floe with $P = p_0$ lies partially in S, only that part of its area within S is counted, but the value of p_0 pertains to the whole floe. $F(p,S)$ is a decreasing function of p. If p is a property that cannot be negative, then

$$\lim_{p\to 0} F(p,S) = F(0^+,S)$$

is the concentration of ice. $F(0,S)$ equals unity.

Thus far, S has been taken to be an area, but one might choose to sample floe sizes by some other set of lower dimension: either a line drawn through the image, or a set of regularly or randomly placed points. Sampling in such sub-spaces is called stereology and has countless applications. Early papers, for instance, concern estimating corpuscles in tissue and particulates in minerals (Wicksell, 1925; Nicholson, 1970). The subject contains a theorem that shows how measurements from different sample spaces are equivalent (Miles, 1978). The theorem states that if some subset U of S is selected, and $U' \subset U$ is the subset of U for which P exceeds p, then the ratio of the measure of U' to the measure of U is, on average, equal to $F(p,S)$

$$E\frac{\mu(U')}{\mu(U)} = F(p,S) \quad ,$$

where E denotes the expected value or ensemble average operator, and μ is the appropriate measure (the number of points, the length of line or the area).

Number density

A second way to describe the distribution of floe size is to find the number of floes per unit area of a region S for which P is no less than p

$$N(p,S) \quad .$$

Again, edge effects are best handled by counting the fraction of a floe's area contained in S, while retaining the value P of the whole floe. $N(p,S)$ is a decreasing function of p.

The total number of floes in S is $S \cdot N(0,S)$, which may be finite or infinite.

The number of floes larger than p and the fractional area covered by floes larger than p are related by

$$F(p,S) = -\int_{p}^{\infty} \alpha(\tilde{p}) dN(\tilde{p})$$

where $\alpha(p)$ is the area of a floe with property p (taken, say, from Table 1), and $-dN(\hat{p})$ is the number of floes with $\hat{p}<P<\hat{p}+d\hat{p}$. Use of one rather than the other is a matter of choice. The advantages of F are its bounded behavior for small p and its appearance in the fundamental theorem of stereology.

It might seem useful to consider the total number of floes larger than some cut-off p_0, $N(p_0,S)$ and to define the fraction of these floes larger than p

$$Q(p,p_0)=\frac{N(p)}{N(p_0)} \quad , \quad p \geq p_0 \quad .$$

Q is a cumulative probability function which increases to unity as p decreases to p_0. Its usefulness is limited, because the information about how densely the floes are packed in space has been lost, and because Q depends on p_0 as strongly as on p. If we envision picking floes at random, this probability function assigns each floe equal probability, whereas the quantity F, taken as a cumulative probability, weights each floe (and the open water) by its area.

Power law distributions.

Consider the distribution of mean caliper diameter ρ. For small ρ, N can behave like ρ^{α}, $\alpha \leq 0$ with $\alpha=0$ corresponding to the case of a finite number of floes in S. For $\alpha<0$, the number of floes smaller than any finite ρ_0 is infinite. Of course, the total area of such floes must remain finite

$$-\int_{0}^{\rho_0} \rho^2 dN = -\alpha \int_{0}^{\rho_0} \rho^{\alpha+1} d\rho < \infty$$

which is satisfied only for $\alpha>-2$. The total perimeter of the floes is proportional to the integral of ρdN, which is finite only when $\alpha>-1$. The three possible cases are:

$\alpha = 0$,	finite number of floes,
$-1<\alpha<0$,	infinite number of floes, finite perimeter,
$-2<\alpha<-1$,	infinite number of floes. infinite perimeter

Over the range for which the power law holds, the floe geometry has a certain self similarity

$$\frac{N(\rho)}{N(k\rho)} = q(k) \quad .$$

That is, for small floes, floes of a fixed size ratio occur in numbers of a fixed ratio. In this case there is no natural length scale to the geometry; provided that we choose a sub-scene which has small scale structure and does not fall entirely on a single floe, the small scale structure looks the same under arbitrary magnification. It is a common experience to confuse sea ice images with quite different scales, as in Figure 4, and that's why. Self similarity is illustrated by the Apollonian gasket in Figure 5, which is characterized by a power law distribution $N \sim \rho^{-1.807}$.

Exponential distributions.

A construction with quite different properties is shown in Figure 6. It is called a Poisson field, because the perpendicular distances from the (randomly oriented) lines to an arbitrary origin are distributed as a Poisson process (Solomon, 1978). Unlike the Apollonian gasket, it has a finite number of pieces in a finite region S. Circles inscribed in the pieces are distributed exponentially

$$N(\rho) = N(0)e^{-\rho/\lambda}$$

where ρ is circle diameter, and λ is the length scale of the pieces. The Poisson field bears only a slight resemblance to winter ice, and none to summer ice; the infinite length of the construction lines precludes there being many small floes in the space surrounded by a few large floes. We do not expect to observe exponential distributions in nature.

Techniques and observations.

One technique we tried involved the use of a set of discs, graduated in size from 3 mm up to 2.5 cm, corresponding to floes with diameters between about 1 and 10 km. Beginning with the largest disc, one can identify all the floes into which the disc fits. These floes have an inscribed circle diameter δ no smaller than the disc diameter. Working with k discs, one can establish k points (N,δ) of the number distribution of inscribed circle diameter. We used five discs. Floes more than half in the test area were counted. The method is appealing in its simplicity and is sufficiently accurate to distinguish the range of distributions occurring in nature.

This method was applied to the LANDSAT image and four U-2 photographs, the distributions for two of which are shown in Figure 7. Inscribed circle diameter was converted to mean caliper diameter ρ, using $\delta = (0.77)\rho$ from Table 1.

Another technique is to digitize each floe boundary on an x,y digitizing tablet by tracing a cursor around the boundary of each floe. Some precaution must be taken to digitize all floes in the chosen size range and lying even partially within the test area. Each floe is represented by the coordinates of twenty to fifty points around its boundary, from which one can easily calculate all floe properties.

This method allows one to treat edge effects without error, counting the (areal) fraction of a floe within the test area while measuring the floe property of the whole floe. The test area for the AIDJEX summer mosaic is the box shown in Figures 1 and 2. Digitizing requires equipment and some set-up time – for instance, writing programs to compute floe properties – but in an operational mode, this method is probably as quick as using disc cutouts and provides accurate measurements of all floe properties.

The AIDJEX summer mosaic was measured in this manner. Its number distribution is shown in Figure 7, and its fractional area distribution in Figure 8.

The mosaic and the LANDSAT image are data from the same geographic area in mid-August, two years apart. The difference between the two distributions (in Figure 7) is evidence of considerable interannual variability.

Striking spatial variability is also present. The distributions denoted by U2-35 and U2-39 in Figure 7 were observed at the same time from regions only 50 km apart. Further, one can interpret the ice in U2-39 as being a broken version of the ice in U2-35. To the extent that this interpretation is valid, we see that only the large floes broke; U2-39 has fewer 10 km floes but more 1 km floes.

§4. Chord length distribution

In winter, when it is difficult to identify floes and assign values of P, piece sizes can be characterized by the distribution of chord lengths. At each point x on a random line, R, assign a chord length $C(x)$ of the longest segment containing x and lying on a single piece of ice.

Either end of the chord touches a crack or lead. From R select a random test segment S of length L, count the number of chords within S for which C is no less than c, and divide by L to define the chord distribution $M(c)$. For a chord only partly in S, count the fraction of its length in S, but assign a value C equal to its total length.

The chord and floe size distributions are closely related. In this instance, take the floe property to be the mean caliper diameter ρ. If a rectangular area with sides a and b is sampled by a test line S parallel to side b, we have that

$$\left\{\begin{array}{c}\text{number of chords}\\ \text{between } c \text{ and } c+dc\end{array}\right\} = \int_{\text{all diameters}} \left\{\begin{array}{c}\text{probability that chord is between } c \text{ and } c+dc,\\ \text{given that } S \text{ hits a floe of diameter } \rho\end{array}\right\} \cdot \tag{2}$$

$$\left\{\begin{array}{c}\text{probability that } S\\ \text{hits a floe with diameter } \rho\end{array}\right\} \cdot \left\{\begin{array}{c}\text{number of floes with}\\ \text{diameter between } \rho \text{ and } \rho+d\rho\end{array}\right\} .$$

Using the definition

$$G(c,\rho) = \text{probability } \{\, \text{chord} > c \,|\, S \text{ hits a floe with diameter } \rho \,\}$$

and the densities

$$m(c) = -\frac{dM}{dc} \quad \text{and} \quad n(\rho) = -\frac{dN}{d\rho} \quad ,$$

(2) becomes

$$b\, m(c)dc = \int_\rho \left\{-\frac{dG}{dc}dc\right\}\left\{\frac{\rho}{a}\right\}\{a\, b\, n(\rho)d\rho\}$$

or

$$m(c) = -\int_\rho \frac{dG(c,\rho)}{dc}\rho n(\rho)d\rho \quad . \tag{3}$$

For circular floes with

$$G = [1-\frac{c^2}{\rho^2}]^{1/2}$$

equation (3) is an Abel integral equation which can be inverted to give the diameter distribution in terms of the chord distribution

$$N(\rho) = \frac{2}{\pi}\int_{c=\rho}^{\infty} (c^2-\rho^2)^{-1/2}dM(c) \quad . \tag{4}$$

Parts of this development follow Ripley (1981, §9.4).

Figure 9 shows measurements of both $N(\rho)$ and $M(c)$ from the AIDJEX summer mosaic, and a calculation of $N(\rho)$ from $M(c)$ observations using (4). Measurements of $G(c,\rho)$ for real summer floes are shown in Figure 10.

§5. Sampling the floe size distribution

It may be inefficient or even impossible to determine the fractional area distribution F by measuring the area of each floe in a region R. In this section we discuss the errors that arise when F is estimated using a subset U of R. A general theory is presented and then applied to several specific sampling strategies where U is taken to be a box, a random straight line segment, or a regular lattice of points.

Let $P(x,y)$ be a measurable property at the point (x,y) and let Γ denote any condition on P. Define the indicator function $\Pi(x,y)$ to be 1 if P satisfies Γ and zero otherwise. For example, if P represents mean caliper diameter, and Γ the condition 1 km $< P <$ 2 km, the indicator function will take the value $\Pi = 1$ over all floes with diameters between one and two kilometers, and will be zero elsewhere. Use the symbol g to denote

the fractional area of R for which P satisfies Γ. With our earlier point of view that P is a random function, we have

$$g = \mu_R^{-1} \int_R \Pi(x,y)\, dR = \text{Prob } (P \text{ satisfies } \Gamma) \quad .$$

Here the measure of R, μ_R, is included to normalize g properly. The probability of g is assumed to be independent of x,y; any point in R has equal *a priori* probability of satisfying the condition Γ.

Now let $\hat{g}$ be an estimate of g based on the random subset U.

$$\hat{g} = \mu_U^{-1} \int_U \Pi(x,y)\, dU \quad . \tag{5}$$

We now show that the mean of $\hat{g}$ is g and show how the variance of $\hat{g}$ depends on the size of the sample U.

The mean and variance of $\hat{g}$.

Since P is a random function, so is Π. Π has the trivial probability density: Prob(Π=1) = g; Prob(Π=0) = $1-g$. Thus $E\Pi$ equals g. Then using (5), $E\hat{g}$ equals g.

From (5), we have

$$var\ \hat{g} = E(\hat{g}-g)^2 = E\left[\mu_U^{-1} \int_U \Pi(x,y)\, dU - g\right]\left[\mu_U^{-1} \int_U \Pi(x',y')\, dU' - g\right] \tag{6}$$

$$= \mu_U^{-2} \int_U \int_U R_\Pi(x,y,x',y')\, dU dU' \quad ,$$

where R_Π is the autocovariance function for the indicator function. Its properties are discussed in the next section. This equation describes how the variance of the estimator depends on the sample set U and on the way the floes satisfying the condition Γ are arranged in space, as characterized by R_Π.

The autocovariance of the indicator function.

The indicator function Π depends on the property P being studied and on the condition Γ. In another context, P might be associated with ice thickness and Γ with any narrow range of thicknesses (Rothrock, in press). But here we associate P with mean

caliper diameter and Γ with any narrow range of diameters. In both cases, Π has certain spatial structure that shows up in its autocovariance.

Consider the one dimensional analogy in which the line is broken into intervals of random lengths, and the property P is interval length. Let Γ be the condition $D < P(x) < D+\varepsilon$. Then $\Pi(x)$ is a random function of x taking the value zero for most x and the value 1 over intervals of length greater than D and less than $D+\varepsilon$. The notable structure of Π in this case is that all of its "up" segments have length D. For small ε the up segments will be rare and the intervals between them will have random lengths. The situation is approximately that of a single "up" segment of length D placed at random on a line segment of length $L \gg D$. To determine the autocovariance for this random function, note that

$$R_\Pi(a) = E[\Pi(x+a) - D/L] \cdot [\Pi(x) - D/L] = E\Pi(x+a)\Pi(x) - D^2/L^2 \quad .$$

The expression $E\Pi(x+a)\Pi(x)$ represents the probability that $x+a$ and x both lie on the random up segment that we denote by V. We have

$$\begin{aligned} E\Pi(x+a)\Pi(x) &= \text{probability}[(x+a) \in V \text{ and } x \in V] \\ &= \text{probability}(x \in V) \cdot \text{probability}[(x+a) \in V \mid x \in V] \quad . \end{aligned}$$

This last probability is evaluated by considering all possible locations that allow V to cover x, and the fraction of those that also cover $x+a$. Then $E\Pi(x+a)\Pi(x)$ is

$$\text{probability}(x \in V) \cdot \frac{\text{overlap of segments centered on } x \text{ and on } x+a}{\text{length of segment centered on } x}$$

$$= g \begin{cases} 1-|a|/D \ , & |a|<D \ , \\ 0 \quad , & |a|>D \ . \end{cases}$$

For large L, this is approximately $R_\Pi(a)$, but we adjust the amplitude so that the variance $R_\Pi(0)$ is $g(1-g)$, keeping R_Π zero for large a. Then

$$R_\Pi(a) \approx g(1-g) \begin{Bmatrix} 1-|a|/D \ , & |a|<D \\ 0 \ , & |a|>D \end{Bmatrix} \quad .$$

In two dimensions, a similar argument can be used to find $R_\Pi(\mathbf{x},\mathbf{x}') = R_\Pi(s)$ where s is the distance between $\mathbf{x}$ and $\mathbf{x}'$. Take the floes to be discs of diameter D, and again denote one rare disc by V. For V to cover $\mathbf{x}$, its center must lie within a circle of diameter D, centered on $\mathbf{x}$. We have that $E\Pi(\mathbf{x}')\Pi(\mathbf{x})$ is equal to the product of g and the fraction

$$\frac{\text{overlap of circles whose centers are a distance } s \text{ apart}}{\text{area of circle centered on } \mathbf{x}}$$

which is

$$2\pi^{-1}h\left(\frac{S}{D}\right) \quad \text{where} \quad h(x) = \begin{cases} \cos^{-1}x - |x|(1-x^2)^{1/2} , & |x|<1 , \\ 0 , & |x|>1 . \end{cases}$$

Again adjusting the variance, we have

$$R_\Pi(s) = g(1-g)2\pi^{-1}h\left(\frac{s}{D}\right) \quad . \tag{7}$$

Figure (11) allows comparison of equation (7) with observed autocovariance functions for three different narrow ranges of floe size.

Sampling by area

Returning now to the question of the variance of $\hat{g}$, consider the case where the sample set U is a box of side A. Then

$$var\ \hat{g} = A^{-4}\int_0^A\int_0^A\int_0^A\int_0^A R_\Pi(x,y,x',y')\,dxdydx'dy' \quad .$$

Make the coordinate change $x',y' \to s,\theta$ with $s = [(x-x')^2 + (y-y')^2]^{1/2}$ and $\theta = \tan^{-1}(y'-y)/(x'-x)$. With s and θ fixed, the region for integration for x and y is the overlap of two boxes of side A whose lower left-hand corners are offset a distance s in the θ direction:

$$\begin{aligned} var\ \hat{g} &= A^{-4}\int_{s=0}^{\sqrt{A}}\int_{\theta=0}^{2\pi}\int_{x=0}^{A-s|\cos\theta|}\int_{y=0}^{A-s|\sin\theta|} R_\Pi(s)\,s\,ds\,d\theta\,dx\,dy \\ &= A^{-4}\int_0^{\sqrt{2}A}(2\pi A^2 - 8As + 2s^2)s\,R_\Pi(s)ds \quad . \end{aligned} \tag{8}$$

To illustrate the use of this result, substitute the approximate expression (7) for $R_\Pi(s)$ into (8) to obtain

$$var\,\hat{g} = g(1-g)2\pi^{-1}A^{-4}\int_0^{\sqrt{2}A}(2\pi A^2 - 8As + 2s^2)sh(\frac{s}{D})ds$$

$$= g(1-g)2\pi^{-1}D^2A^{-2}\int_0^{\sqrt{2}AD^{-1}}(2\pi - 8DA^{-1}\eta + 2D^2A^{-2}\eta^2)\eta h(\eta)d\eta \quad .$$

For $A \gg D$, this is roughly

$$var\,\hat{g} = g(1-g)(\frac{1}{4}\pi D^2)A^{-2} \quad . \tag{9}$$

In many equations that follow, the variance of $\hat{g}$ is proportional to $g(1-g)$:

$$var\,\hat{g} = g(1-g)K^{-1} \quad .$$

For M independent point samples (Bernoulli trials with probability of success equal to g), the constant of proportionality is simply $K = M$. For area sampling we have that $K \approx A^2/(\pi D^2/4)$ = (box area)/(disc area) which we can think of as an equivalent number of independent samples. If, for example, we wish to estimate g for a class of floes that are thought to cover about 0.10 of the area, and we want the estimate (5) to be good to ±0.02, then $var\,\hat{g} = (0.02)^2 = (0.1)(0.9)K^{-1}$, which implies $K = 225$. This can be achieved by selecting 225 point measurements separated widely enough to be independent or by measuring densely over a box of side $A = (\pi/4)^{1/2}K^{1/2}D$, roughly $K^{1/2}$ or 15 times the diameter of the floes in question.

Equation (8) was tested using the digitized AIDJEX summer mosaic. Using the measured autocovariance of the indicator function for a fairly narrow range of floe size, $var\,\hat{g}$ in (8) was evaluated for several values of A, as shown in the right-hand column of Table 2. An independent measure of the variance of $\hat{g}$ was obtained directly by choosing several different test areas of side A, measuring $\hat{g}$ in each one, and noting the mean and variance of the set of samples of $\hat{g}$. These are shown in Table 2, and confirm the theoretical results.

Table 2. Comparison of theory with measurement for variance of estimator $\hat{g}$, sampling floes in AIDJEX summer mosiac with boxes of side L

Small floes: $1 < \rho < 4.7$ km, g = 0.20

	Measurements from mosaic		Theory, Eq. (8)
L, km	number of samples	$\sqrt{var\ \hat{g}}$	$\sqrt{var\ \hat{g}}$
5	25	.22	.19
10	25	.15	.12
19	25	.09	.08
32	9	.07	.05
47	4	.05	.04
100			.02
200			.01

Large floes: $\rho > 13.5$ km, g = 0.21

	Measurements from mosaic		Theory, Eq. (8)
L, km	number of samples	$\sqrt{var\ \hat{g}}$	$\sqrt{var\ \hat{g}}$
5	25	.36	.32
10	25	.30	.29
19	25	.21	.20
32	9	.16	.14
47	4	.08	.10
100			.05
200			.03

Sampling along a line

Let U be a random line segment of length L. At each point along the line, the floe diameter (not the chord length) is determined and $\hat{g}$ is evaluated using equation (5). Then the variance is

$$var\,\hat{g} = L^{-2}\int_0^L\int_0^L R_\Pi(|x-x'|)dx\,dx' = 2L^{-2}\int_0^L (L-s)R_\Pi(s)ds \quad .$$

Using the form given above for R_Π and taking $L \gg D$, we get the approximation

$$var\,\hat{g} = g(1-g)4\pi^{-1}\int_0^1 (1-x)h(x\frac{L}{D})dx \approx g(1-g)\frac{D}{L} \quad , \quad L \gg D \quad . \tag{10}$$

Sampling on a regular lattice

When U is an $M \times M$ lattice of points with spacing Δ, the expression for the variance of $\hat{g}$ becomes

$$var\,\hat{g} = M^{-4}\sum_{i=1}^{M}\sum_{j=1}^{M}\sum_{k=1}^{M}\sum_{l=1}^{M} R_\Pi(S_{ijkl})$$

where S_{ijkl} is the distance between the ij and kl lattice points. The covariances $R_\Pi(S_{ijkl})$ can be thought of an an $M^2 \times M^2$ matrix of covariances between any pair of lattice points. The diagonal elements are simply $g(1-g)$. If Δ is chosen large enough so that the points are uncorrelated, then the non-diagonal elements are zero and

$$var\,\hat{g} = g(1-g)M^{-2} \quad . \tag{11}$$

For a smaller lattice spacing some of the non-diagonal covariances will be positive and the variance of $\hat{g}$ will increase.

To summarize, we estimate the fractional area covered by ice floes of a certain range of sizes using equation (5). The variance of this estimator can be found using the auto-covariance R_Π of the indicator function in equation (6) for any sampling strategy. The variance is inversely proportional to K, the equivalent number of independent samples, which is given by the approximations

area sampling: K ≈ area of sample / area of floes being considered

line sampling: K ≈ length of sample / diameter of floe

point sampling: K ≈ number of points separated by at least a floe diameter

§6. Conclusions

We have devoted this preliminary discussion of the floe size distribution of sea ice to questions of definition and of measurement, with emphasis on the errors which arise in estimating the distribution from a limited sample. Our preferred definition is the number distribution $N(\rho)$ giving the number per unit area of floes whose mean caliper diameter exceeds ρ. $N(\rho)$ increases as ρ decreases to zero. In some of the data sets we have examined, N behaves approximately like ρ^{α} with $-1.7 < \alpha < -2.5$, but we see no reason to expect a power law or any other simple analytical form to be valid for all ρ. We find changes in the distribution from year to year and from one region to another.

The theory given for the sampling errors is summarized in equations (9), (10) and (11). The central idea is this: the error in an estimate of the abundance of floes of area a in a sample of area A depends on the number of independent samples, which is roughly A/a.

The several floe properties related to floe size that we considered, mean caliper diameter, perimeter, area, chord length, diameter of inscribed circle, appear to be roughly equivalent. The choice of what property to measure may be made based on the kind of data and measuring systems available. For manual measurements, we recommend sampling the chord lengths along random lines.

The important geophysical problems are to relate the geometric properties of the ice pack to its mechanical and thermal properties, and to relate changes in the geometry to the mechanical and thermal forcing. Floe size, ice thickness, and surface roughness are three geometric properties which have been studied. Others of potential interest are the

widths, lengths and branching properties of leads.

§7. Acknowledgments

We are grateful to J. F. Nye for his discussions on this subject and to R. T. Hall who made many of the measurements. This work was supported by the National Aeronautics and Space Administration under Grant No. NAG-5-160 and by the Office of Naval Research under Contract No. N00014-76-C-0234.

References

Hall, R. T., Seasonal photo mosaics of the AIDJEX triangle. *AIDJEX Bulletin No. 39*, 79-84. University Press, University of Washington, Seattle, 1978.

Gorbunov, Yu. A. and L. A. Timokhov. Variability of degree of break-up (in Russian). *Tr. Arkt i Antarkt. N. Inst., 316*, 89-95, 1974.

Kheysin, D. E. Selection of algorithms for numerical evaluation of the distribution of ice floe dimensions and their concentration. *Problemy Arkt. i Antarkt., 45*, 87-93.

Losev, S. M. Area characteristics of ice cover. *Problemy Arkt. i Antarkt., 39*, 47-54, 1972.

Mandelbrot, B. B. *Fractals: Form, Chance and Dimension.* 365 pp., Freeman, San Francisco, 1977.

Miles, R. E. The importance of proper model specification in stereology. *Geometrical Probability and Biological Structures: Buffon's 200th Anniversary*, R. E. Miles and J. Serra, eds., Springer-Verlag, New York, 1978.

Nicholson, W. L. Estimation of linear properties of particle size distributions. *Biometrika, 57*, 273-297, 1970.

Ripley, B. D. *Spatial Statistics*, 252 pp., Wiley, New York, 1981.

Rothrock, D. A. Ice thickness distribution – measurement and theory. NATO Advanced Study Institute, Maratea, Italy, September 1981. *The Geophysics of Sea Ice*, N. Untersteiner, ed., in press, Plenum Publishing Corp.

Solomon, H. *Geometric Probability*, 174 pp., Soc. for Industrial and Applied Mathematics, Philadelphia, 1978.

Weeks, W. F., W. B. Tucker, M. Frank and S. Fungcharoen. Characterization of surface roughness and floe geometry of sea ice over the continental shelves of the Beaufort and Chukchi Seas. *Sea Ice Processes and Models.* R. S. Pritchard, ed., University Press, University of Washington, Seattle, 1980.

Wicksell, S. D. The corpuscle problem. A mathematical study of a biometric problem. *Biometrika, 17*, 84-89, 1925.

Figure Captions

Figure 1. Mosaic of aerial photographs of summer pack ice (Hall, 1979). The dark areas are open water between floes. The box measures 95 by 110 km.

Figure 2. Digitized floe boundaries in the summer mosaic (Figure 1).

Figure 3. The distribution of the ratios of area to squared mean caliper diameter.

Figure 4. Views of sea ice on two different scales. The frame on the left is about 26 km wide, that on the right, 2.4 km. The texture on the left of the high level image is due to clouds. Melt ponds can be seen in the lower altitude photograph.

Figure 5. An Apollonian gasket (from Mandelbrot, 1977). The disc sizes are distributed as a power law.

Figure 6. A Poisson field, illustrating a construction with an exponential distribution of piece sizes.

Figure 7. The cumulative number distribution of mean caliper diameter $N(\rho)$. For the solid lines, mean caliper diameter was directly measured; for the dashed curves, it was calculated from measured inscribed circle diameters.

Figure 8. The cumulative area distribution of mean caliper diameter $F(\rho)$ for the summer mosaic.

Figure 9. (above) The cumulative number distribution of mean caliper diameter $N(\rho)$ for the summer mosaic: (·) measured directly, and (+) calculated from measured chord distribution (solid line below). The solid chord distribution was smoothed from the actual observations (·).

Figure 10. The density of the ratio of chord to mean caliper diameter for the floes in the summer mosaic and for discs ($-dG/d\gamma$, where $\gamma = c/\rho$).

Figure 11. The autocovariance of the indicator function. The solid line is the theoretical expression (7) for rare discs. The symbols show observations from the digitized summer mosaic for several narrow ranges of diameters.

Figure 1. Mosaic of aerial photographs of summer pack ice (Hall, 1979). The dark areas are open water between floes. The box measures 95 by 110 km.

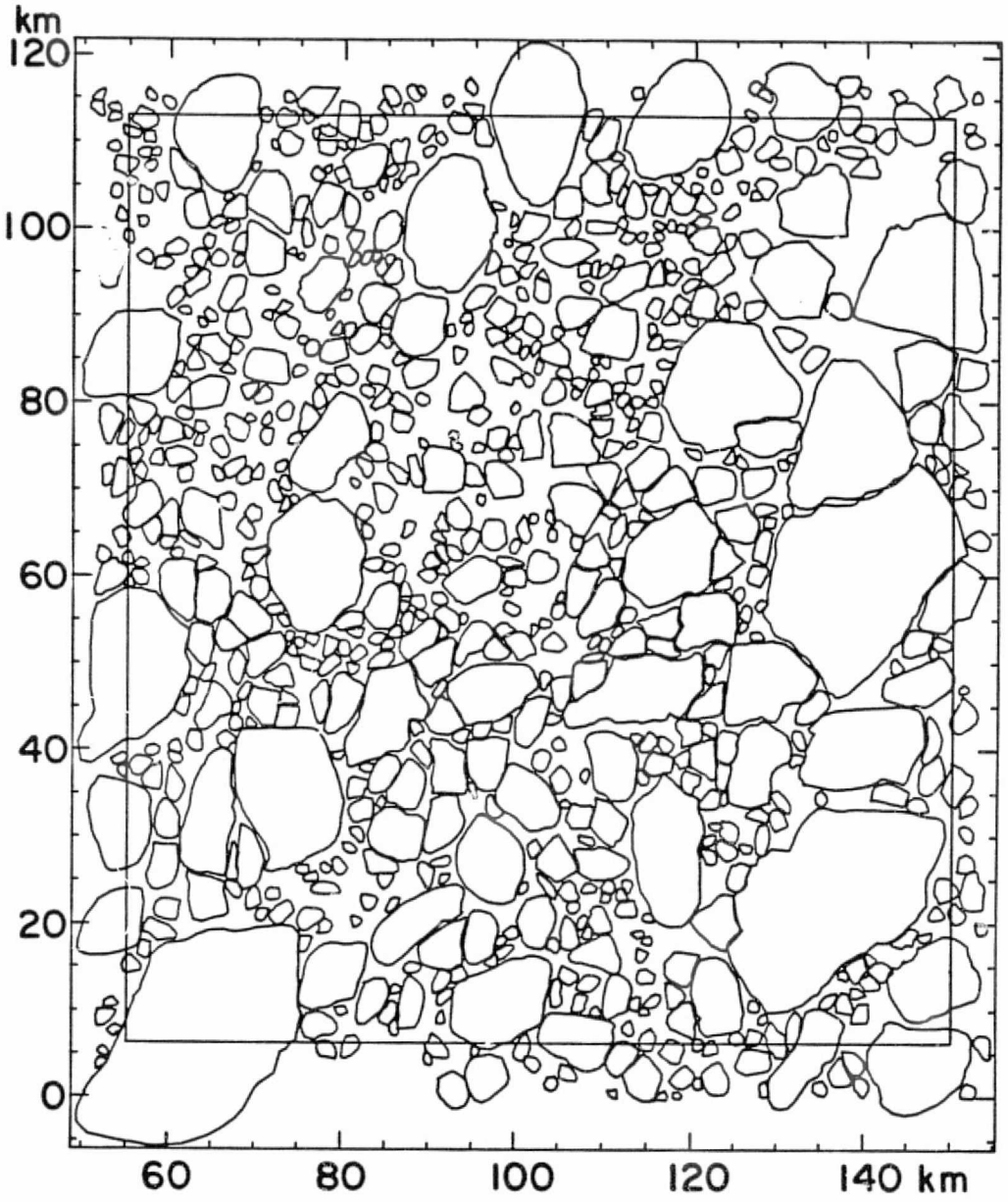

Figure 2. Digitized floe boundaries in the summer mosaic (Figure 1).

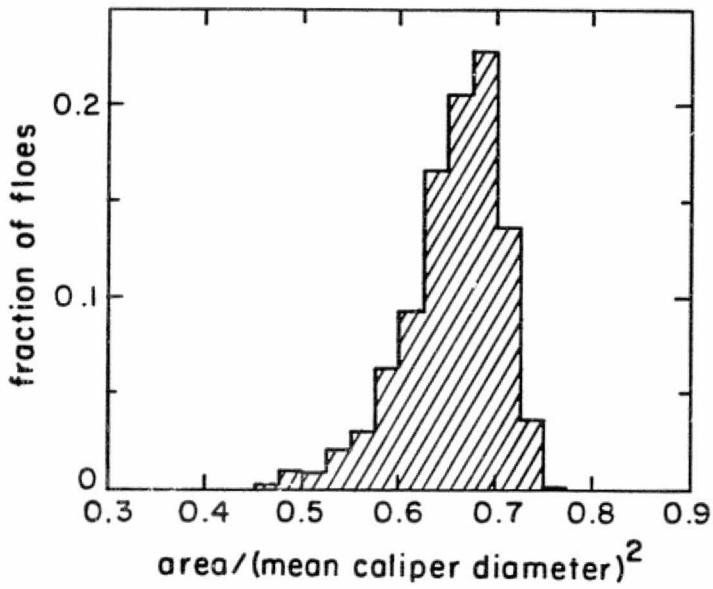

Figure 3. The distribution of the ratios of area to squared mean caliper diameter.

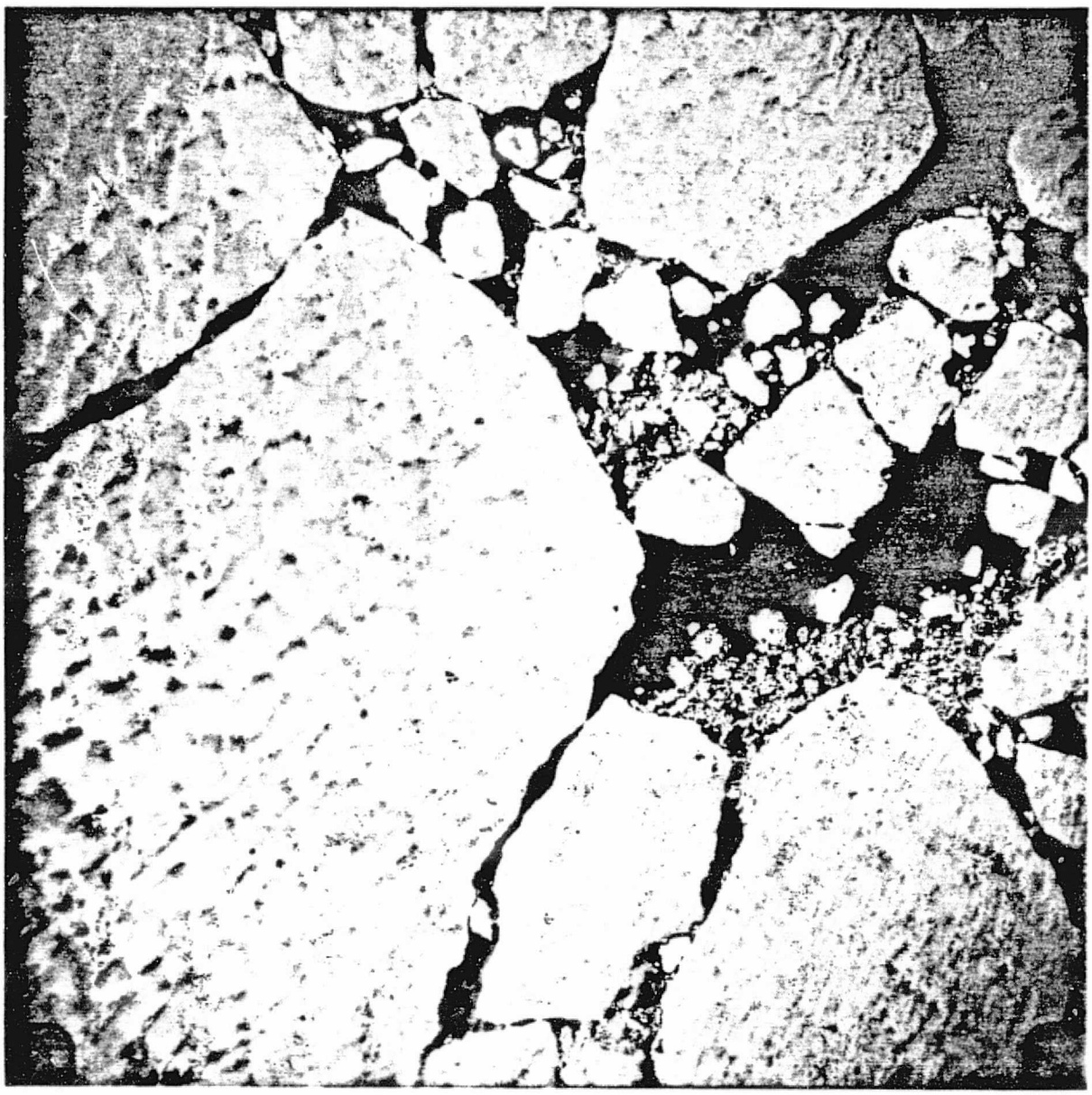

Figure 4a.

Figure 4a and 4b. Views of sea ice on two different scales. Frame 4a is about 28 km wide.. The texture on the left is due to clouds.

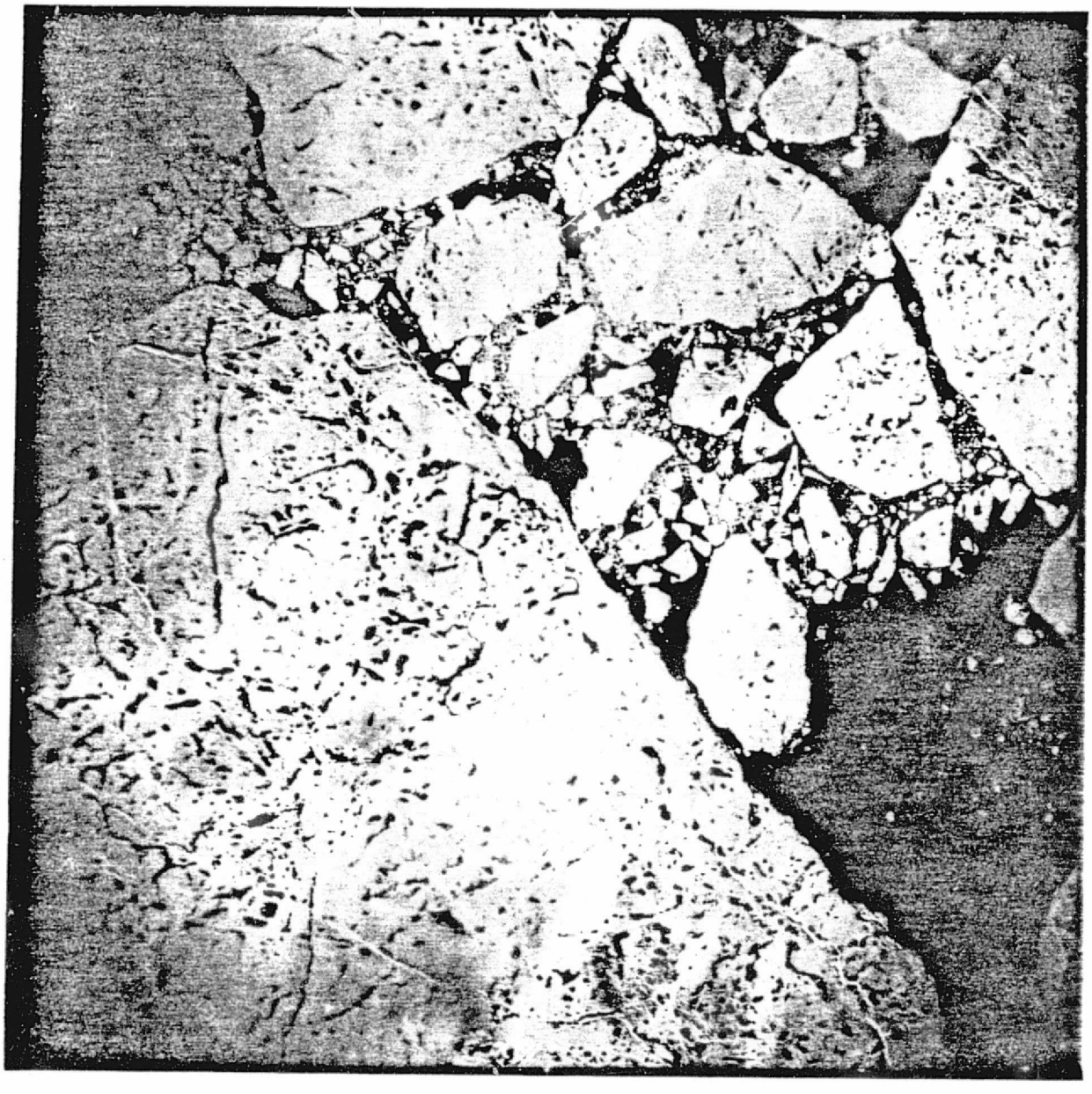

Figure 4b.

Figure 4a and 4b. Views of sea ice on two different scales. Frame 4b is about 2.4 km wide. Melt ponds can be seen in this photograph.

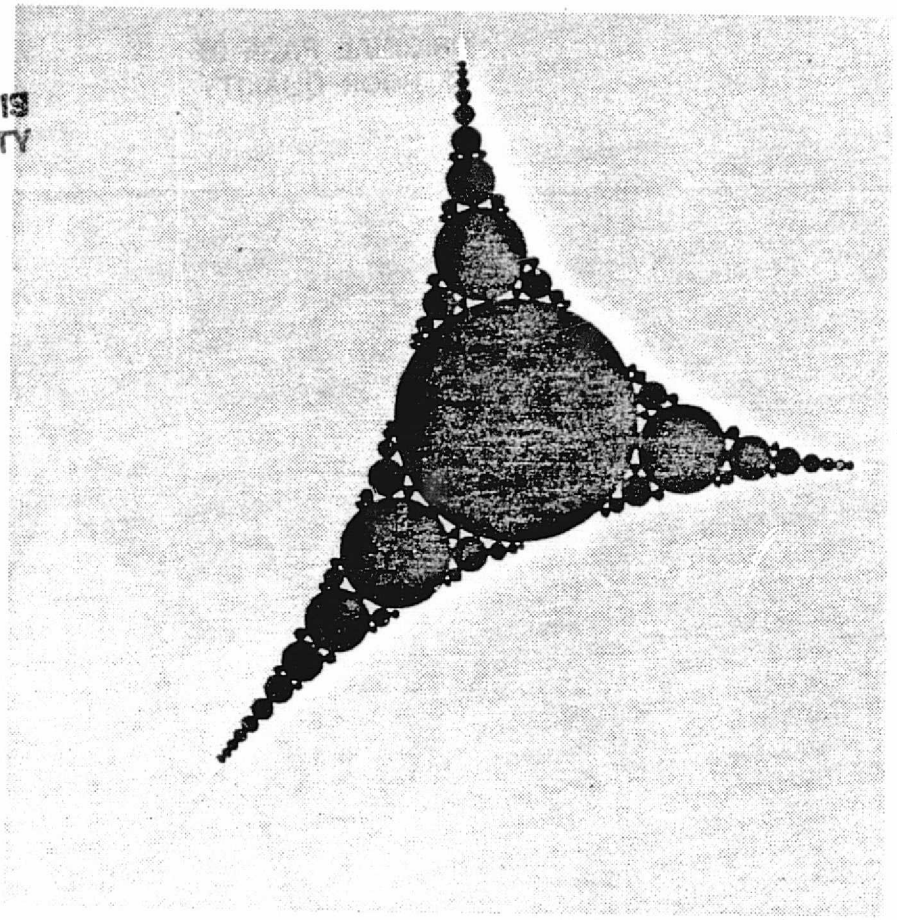

Figure 5. An Apollonian gasket (from Mandelbrot, 1977). The disc sizes are distributed as a power law.

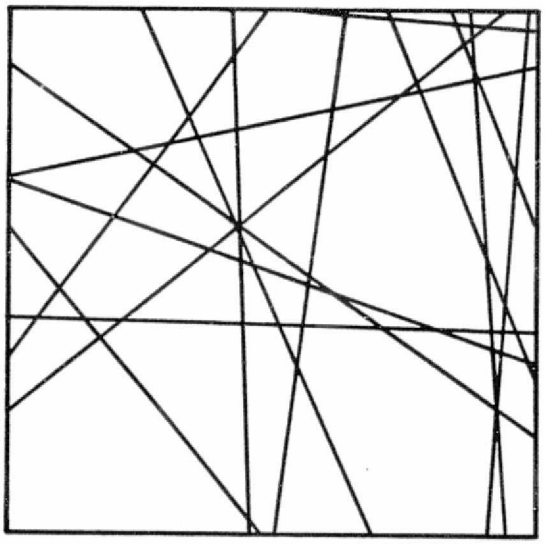

Figure 6. A Poisson field, illustrating a construction with an exponential distribution of piece sizes.

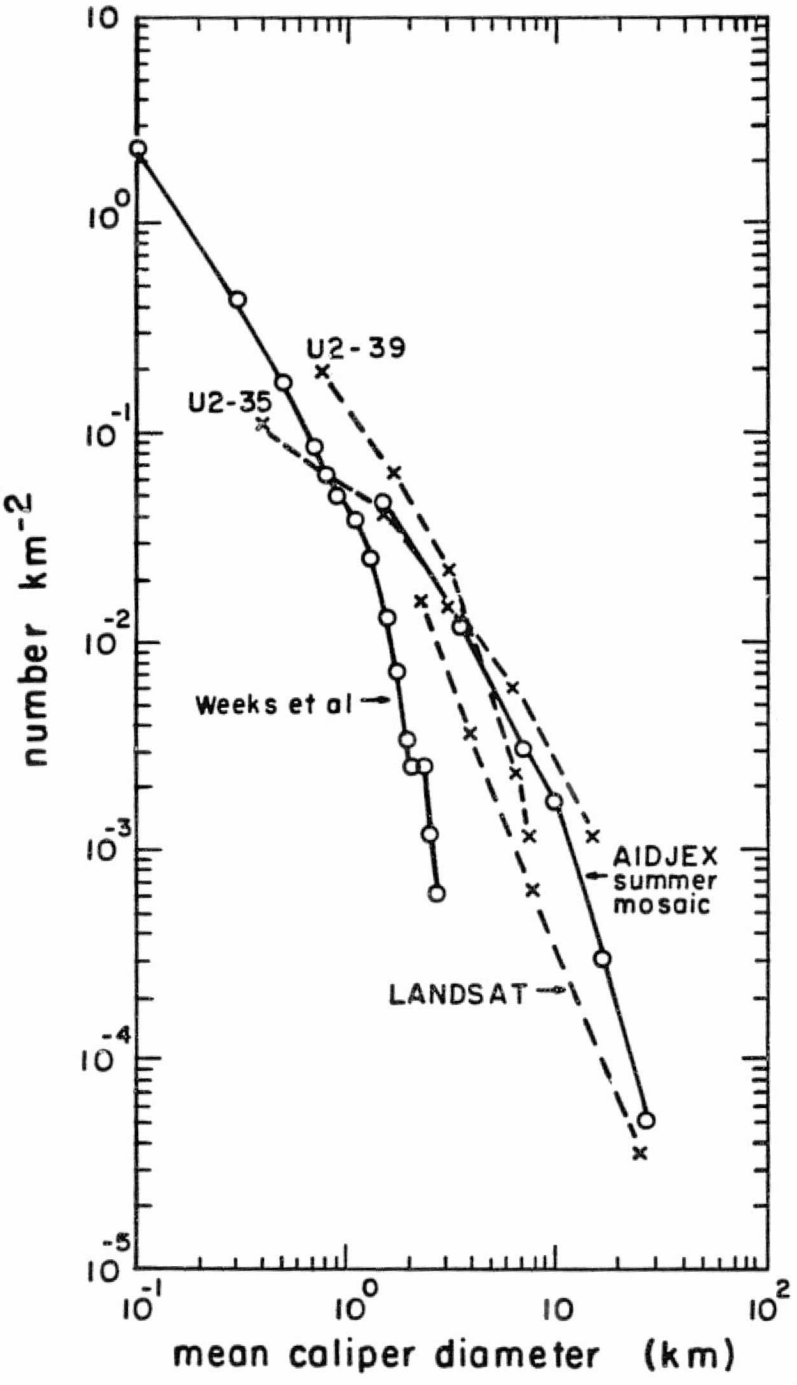

Figure 7. The cumulative number distribution of mean caliper diameter $N(\rho)$. For the solid lines, mean caliper diameter was directly measured; for the dashed curves, it was calculated from measured inscribed circle diameters.

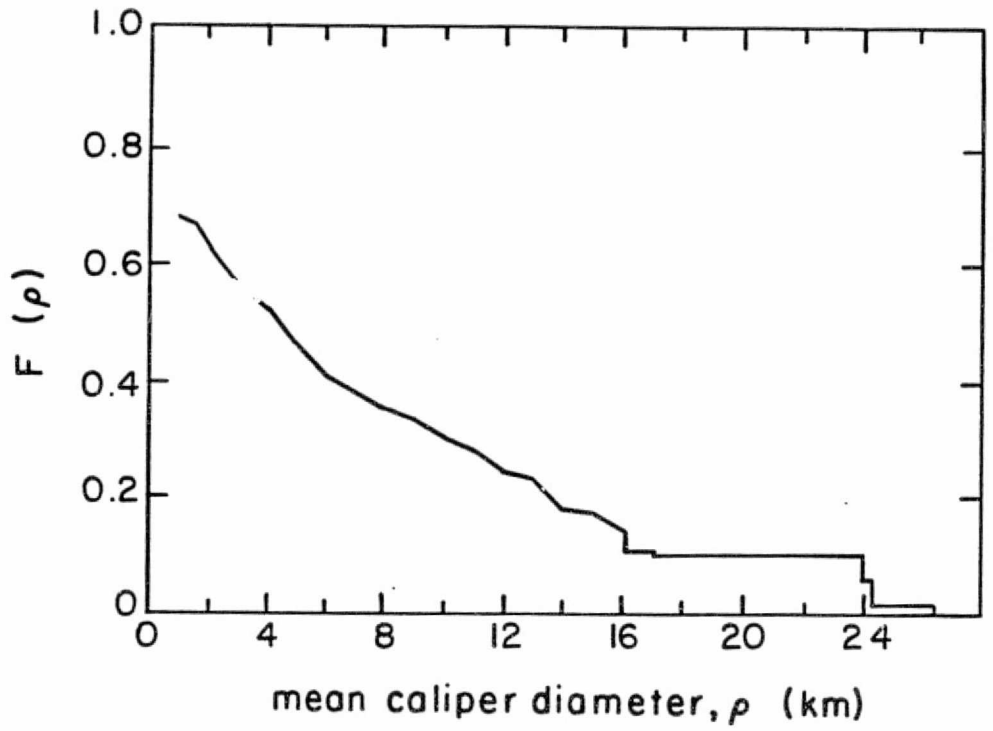

Figure 8. The cumulative area distribution of mean caliper diameter $F(\rho)$ for the summer mosaic.

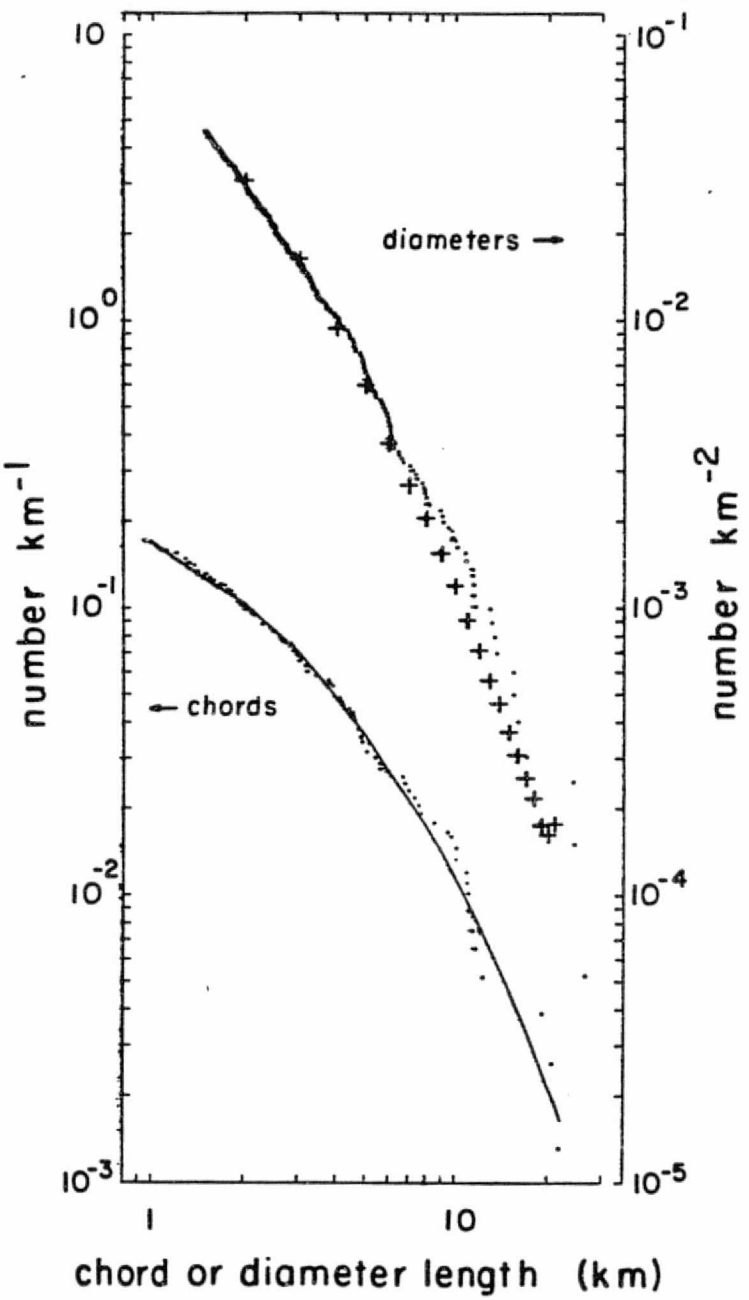

Figure 9. (above) The cumulative number distribution of mean caliper diameter $N(\rho)$ for the summer mosaic: (•) measured directly, and (+) calculated from measured chord distribution (solid line below). The solid chord distribution was smoothed from the actual observations (•).

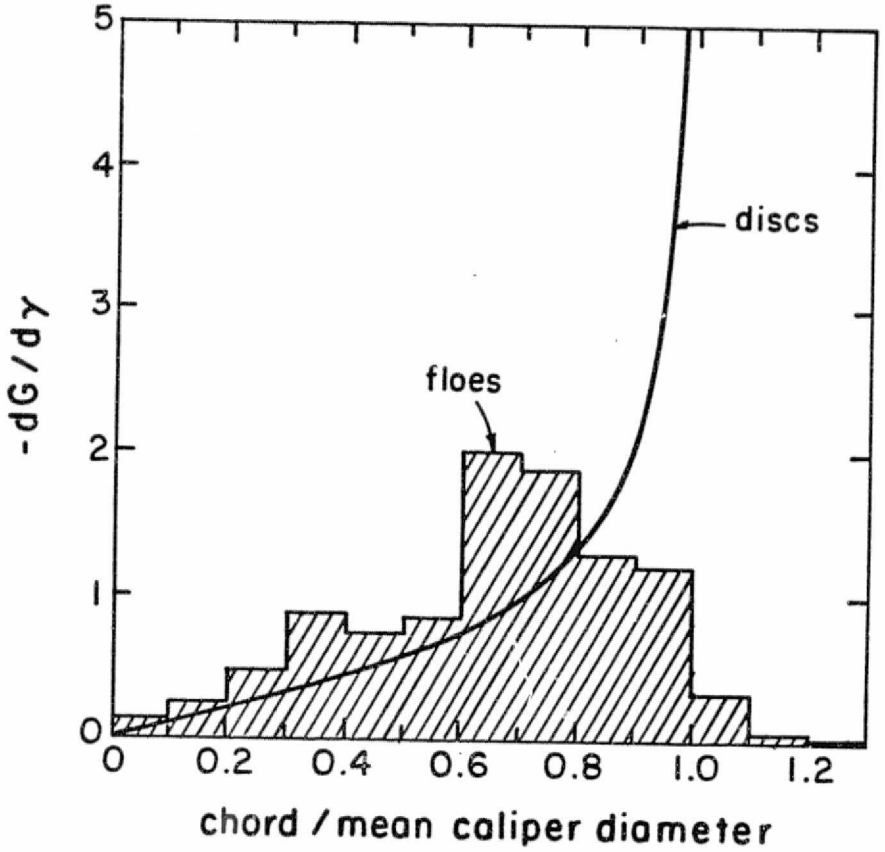

Figure 10. The density of the ratio of chord to mean caliper diameter for the floes in the summer mosaic and for discs ($-dG/D\gamma$, where $\gamma = c/\rho$).

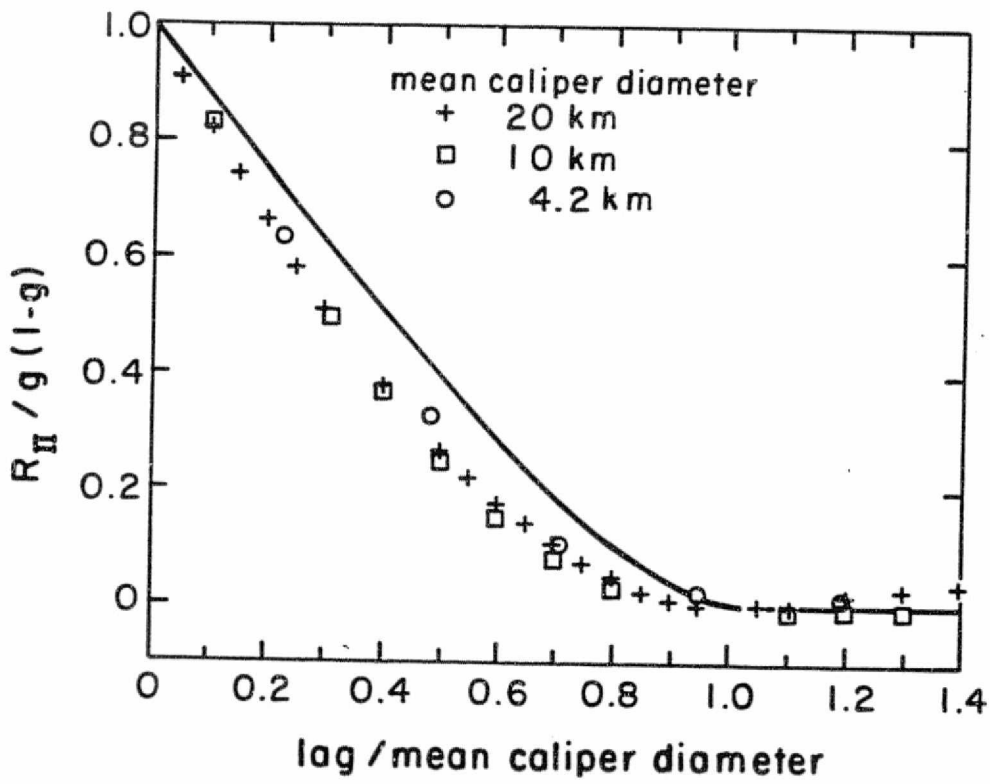

Figure 11. The autocovariance of the indicator function. The solid line is the theoretical expression (7) for rare discs. The symbols show observations from the digitized summer mosaic for several narrow ranges of diameters.

APPENDIX II

ICE THICKNESS DISTRIBUTION--MEASUREMENT AND THEORY

by

D. A. Rothrock

ICE THICKNESS DISTRIBUTION--MEASUREMENT AND THEORY

by D. A. Rothrock

INTRODUCTION

In considering the historical literature relevant to the subject of ice thickness distribution, I was struck by the paper by Wittmann and Schule (1966) at the Lake Arrowhead symposium on the arctic heat budget. They presented a synthesis of visual observations from aircraft showing ice concentration, lead spacings, percent coverage of several ice types, and ridging indices in the subregions of the Arctic Ocean. Their format emphasizes the basic elements of present thinking--first, that we want properties averaged over space scales which include many ice features, and second, that these average properties vary on yet longer scales over the basin and from one season to the next, in ways of interest to the climatologist.

Wittmann and Schule showed what data were available from operational observations just as Soviet scientists were attempting to forecast ice concentration (Nikiforov et al., 1967; Doronin, 1970). In the intervening fifteen years, effort has been directed to defining what data we want for climatological and forecast modeling of sea ice, and why we want them. One data set we want is ice thickness distribution. A major reason is that it tells us the mass of ice in the ice cover. Other reasons are the subject of other chapters. Suffice it to say that ice thickness and its distribution influence components of the surface heat balance, the salt balance of the upper ocean, light penetration and biological productivity, and trafficability on top of, through, and beneath the ice cover. It is unfortunate that thickness alone does not determine these phenomena; they are affected by snow cover, temperature, ice formation history and surface relief.

Presented at the NATO Advanced Study Institute on Air-Sea-Ice Interaction, September 27-October 10, 1981, Maratea, Italy.

so that writing some flux as a function only of thickness sweeps a lot under the rug.

THICKNESS AND ITS DISTRIBUTION DEFINED

~~It is also typical of geophysics that~~ Although one can draw a slab of ice or a cross section of a ridge schematically with several straight lines, when one sets about measuring thickness, it is no longer such a clear-cut notion. There are cavities in ridged ice--some connected to the air or water. Ponds of fresh or brackish water covered with a skim of ice can lie in the troughs of both the upper and lower surfaces. How should a slush of ice crystals be treated? We suppose that one has satisfactory conventions for dealing with these phenomena and that there is a top surface of the ice (not the snow) at a height h_t measured up from the sea surface, and a bottom surface at draft h_b measured down from the sea surface. The thickness is $h = h_t + h_b$.

From thickness measurements which resolve ridges and leads, we want to know average properties over regions hundreds of kilometers in diameter. For instance, to evaluate mean thickness $\hat{H}$ for a region R centered on (x,y), we write

$$\hat{H}(x,y) = \frac{1}{A} \iint_{x' \in R} h(x',y')dx'dy', \quad (\text{where } A = \iint_R dx'dy')$$

as an integral, over thickness, of the area covered by each thickness

$$= \iint_R h \frac{da(h)}{A} \equiv \int_{\text{all } h} h\, g(h)\, dh$$

The ice thickness distribution g(h)dh is defined as the fraction of R with thickness between h and h + dh. If we want, say, an average heat flux $\overline{Q}$ and Q depends on h, we can again integrate over all thicknesses

$$\overline{Q} = \frac{1}{A} \iint_R Q[h(x',y')]dx'dy' \equiv \int_{\text{all } h} Q(h)\, g(h)\, dh$$

Since many fluxes at the air-sea-ice interface are strongly related to thickness, it appears that measurements of thickness distribution would have many applications.

Two observed distributions of draft (which is nearly the same as thickness) are illustrated in Figure 1. The Beaufort Sea distribution shows 5% coverage of 0-to-1 meter ice and 40% coverage of 2-to-3 meter ice. On the other side of the ocean, the Fram Strait ice is much heavier, with roughly five times as much thick ice as in the Beaufort Sea ice. The 2-to-3 meter category is comparatively empty with only 3.5%. Thus the Fram Strait ice has a greater mass, is ~~probably~~ frictionally rougher by virtue of its deformed ice, and yet with its 10% of 0-to-1 meter ice is producing ice faster than the ice in the Beaufort Sea sample.

Although the distributions in Figure 1 look strikingly different, the question must be answered: are these real geophysical differences or could these two distributions be different samples from the "same" ice cover? An empirical answer is obtained by taking several samples from each area, and noting whether all samples from one region are similar to each other and different from the samples from another region.

An analytical technique for answering questions about sampling errors is rooted in probability theory. We adopt the notion that $h(\underset{\sim}{x})$ is a stochastic process; the thickness h at a fixed position $\underset{\sim}{x}$ is a random variable. In this framework, the thickness distribution is a probability function

$$p = \int_a^b g(h)dh = \text{probability that } a<h<b \qquad (1)$$

The expected value of thickness is the mean of the distribution $H = \int_0^\infty gdh$. By taking the process to be nearly stationary (varying only on scales of hundreds of kilometers) and ergodic, we can estimate statistics of the process, such as the mean, or distribution, or spectrum, from spatial averages of data. In addition, we can find confidence intervals for these estimates.

MEASURING THICKNESS AND ESTIMATING ITS STATISTICS

There are two aspects to measurements of thickness statistics: measuring thickness accurately at a point and sampling it at enough points to estimate a statistic satisfactorily. All methods are seriously limited either by measurement errors or sampling errors or both.

Submarine Sonar

The most satisfactory measurements of thickness distribution are obtained from upward-looking submarine sonar. Table 1 lists several cruises from which data have been published. The sonar does not directly measure thickness, but the distance from the transducer mounted on the submarine to the closest point of the bottom surface within the cone of the sonar beam. A pressure sensor measures the transducer depth. The difference between these distances is some approximation of the ice draft.

Table 1. Submarine sonar data.

Submarine	Period	Location	Beam width along track	Submarine depth uncertainty	Length	Reference
Nautilus, Skate, Sargo, Seadragon	1957-62	whole Arctic		2.0 m	$>10^4$km	Lyon (1963,1966) LeShack (1980)
Dreadnought	March 71	86°-90°N 6°-7°E	20°	0.3 m	1000km	Williams et al. (1975)
Sovereign	Oct 76	80°-90°N 25°E-70°W	17°	0.2 m	4000km	Wadhams (1981)
Gurnard	Apr 76	70°-77°N 138°-155°W	3°	0.1 m	1400km	Wadhams and Horne (1978)

There are several sources of measurement error. First, the depth of the transducer is not precisely known; in the more modern data the accuracy is about ±0.2 m or 0.3 m. The error is not so critical for thick ice, but it might make an estimate of the coverage of thin ice useless. It would be useful to know more about the properties of this error. Wadhams (1981) takes it to be white noise with zero mean and variance $(0.2\ \text{m})^2$.

Another error is due to the non-linear smoothing of the surface by the sonar beam--always increasing the observed draft. The problem is akin to surveying the ice with a leveling rod 15 m in diameter. Because no information is sensed from some troughs, there is no way to reconstruct the actual draft, although an approximate reconstruction can be attempted (Williams et al., 1975; Wadhams, 1981). An alternative approach is to simulate numerically the smoothing of the wide beam (17°) sonar on a profile measured with a narrower beam. The wide beam causes the draft distribution to be shifted to the right,

underestimating thin ice and overestimating deep drafts and the mean draft by about 10% (Williams et al., 1975; Rothrock and Thorndike, 1980; Wadhams, 1981).

The desired quantity is thickness, not draft. So, although isostatic balance is achieved only over tens of meters, it is assumed to hold at each point in order to convert $h_b(x)$ to $h(x)$ by

$$h(x) = \frac{\text{water density}}{\text{ice density}} h_b(x) \approx 1.11\, h_b(x)$$

The error thus introduced has zero mean and is probably not important.

To estimate a statistic of thickness, we integrate over some length L of the profile. For instance

$$\hat{H} = \frac{1}{L}\int_0^L h(x)dx$$

is an estimate of the true mean thickness H. If L is chosen too small, the estimate is poor. The estimator $\hat{H}$ is a random variable with a distribution. Its mean is H: it is an unbiased estimate. The important quantity is the variance of $\hat{H}$ which tells how close $\hat{H}$ is likely to be to the true mean. The variance is

$$\text{var}\,\hat{H} = E(\hat{H} - H)^2 = E\left\{\left[\frac{1}{L}\int_0^L h(x_1)dx_1 - H\right]\left[\frac{1}{L}\int_0^L h(x_2)dx_2 - H\right]\right\}$$

$$= \frac{1}{L^2}\int_0^L\int_0^L E\left[h(x_1) - H\right]\left[h(x_2) - H\right]dx_1dx_2$$

E is the expected value operator. The integrand is ~~[illegible]~~ the autocovariance of h, C_h; assuming the thickness is homogeneous and isotropic, it is a function of separation only, $s = |x_1 - x_2|$. The double integral reduces to

$$\text{var } \hat{H} = \frac{2}{L} \int_0^L \left(1 - \frac{s}{L}\right) C_h(s) ds$$

by transforming to new variables s and $t = x_1 + x_2$ and integrating over t. For the *Gumard* profile whose autocovariance is shown in figure 2, this sampling error is listed in Table 2. A typical mean thickness of 3-to-4 m can be sampled by a record ten-to-twenty kilometers long with a sampling error of 10%.

Table 2. The sampling error of an estimate of mean thickness from a line record of length L.

L, km	$(\text{var } \hat{H})^{1/2}$, m
10	0.38
50	0.17
100	0.12
500	0.05
1000	0.04

Although no error model has been developed to treat these several measurement errors and the sampling error as a whole, it is likely that mean thickness estimates from 100 km sonar profiles have an uncertainty of 0.2 to 0.4 m.

How large is the sampling error for distributions shown in Figure 2? In particular, how accurate is an estimate of p, for the bin a<h<b? To answer this question, we need to characterize the spatial arrangement of the regions contributing to this bin. These regions are identified by the indicator function

$$\pi(\underset{\sim}{x},t) = \begin{cases} 1, & a < h(\underset{\sim}{x},t) < b \\ 0, & \text{else} \end{cases}$$

The regions where $\pi = 1$ are the regions we must sample to estimate p. Given profile data (and so, ignoring the y and t dependence), our estimate of p is the fraction of the profile intersecting these regions

$$\hat{p} = \frac{1}{L}\int_0^L \pi(x)dx$$

The estimate is unbiased, since

$$E\hat{p} = \frac{1}{L}\int_0^L E\pi \, dx$$

$$= \text{probability } [a<h(x)<b] \cdot \frac{1}{L}\int_0^L dx = p$$

assuming the process is spatially stationary. The remaining issue is: how large is the variance of p? We have

$$\text{var } \hat{p} = E(\hat{p} - p)^2$$

$$= E\left\{\frac{1}{L}\int_0^L \left[\pi(x_1)-p\right]dx_1 \cdot \frac{1}{L}\int_0^L \left[\pi(x_2)-p\right]dx_2\right\}$$

$$= \frac{1}{L^2}\int_0^L\int_0^L C_\pi(x_1,x_2)dx_1dx_2$$

where

$$C_\pi(x_1,x_2) = E\Big[\pi(x_1) - p\Big]\Big[\pi(x_2) - p\Big]$$

is the autocovariance of the indicator function. Stationarity provides that C_π depends only on the distance between points $s = |x_1 - x_2|$, and the double integral reduces, as before, to

$$\text{var } \hat{p} = \frac{2}{L}\int_0^L \Big(1 - \frac{s}{L}\Big) C_\pi(s)ds \qquad (2)$$

The autocovariance C_π has magnitude $p(1-p)$ at $s = 0$ [since $E\pi(x)\pi(x) = E\pi(x) = p$], and is zero at $s = \infty$ [since $E\pi(x)\pi(x+s) \to p^2$ as $s \to \infty$]. If we define the correlation coefficient

$$r(s) = \frac{C_\pi(s)}{p(1-p)}$$

(2) becomes

$$\text{var } \hat{p} = p(1-p)\ell/L \qquad (3)$$

where

$$\ell = \int_0^L 2\Big(1 - \frac{s}{L}\Big) r(s)ds$$

In practice we are interested in the case where $r(s)$ drops off in a distance much smaller than L; then

$$\ell \simeq \ell_\infty = 2\int_0^\infty r(s)ds$$

(When $L/\ell_\infty > 5$, we find ℓ within 10% of ℓ_∞.) The quantity ℓ_∞ is the autocorrelation length scale; it is also a measure of the characteristic length of individual profile segments with $\pi = 1$.

The first portion of Table 3 gives values of ℓ_∞ computed from the Beaufort Sea profile. Values as small as 10 m have considerable uncertainty because the horizontal resolution of the *Gurnard* data is several meters. The resulting sampling error for $\hat{p}$ is also shown there and in Figure 3. The length scale for thin ice is much greater than that for thick ice, because thin ice is spread out in leads and polynyas, whereas thick ice is clumped in ridges. In the table, we see that the thinnest ice and the 5-to-6 meter ice are equally plentiful, but that the error $\sigma_{\hat{p}}$ is an order of magnitude smaller for the thicker ice bin. To get an equally good estimate of the thin ice would require a record 5600 km long (although not necessarily in a straight line).

Table 3. Length scale and sampling error for ten bins of two draft distributions. The quantity $\sigma_{\hat{p}} = (\text{var } \hat{p})^{1/2}$ is the standard deviation of $\hat{p}$; $\sigma_{\hat{p}}/\hat{p}$ is the relative error.

Bin (m)	Beaufort Sea L ≈ 60 km				Fram Strait L ≈ 100 km		
	ℓ_∞ (m)	$\hat{p}$	$\sigma_{\hat{p}}$	$\sigma_{\hat{p}}/\hat{p}$ (%)	$\hat{p}$	$\sigma_{\hat{p}}$	$\sigma_{\hat{p}}/\hat{p}$ (%)
0 to 1	1300	.053	.033	62	.105	.035	33
1 to 2	230	.089	.018	20	.026	.0076	29
2 to 3	170	.42	.026	6	.036	.0077	21
3 to 4	34	.20	.0095	5	.137	.0063	5
4 to 5	20	.087	.0051	6	.110	.0044	4
5 to 6	14	.051	.0034	7	.084	.0033	4
6 to 7	11	.031	.0023	8	.073	.0027	4
7 to 8	10	.021	.0019	9	.073	.0026	4
8 to 9	12	.014	.0017	12	.073	.0028	4
9 to 10	11	.011	.0014	13	.057	.0024	4

Assuming ℓ_∞ is not very different for another mature ice cover, the values of ℓ_∞ from the Beaufort Sea profile have been used in (3) to evaluate the sampling error for the Fram Strait distribution (in Table 3 and in Figure 3). Within the sampling error, the percentage of thin ice (0-to-1 meter) in he two distributions is marginally distinguishable, but in all other bins, the distributions are measureably different.

Heat balance estimates are sensitive to the thinnest 5 or 10 centimeters of ice. ~~(Maykut, this volume)~~. Given the measurement errors and sampling difficulty, present submarine sonar records cannot provide good estimates of such narrow categories of thin ice.

Boring Holes

The most direct way to measure thickness is to bore a hole or cut a core. Thickness can be measured to whatever accuracy is appropriate to the condition of the surfaces. So there is negligible measurement error.

It can take a few minutes' work to bore a hole. A reasonable strategy for estimating thickness statistics might be to determine the thickness h_i by boring n holes. To be independent the samples must be roughly 1 km apart; this is the spacing at which the autocorrelation function of $h_b(x)$ has its first zero (Figure 2). How close is the estimate of mean thickness

$$\hat{H} = \frac{1}{n} \sum_{i=1}^{n} h_i$$

to the true mean H? The variance of $\hat{H}$ is

$$\text{var } \hat{H} = \sigma^2/n$$

where σ^2 is the variance of the thickness distribution. Table 4 shows a few values of n required to achieve a desired sampling accuracy using the variance $\sigma^2 = C_h(o) = 5.6\ m^2$ from Figure 2. So we could sample H to ±0.5 m by coring once, flying a kilometer away, kicking out a bag of dye to mark an unbiased site, landing and boring at the dye mark and repeating this twenty times. This argument, although without the condition of spatial independence of the thicknesses sampled, has been advanced by Untersteiner and Maykut (1969), with the result that 50 samples are needed to establish the mean with a standard deviation of 1/3 meter.

Table 4. The standard deviation of an estimate of mean thickness from n independent samples.

n	$(\text{var } \hat{H})^{1/2}$, m
23	0.5
62	0.3
560	0.1
2240	0.05

Such requirements to obtain the average ice thickness are difficult to meet in practice, but not outlandish. To obtain an entire thickness distribution by drilling holes in the ice requires logistics bordering on the prohibitive:

From n samples at positions $\underset{\sim}{x}_i$, we estimate the fraction of area in the bin a<h<b by

$$\hat{p} = \frac{1}{n} \sum_{i=1}^{n} \pi(\underset{\sim}{x}_i)$$

which has expected value p and variance

$$\frac{p(1-p)}{n^2} \sum_{i=1}^{n} \sum_{j=1}^{n} r\left(|\underset{\sim}{x}_i - \underset{\sim}{x}_j|\right)$$

The object is to choose the hole positions $\underset{\sim}{x}_i$ for the most efficient sampling. If r is never negative, the minimum variance is obtained by taking all holes so far apart that r_{ij} is zero for $i \neq j$. From the submarine data we know this

separation should be several kilometers (several times ℓ_∞) if we are sampling the 0-to-1 meter bin. The situation reduces then to n independent Bernoulli trials with chance of success p; the variance is simply p(1-p)/n. Table 5 shows that to resolve the distribution into ten bins each with ten percent of the area to an accuracy of 30% (that is, p = 0.10 ± 0.03) would require one hundred holes. ~~This is getting impractical.~~ Boring might be practical only in applications which require a fairly coarse resolution of the distribution with generous tolerances.

Table 5. Number of independent samples n required to estimate fraction of area p with standard deviation σ_p equal to some fraction of p.

p	n for σ_p = 0.3 p	n for σ_p = 0.1 p
0.3	26	233
0.2	44	400
0.1	100	900
0.05	211	1900
0.01	1100	9900

Other Methods

There is a class of observing techniques that may eventually provide measurements of ice thickness from aircraft or satellite. Some are discussed in another chapter, but not necessarily with regard to sensing ice thickness. All are in an early stage of development as thickness sensing instruments. Included are radio echo sounding, visual and infrared photography, various microwave and radar sensors, and laser altimeters. Only radio echo sounding senses both the upper and lower surface. Altimeters sense the height of the

snow surface; to estimate the ice surface h_t and then multiply by

$$\left[1 - \frac{\text{ice density}}{\text{water density}} \right]^{-1} \approx 10$$

to obtain thickness h introduces unsatisfactory errors. The microwave radiometers sense radiative properties at or near the top surface--properties only weakly tied to ice thickness for thick ice.

Some measurements of thin ice fraction have been obtained from LANDSAT visual images with accompanying ground truth. The area of gray ice is measured from an image; the thickness of the gray ice is determined by coring or drilling. This method has provided data for tests of thickness distribution theory (Thorndike, 1980).

THICKNESS DISTRIBUTION THEORY

Having observed the thickness distribution and having at least a rough idea of the thermal and ridging processes which determine it, the ice physicist has naturally been tempted to formulate a mathematical theory to describe the distribution and its evolution. Such a theory was introduced as part of AIDJEX modeling work (Thorndike et al., 1975), and is gradually being introduced into forecasting and climatological models (e.g., Hibler, 1980). Its use does involve several difficulties. First, since the distribution is difficult to observe, often no initial conditions are available, and model results cannot be verified (or refuted). Second, largely for the same reason, model parameters describing the ridging process are not well known, so that the model results can only be considered rough approximations. And third, generally one is modeling the ice cover as a function of two (horizontal)

space coordinates and of time, and the addition of another independent variable, ice thickness, considerably enlarges the computational burden. Being thus forewarned that the theory is no panacea, we will nonetheless review it and see what strengths we find in it.

The equation for the time rate of change of thickness distribution $g(h,\underset{\sim}{x},t)$ is

$$\frac{\partial g}{\partial t} = \psi - \text{div}(\underset{\sim}{u}g) - \frac{\partial}{\partial h}(fg) + \phi \qquad (4a)$$

The four terms on the right hand side, discussed one at a time below, represent opening and ridging, flux divergence, ablation and accretion at the upper or lower surface, and lateral melting. The Lagrangian form is

$$\frac{Dg}{Dt} = \psi - g \text{ div } \underset{\sim}{u} - \frac{\partial}{\partial h}(fg) + \phi \qquad (4b)$$

These equations are primarily statements relating geometry and kinematics. The real physics of the ice cover enters in the structure of ψ, f, and ϕ. All three of these functions depend on the thickness distribution itself, making (4) a non-linear functional equation. Early work with this equation treated only the feedback of the thickness distribution g through ridging and opening ψ. More recent work (Maykut, in preparation; Hibler, 1980) has included the feedback by which summer melting (ϕ and f) is determined by the amount of radiation absorbed and hence the open water.

To consider flux divergence, we focus on an arbitrary region R and the exchange of h-ice (ice of thickness between h and h+dh) across its boundary curve C. The flux of h-ice across a line with normal $\underset{\sim}{n}$ is $\underset{\sim}{n} \cdot \underset{\sim}{u}g\,dh$. The

total flux into or out of R is written first as the integral of the flux around C

$$\oint_C \underset{\sim}{n} \cdot \underset{\sim}{u}g \, dh \, dl$$

and then, by Gauss' theorem, as

$$\iint_R \mathrm{div}(\underset{\sim}{u}g \, dh)da$$

This term accounts for the net loss of h-ice from R

$$-\frac{\partial}{\partial t} \iint_R (gdh)da$$

Since R is arbitrary, and fixed in space, the equation takes the differential form

$$\frac{\partial g}{\partial t} = -\mathrm{div}(\underset{\sim}{u}g)$$

This flux divergence term has two parts: $-g \, \mathrm{div} \, \underset{\sim}{u}$, denoting the influx of h-ice by convergence, and $-\underset{\sim}{u} \cdot \mathrm{grad} \, g$ denoting advection.

Thermal growth $f = dh/dt$ carries ice to a new thickness, in just the same way as velocity $\underset{\sim}{u} = d\underset{\sim}{x}/dt$ carries ice to a new position, giving a term completely analogous to the flux divergence term

$$\frac{\partial g}{\partial t} = -\frac{\partial}{\partial h}(fg) \qquad (5)$$

This is a mathematical statement. For a more physical view of thermal growth, it is best to turn to the cumulative distribution G(h,t). The governing principal is that ice thinner than h at time t is thinner than h + fdt at time t + dt giving

$$G(h,t) = G(h + fdt,\ t + dt)$$

Expanding the right hand side about (h,t) gives

$$G(h,t) = G(h,t) + \frac{\partial G}{\partial h} \cdot fdt + \frac{\partial G}{\partial t}\, dt + O(dt^2)$$

or

$$\frac{\partial G}{\partial t} = -f\, \frac{\partial G}{\partial h}$$

which is the integral form of (5).

Lateral melting ϕ eats away at the edges of floes to reduce their area. The process conserves area: an amount of open water is formed equal to the total ice-covered area melted so

$$\phi = s\Big[\delta(h) - \ell(h)\Big]$$

where s depends on the available heat (but not on h), δ is the Dirac delta function and $\ell(h)$ is positive with $\int_0^\infty \ell(h)dh = 1$. The volume loss of h-ice $sh\ell(h)$ is proportional to the area of floe edges which we can take to be proportional to hg(h); hence, $\ell(h) \propto g(h)$, and the integral

constraint determines that $\ell(h) = g(h)$. The unknown s is determined by stating that

$$Q = \rho L \int_0^\infty h\phi dh$$

where Q is the rate at which heat becomes available for lateral melting (per unit area of R), ρ is the density of ice, and L is the latent heat of fusion. Solving for s and substituting gives

$$\dot{s} = \frac{Q}{\rho L H}\left[\delta(h) - g(h)\right]$$

where $H = \int_0^\infty hgdh$.

Ridging and opening processes are embodied in the redistribution function ψ, on which there are two constraints. The ~~mechanical~~ processes can only rearrange existing ice, ridging thin ice to produce thick, but cannot alter the mean ice thickness, so by assumption

$$\int_0^\infty h\psi dh = 0$$

Furthermore, the formation of new area of open water less the loss of area by ridging must exactly accommodate the area of ice imported by convergence. Hence, ignoring the thermodynamics (setting $f = \phi = 0$) and integrating (4) over all h gives

$$\int_0^\infty \psi dh = \text{div } \underset{\sim}{u}$$

The definition of ψ is hypothetical, relying on assumptions and reasoning about idealized situations (Thorndike et al., 1975; Hibler, 1980); there are few hard facts about redistribution.

Open water formation is represented by a delta function at $h = 0$, and ridging by a function $\mu(h)$ which is a sink of thin ice and a source of thick ice. The degree to which each of these processes occurs in redistribution depends on strain rate invariants. We denote the sum of the principal strain rates by $\dot{\varepsilon}_I$ ($\equiv$ div $\underset{\sim}{u}$) and the difference by $\dot{\varepsilon}_{II}$. These can be expressed in polar form as a modulus $|\dot{\varepsilon}| = (\dot{\varepsilon}_I^2 + \dot{\varepsilon}_{II}^2)^{\frac{1}{2}}$, which tells the quantity of the deformation, and an angle $\theta = \tan^{-1}(\dot{\varepsilon}_{II}/\dot{\varepsilon}_I)$, which tells the quality of the deformation.

The combination of ridging and opening into ψ is assumed to be proportional to strain rate in the form

$$\psi = |\dot{\varepsilon}| \left\{ \alpha_o(\theta)\ \delta(h) + \alpha_r(\theta)\ \mu(h) \right\}$$

The coefficients α_o and α_r need to be observed in nature--the idea is that divergence (small θ) will favor opening (larger α_o, smaller α_r) and conversely that convergence (θ getting up toward π) will favor ridging. But even in pure shear ($\theta \sim \frac{\pi}{2}$) the separation of floes in some locations and coming together of floes elsewhere will insure that both opening and ridging occur simultaneously.

Just how the ridging function μ varies with h depends on the present state of the thickness distribution (since we don't want to ridge ice that isn't there), and on two parameters G* and k. G* is the cumulative fraction of the thickest ice assumed to ridge. It is taken to lie in the range 0.05 to 0.15, allowing ice up to

about one meter to ridge. The second parameter k is the ratio of the thickness of ridged ice to its original thickness. Of course, even the notion that this ratio is a constant is a strong contradiction of reality. The value originally assumed (k = 5) seems to have been too small, producing no ice thicker than 6 m and allowing the pack to deform too easily. (Ice strength is thought to be tied to ridging and to increase with the size of ridges being formed.) A value of k = 15 is better in both respects.

An alternative formulation of redistribution has been advanced in which ridged ice is quantified not by its thickness distribution but in terms of mean ridge height and ridge intensity (Bugden, 1979). The motivation, of course, is that ridge statistics are readily available from aircraft visual observations and laser profiles, so a model predicting them would be testable. This approach has its drawbacks, though, and has not been hotly pursued. Ridged ice is not the sheet threaded with long triangular rubble piles seen in schematic diagrams. In reality old and new ridges overlap, making the identification of a pressure ridge a matter of each observer's particular definition. So ridge statistics are not uniquely related to areas or volumes of ridged ice. Hence an equation involving areas of undeformed ice and ridged statistics for deformed ice is less clean than the formulation involving only ice areas. The more desirable path is to state the theory wholly in terms of thickness distribution and improve techniques for extracting it from data.

The first theoretical solutions for thickness distribution were calculated for a single Lagrangian point from (4b); that is, space was not a variable. We will examine solutions of that problem here. Deformation rate

is a function of time, known from sets of buoy tracks, often lacking frequencies greater than 1 cycle per day. Growth rate is a function of thickness and time, known from climatology, and lateral melting is neglected. Starting with an observed distribution as an initial condition, solutions change in time but hover near a realistic distribution. Thus the theory is compatible with our understanding of ice dynamics.

The theory, of course, can do more than predict the distribution. It shows us which terms are important to the balance in various ranges of thickness and just how large these terms are. Table 6 shows the annual average of net thermal production (growth into the range less growth out), ridging and open water gain, and import by convergence. The thinnest category is maintained by newly formed open water growing thermally into the next category; some ice is ridged out of this category. For the rest of the thin ice (0.1 to 1.6 m), the net thermal production is nearly balanced by ridging loss. For equilibrium ice (1.6 to 6.4 m) both thermodynamics and ridging provide sources. A balance is only made possible by the divergence. Thick ice (>6.4 m) is not in balance. It is gaining 0.7% per year because the ridging gain cannot be compensated for by this divergence and the net melt.

Whereas ice thinner than the mean adjusts fairly rapidly to a given deformation and growth regime, it is probably futile to think about an equilibrium distribution for thick ice. For one thing, the determining variables are poorly known: the long term net divergence, the infrequent large convergences capable of making very thick ice, and the melt rate and rate of erosion for thick ice. For another, the adjustment time for thick ice is slow: it takes thirty years for twenty-five meter ice to approach equilibrium thickness. Only the Beaufort Sea may contain ice that old.

Table 6. An average over one year of the terms in the thickness distribution equation (4b). Each term is also integrated over a thickness range. Units of terms are percent per day, of thickness distribution, percent.

Terms in (4b)		0-0.1 m	0.1-1.6 m	1.6-6.4 m	6.4-25.6 m
Thermal flux gradient	$-\frac{\partial}{\partial h}(fg)$	-0.59	0.43	0.013	-0.003
Open water production	$A\,\delta$	0.73			
Ridging loss	$-C\,\mu_L$	-0.14	-0.44	0	0
Ridging gain	$C\,\mu_G$	0.00	0.01	0.015	0.014
Import	$-g\ \mathrm{div}\ u$	0.00	0.00	-0.028	-0.009
Rate of change of g		0.00	0.00	0.000	0.002
Thickness distribution	$\int_a^b gdh$	2.9	20.0	58.9	18.1

The balance in Table 6 is no surprise but simply shows that the model behaves much as the ice it was designed to mimic: open water grows to thin ice and is ridged into thick ice which continually ablates or is exported. The theory elucidates some unforeseen details, and most importantly tells the rates of these various transfers and shows how nearly balanced they are.

A WORD ON NUMERICAL TECHNIQUES

One numerical procedure for solving this problem involves integrating the functional differential equation

$$\frac{\hat{D}G}{\hat{D}t} = \int_0 \psi dh - G \text{ div } \underset{\sim}{u}, \quad \text{where } \frac{\hat{D}}{\hat{D}t} = \frac{D}{Dt} + f \frac{\partial}{\partial h}$$

for each time step along characteristics satisfying

$$\frac{\partial h}{\partial t} = f(h,t)$$

and then to interpolate the new G(h + fdt, t + dt) to some fixed h-grid G(h, t + dt). A large area of open water freezing at the same time (late summer appears as a step in G(h) or a spike in g(h). This step cannot be resolved by any fixed grid. But to make matters worse, repeated interpolation at each time step continues to smooth out the step. The numerical solution then is only a shadow of the correct solution. An alternative procedure (Colony, personal communication) is to allow the h-grid to float, moving with the characteristics. A step can be followed by two nearly identical characteristics on which the values of G are quite distinct. Figure 4 shows solutions using Colony's characteristic grid, a coarse fixed grid (à la Thorndike et al., 1975), and a much denser fixed grid (153 h-values at spacings varying from 2 to 50 cm). Table 7 shows further comparisons. The integration starts with all thin ice, proceeding in time steps of one day for a year; the deformation rates are those computed from the AIDJEX manned camps (Colony, 1978). The values k = 15 and G* = 0.1 were used, and A and C were those identified with the 30° teardrop in Rothrock and Hall (1975).

Table 7. Variables computed by different numerical procedures.

Numerical procedure	mean thickness $\bar{h}$, m	thermal production $\bar{f}dt$, m	coverage by ice < 1 m G(1), %	coverage by ice between 1 and 2 m G(2)-G(1),%	coverage by ice $\geq$ 6 m 1-G(6), %
Characteristic grid	144	163	23	69	95
Dense fixed grid	144	171	34	58	95
Coarse fixed grid	176	246	45	23	96

The large step at 1.2 m is the remains of the initial thin ice. The smaller step at 18 cm is from the freeze up several days before the integration stops. These are clearly not going to be captured by a coarse fixed grid. It is more surprising that the finer fixed grid smears the large step out over nearly one meter. Another curiosity is that even the coarse fixed grid represents the thick ice better than the thin ice from which it is produced. I see two lessons here. First, special numerical care is warranted for these discontinuous functions. Second, some variables are robust against numerical errors, and some are quite sensitive; it would seem prudent to know into which class one's favorite variable falls.

G can also have steps in space. If there is ice of thickness H to the left of an ice edge at x = X, G has a jump along the curve shown in Figure 5. Representing this function G(h,x) accurately will require more than single values on a fixed (h,x)-grid. And as H and X change with time, the jump in G will be lost if special care is not taken.

TESTING THE THEORY

Several tests of the theory (Nye, 1975; Thorndike et al., 1975; Rothrock and Hall, 1975; Coon et al., 1977; Thorndike, 1980) have focused primarily on the dynamics of thin ice and open water and have compared these quantities to satellite observations. They show that:

i) the theory adequately simulates thin ice with the chosen forms of A, C, and μ_L, and the value $G^* \sim 0.05$ to 0.10,

ii) the considerable uncertainty in deformations estimated from the motion of only several points can cause considerable discrepancy between computations and observations, in particular of summer open water,

iii) the value k = 5 produces ridged ice that is insufficiently thick.

As another test of the theory, focussing particularly on the thick ice, the following situation has been simulated. Ice forms in the Siberian marginal ice zone, and drifts across the ocean. It passes the pole in roughly three-to-five years, judging from the drift tracks of North Pole 6 and 10 and the *Sedov*. Starting on September first with an initial condition of 100% open water, the thickness distribution model just discussed (k = 15, G^* = 0.1, 30° teardrop, AIDJEX manned camp deformations, climatological growth rates, no lateral melting) was integrated for several years.

Some results are compared in Table 8 with submarine data from the vicinity of the pole. The theory has not produced enough thick ice. That was a shortcoming in the calculation by Thorndike et al. (1975), but there k was 5, and no ice over 6 m was produced. Here, k is 15, and ice is produced in the whole thick end of the distribution, up to 23 m. Furthermore, the shape of the thick end of the distribution is similar to observations. Ice of the right thickness is being made but in too small an amount. The more likely cause for the discrepancy is in the deformations driving the ridging. They were observed in a

ature ice cover in the Beaufort Sea, and may be quite inappropriate for young ice in the marginal ice zone.

Table 8. Comparison of theory to data in a transpolar drift.

	Mean thickness	Coverage of ice thinner than 2.2 m	Coverage of ice between 2.2 and 5.6 m	Coverage of ice thicker than 5.6 m
	h, m	%	%	%
Theory, after 3 years, October	3.0	74	12	14
Theory, after 5 years, October	3.5	64	16	20
Sovereign, sec. 17-21 October	4.4	13	59	33
Dreadnought, March	4.6	12	55	33

Sovereign and *Dreadnought* data are from Wadhams (1981). Drafts are multiplied by 1.11 to obtain thickness.

The open water at the start of the simulation has, after five years, grown to 1.9 m and covers 30% of the area. The *Dreadnought* thickness distribution shows a strong peak at 2.9 meters' thickness (Williams et al., 1975, Figure 10). The *Sovereign* peaks occur at slightly greater thicknesses. This deficiency of the model could be due to poor growth rates or to an underestimation of rafting and ridging of the young Siberian ice.

The procedure of combining inputs and thickness distribution observations from different times and places is not going to provide any further improvement

in the theory. As the ditty has it, "the'v gone about as fer as the' kin go." A more controlled and complete experiment is necessary, in which a Lagrangian region is monitored repeatedly by submarine and satellite, and the deformation history and thermal environment is documented continuously.

WHITHER THICKNESS DISTRIBUTION?

Several avenues are available for advancing our knowledge of ice thickness distribution.

1) The parameters in the model are pinned down as well as available data allow. A controlled mass balance experiment would be valuable in which the model inputs and outputs were simultaneously monitored.
2) Sampling theory can determine how large a sample is required to resolve the differences we think we observe between two distributions. This should be a prerequisite for a mass balance experiment.
3) Remote sensing is unlikely to resolve the thickness of thick ice, but a program combining satellite estimates of thin ice and submarine sampling of thick ice would be valuable.
4) Substantial concentration of a single thickness creates numerical problems that need more attention.
5) The ice cover moves in pieces and not as a continuum as presently assumed in theory and in the analysis of deformation. A more direct approach to redistribution could be developed in terms of the movement of pieces.

REFERENCES

Bugden, G. L., 1979. The deformation of pack ice by ridging. J. Geophys. Res., 84, 1793-96.

Colony, R., 1978. Daily rate of strain of the AIDJEX manned triangle. AIDJEX Bulletin, 39, 85-110.

Coon, M. D., R. T. Hall and R. S. Pritchard, 1977. Predictions of arctic ice conditions for operations. Proc. 9th Annual Offshore Technology Conf., 4, 307-14. Offshore Technology Conference, Callas, Texas.

Doronin, Yu P., 1970. K methodike rascheta splochennosti i dreifa l'dov. (On a method of calculating the compactness and drift of ice floes.) Tr. Arkt. Anarkt. Nauch. Issled. Inst., 291, 5-17. (English translation AIDJEX Bulletin, 3, 22-39.)

Hibler, W. D., 1980. Modeling a variable thickness sea ice cover. Monthly Wea. Rev., 108 (12), 1943-73.

LeShack, L. A., 1980. Arctic ocean sea ice statistics derived from the upward-looking sonar data recorded during five nuclear submarine cruises. Technical Report to the Office of Naval Research. Contract N00014-76-C-0757/ NR 307-374.

Lyon, W., 1963. The submarine and the Arctic Ocean. Polar Record, 11, 699-705.

Lyon, W., 1966. Under surface profiles of sea ice observed by submarine. 11th Pacific Science Congress, Tokyo.

Maykut, G. A., in press. Large scale heat exchange and ice production in the central arctic. J. Geophys. Res.

Nikiforov, Ye. G., Z. M. Gudkovich, Yu. I. Yefimov, M. A. Romanov, 1967. Osnovy metodiki rascheta pereraspredeleniya l'da b arkticheskikh moryakh b navigatsionnyy period pod vosdeystviem vetra. (Principles of a method for computing ice redistribution in arctic seas under the influence of wind during the navigation system.) Tr. Arkt Anarkt. Nauch. Issled. Inst., 257, 5-25. (English translation AIDJEX Bulletin, 3, 40-64. NTIS No. PB 196063.)

Nye, J., 1975. A test of ice thickness redistribution equations by measurements on ERTS pictures. AIDJEX Bulletin, 28, 141-49.

Rothrock, D. A. and R. T. Hall, 1975. Testing the redistribution of sea ice thickness from ERTS photographs. AIDJEX Bulletin, 29, 1-19.

Rothrock, D. A. and A. S. Thorndike, 1980. Geometric properties of the underside of sea ice. J. Geophys. Res., 85 (C7), 3955-63.

Thorndike, A. S., 1980. Tests of the ice thickness distribution theory. In Sea Ice Processes and Models, ed. R. S. Pritchard, Univ. of Washington Press, Seattle, Washington, 144-50.

Thorndike, A. S., D. A. Rothrock, G. A. Maykut and R. Colony, 1975. The thickness distribution of sea ice. J. Geophys. Res., 80 (33), 4501-13.

Untersteiner, N. and G. A. Maykut, 1969. Arctic sea ice, Naval Res. Reviews, Ofc. of Naval Res., Wash., D.C., 12-13.

Wadhams, P., 1980. A comparison of sonar and laser profiles along corresponding tracks in the Arctic Ocean. In Sea Ice Processes and Models, ed. R. S. Pritchard, Univ. of Washington Press, Seattle, Washington, 283-99.

Wadhams, P., 1981. Sea ice topography of the Arctic Ocean in the region 70°W to 25°E. Phil. Trans. Roy. Soc., 302, 45-85.

Wadhams, P. and R. J. Horne, 1980. An analysis of sea ice profiles obtained by submarine in the Beaufort Sea. J. Glaciol., 25 (93), 401-24.

Williams, E., C. Swithinbank and G. de Q. Robin, 1975. A submarine sonar study of arctic pack ice. J. Glaciol., 15 (73), 349-62.

Wittmann, W. I. and J. J. Schule, 1966. Comments on the mass budget of arctic pack ice. Proc. Symp. on the Arctic Heat Budget and Atmospheric Circulation, RM-5233-NSF, ed. J. O. Fletcher, Rand Corp., Santa Monica, Calif., 215-246.

FIGURE CAPTIONS

Figure 1. Distributions of ice draft for two regions. The bin size is one meter. The Beaufort Sea data are from *Gurnard* profiles (the 60 km offshore profile of Rothrock and Thorndike, 1980), and the Fram Strait data are from *Sovereign* profiles (a 97 km profile, section no. 2 in Wadhams, 1980).

Figure 2. Autocovariance of the Beaufort offshore profile (from Rothrock and Thorndike, 1980).

Figure 3. The range of probable values for the distributions in Figure 2. In each bin, the range $\hat{p} - \sigma_p$ to $\hat{p} + \sigma_p$ has been filled in--stippled for the Beaufort Sea distribution and crosshatched for Fram Strait.

Figure 4. Cumulative thickness distribution computed from theory using three numerical schemes: characteristic grid, coarse fixed grid, and fine fixed grid.

Figure 5. A line of discontinuity in G on the (x,h) plane. Open water lies to the right of $x = X$.

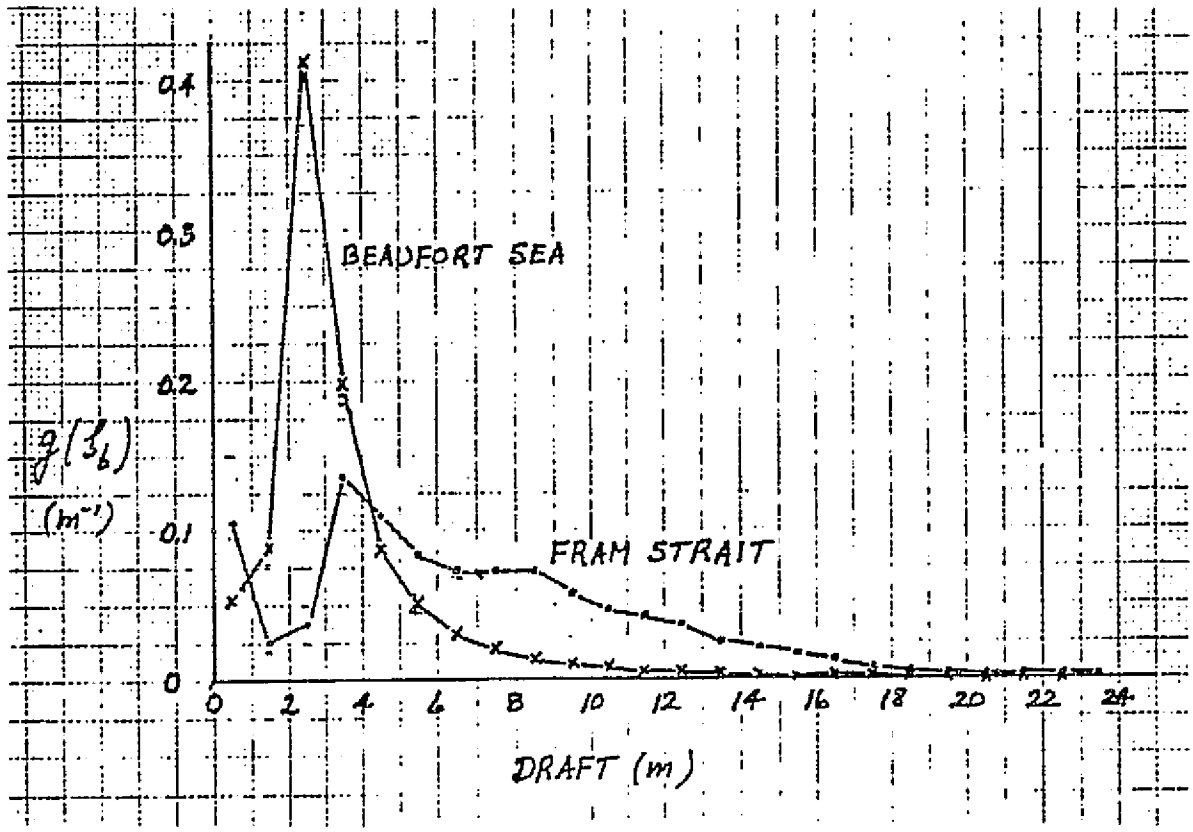

Figure 1. Distributions of ice draft for two regions. The bin size is one meter. The Beaufort Sea data are from *Gurnard* profiles (the 60 km offshore profile of Rothrock and Thorndike, 1980), and the Fram Strait data are from *Sovereign* profiles (a 97 km profile, section no. 2 in Wadhams, 1980).

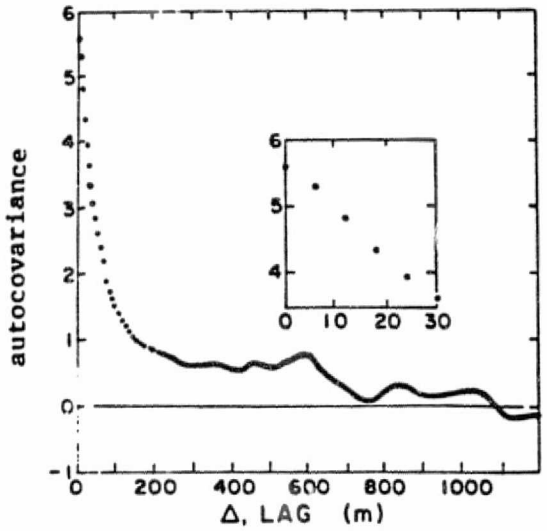

Figure 2. Autocovariance of the Beaufort offshore profile (from Rothrock and Thorndike, 1980).

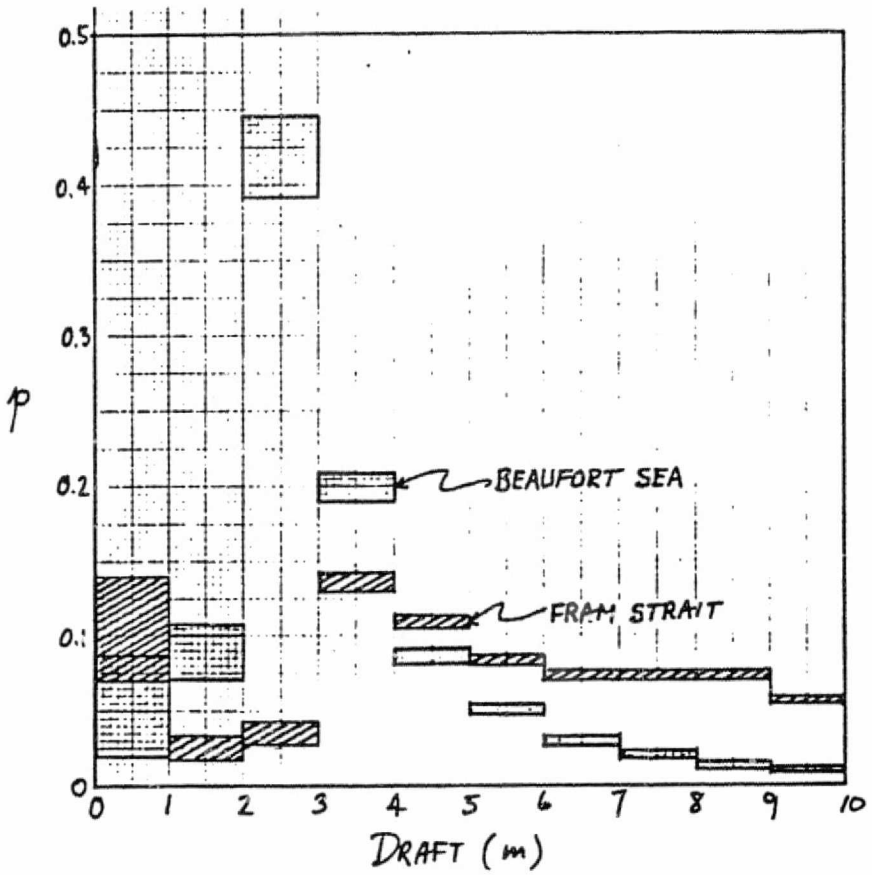

Figure 3. The range of probable values for the distributions in Figure 2. In each bin, the range $\hat{p} - \sigma_p$ to $\hat{p} + \sigma_p$ has been filled in--stippled for the Beaufort Sea distribution and cross hatched for Fram Strait.

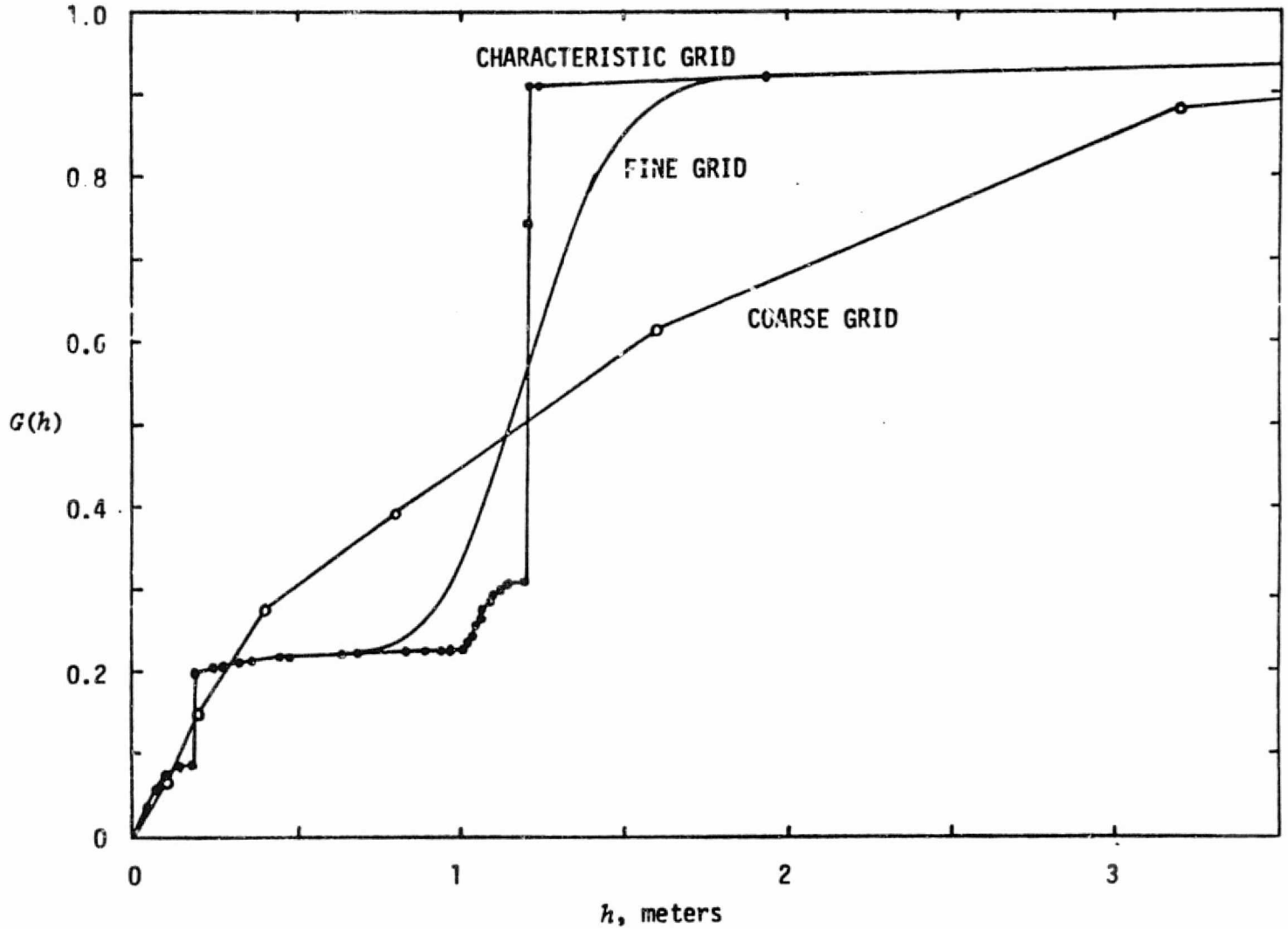

Figure 4. Cumulative thickness distribution computed from theory using three numerical schemes: characteristic grid, coarse fixed grid, and fine fixed grid.

Figure 5. A line of discontinuity in G on the (x,h) plane. Open water lies to the right of $x = X$.

APPENDIX III

KINEMATICS OF SEA ICE

by

A. S. Thorndike

CHAPTER 7. KINEMATICS OF SEA ICE

A. S. Thorndike

Contents

List of Figures

List of Tables

Kinematics is that branch of physical science dealing with motion itself and not with the causes of the motion. Attention is focused, in this chapter, on how sea ice moves. The deeper question of why sea ice moves as it does is addressed in the chapter on sea ice dynamics. For some scientific and practical applications, knowledge of the ice kinematics (as opposed to the dynamics) is sufficient. As examples, consider gouging of the sea floor in shallow water, the transport of natural debris or pollutants, the impact loads on structures, navigability in icy regions, and the movement of the ice edge. Aside from these applications, the study of kinematics is a basic step toward understanding the dynamics.

Figure 1 illustrates the idea that the motion of sea ice is the response of the ice pack to external forces. To understand the response of the ice one needs to monitor both the driving forces and the motion. Since we will discuss only the motion here, there will be the underlying ambiguity of whether the results inform about properties of the ice itself or about the driving forces. We will see for example that the ice motion is nearly non-divergent. But we should not conclude on this basis alone that the ice is an incompressible material. The correct explanation could be that the net driving force is itself nearly non-divergent. Because of this ambiguity in the interpretation of kinematic data, it is useful to think of the study of the kinematics as part and parcel of the broader study of sea ice dynamics.

The fundamental kinematic notion is that all pieces of ice have an identity which is preserved in time. If we identify a piece of ice by making a small mark on the ice surface at position X at time o, the assumption is that at some later time t, the piece of ice as identified by that mark will be at a position x. This defines the position function $x(t,X)$ with $x(o,X) = X$. We do not mean to imply by this that ice floes retain their identity indefinitely, only that it is possible to track individual points. Two points originating on the same ice floe may very well wander apart in time, but we assume we could keep track of them.

There are difficulties with the notion of a position function. It is natural to consider the space domain to be the two dimensional surface of the Arctic Ocean, say $\mathcal{X}$. At $t=o$ there will generally be some points in $\mathcal{X}$ which are not covered by ice, so $x(t,X)$ is not defined for some $X \in \mathcal{X}$.

Further, ice is always being created and destroyed thermodynamically, so the position function $x(t,X)$ is only defined for an interval of time.

Finally, the idea that the small mark retains its identity is questionable. This is a common problem in the definition of the motion of a turbulent fluid. After a time the marked fluid has mixed with the unmarked and it is no longer possible to assign a position to the mark. Something of the same sort happens with sea ice. Despite these shortcomings, the notion of a position function is the best we have. Furthermore this notion corresponds exactly with most of the observations we have. We will use the term trajectory for the function $x(t,X)$ where X is held constant. The initial position X serves to label ice particles and we refer to the trajectory $x(t,X)$ of the particle X.

5.1 Observations

The most common observations of ice motion are of trajectories of ice particles consisting of a sequence of measurements (z_i, t_i), $i = 1, \cdots N$ where

$$z_i = x(t_i, X) + \varepsilon_i$$

The measurement error is represented by ε_i.

In passing we mention that other kinds of measurements of ice motion have been made. Hunkins (1967) and McPhee (1978) for instance inferred the ice velocity using current meters suspended from the ice into what they assumed to be essentially a static ocean. These data were used to study motion on the time scales of hours. An attempt to study motions on much shorter time scales using accelerometers was made by Craig (1972).

Many techniques have been used to measure ice trajectories. These are summarized in Table I. Each technique has its good and bad features. Over the past decade most data have been obtained by satellite positioning which works somewhat as follows. Suppose a stable frequency f_0 is transmitted by a device on the ice. The signal received at the rapidly moving satellite will have a frequency f which has been shifted by the Doppler effect: $f = f_0 + \Delta f$. The Doppler shift Δf is related to the rate of change of distance between the device on the ice and the satellite: $\Delta f \sim \frac{d}{dt} \| x_{sat} - x_{ice} \|$. The received frequency f is measured at several times. If the satellite coordinates are known at these times, then each measurement produces an equation with unknowns f_0 and x_{ice}. Generally several measurements are made during the 10 to 20 minutes it takes for the

TABLE I

Techniques for measuring sea ice motion

technique	basic measurement	sampling rate	accuracy	comments
Hunkins et al, 1971 celestial navigation	azimuth and elevation of heavenly bodies	1 per day	10^3 m	weather dependent
Martin et al, 1978 satellite navigation	Doppler shift of stable transmitted signal	30 per day	30-500 m	
Thorndike, 1973 acoustic tracking	travel time from ice to fixed reference on the ocean floor	up to 1 per minute	5 m	limited range, elaborate instrumentation, relative position only
Tucker et al., 1980 Tabata et al., 1980 radar	travel time from source on shore to target on ice	no limit	< 1 m	limited to near shore
Hall, 1980 Landsat imagery	location of identifiable ice features	erratic	80 m	weather dependent, good space resolution, poor time resolution
Hall & Rothrock, 1981 synthetic aperture radar imagery (SEASAT)	location of identifiable ice features	1 per 3 days	80 m	no system available at present, properties of future systems unclear

satellite to pass by. The several equations are solved simultaneously for f_o and χ_{ice}. Precise positioning requires a stable transmit frequency, precise measurement of the received frequency, and precise knowledge of the satellite coordinates. With care, errors can be controlled to the order of tens of meters, as in the best uses of the Navy Navigation Satellite System.

Satellite systems which serve primarily to relay data from automatic data platforms (or buoys) to data processing centers also determine the location of the transmitting data platform, using the same Doppler positioning principle. The ARGOS system currently on the NOAA-B satellite can relay data from up to 30 sensors and determine platform locations to an accuracy of a few hundred meters about ten times per day. Fully automatic platforms cost in the neighborhood of $6,000 with additional costs depending on the desired sensors.

Satellite imaging systems can also be used to measure ice motions, provided that some features on the ice can be identified in a sequence of images. Because of their all season and all weather capability and good resolution, imaging radar systems will probably be best. The basic angular resolution of these systems is approximately the ratio of the wavelength of the radar signal to the diameter of the antenna. To achieve an angular resolution of 10^{-5} (10 meters at a range of 1,000 kilometers) with a wavelength of 25 cm (1.2 GHz) requires an antenna 25 km in diameter. Although such large antennas cannot be constructed in space, it is possible to synthesize large antennas by using data from several points along the satellite's orbit. The determinations of the geographical position of an ice feature with the SEASAT data contained errors of up to 3 kilometers (see Hall and Rothrock, 1981). Unless these errors can be reduced the data are not particularly valuable for measuring the displacements over intervals of a few days or less. However, the errors are highly correlated in space and are essentially eliminated in estimates of the spatial variability of the ice motion.

The attractive feature of imaging radar systems is their potential to sample densely in space. Hall and Rothrock's work suggests that it will be possible to track roughly one feature per square kilometer, which will resolve most of the spatial structure of the field of motion. Techniques for extracting data from the images or from the raw data are still rather primitive. No doubt satisfactory automated techniques for identifying and tracking features will be developed when the need arises. At present there is no imaging radar system in space. Planning is underway for a system to be in operation perhaps by 1985.

5.1.1. Sources of data

The earliest ice motion data are the trajectories of ships beset in the ice. These are followed by the trajectories of numerous Soviet and U.S. drifting research stations, and more recently by the trajectories of automatic data buoys. The following list of data sources is by no means complete.

Experiment	Reference	Description
T-3	Hunkins et al., 1971	Monthly positions May 1962-December 1970
Beset ships and drifting stations before 1970	Hastings, 1971	A chart showing most prior trajectories, one point per month; includes: Fram, Jeanette, Maud, Sadko, Sedov, Tegetthoff, British Trans-arctic Exp., Alpha, Arlis I, Arlis II, Charlie, North Pole 1-20, T-3.
AIDJEX 1972	AIDJEX Staff, 1972	100 km triangle, Beaufort Sea, March and April 1972.
AIDJEX 1975-76	Thorndike and Cheung, 1977	Manned camp positions and velocities tabulated at 6 hr intervals, daily buoy positions.
1976-77 buoys	Thorndike and Cheung, 1977	Tabulated daily positions of Beaufort Sea buoys.
1979 buoys	Thorndike and Colony, 1980	Tabulated daily positions, 25 buoys, analyses of surface pressure plotted daily.
1980 buoys	Thorndike and Colony, 1981	As above.
Fram I, 1979	Hunkins et al., 1979	March-May 1979; 84°N, 9°W
LOREX 79	Popelar et al., 1981	Three stations, 100 km spacing April, May 1979; 88°-90°N.

5.2 The general circulation

The main features of the long term circulation, Figure 2, are the clockwise circulation in the Beaufort Sea--and the motion of ice from the Siberian coasts across the North Pole and through the Greenland-Spitsbergen passage. Time honored nomenclature for these features are the Beaufort Gyre and the Transpolar Drift Stream. Some handy numbers for these long term features are:

center of Beaufort Gyre: 80°N, 155°W, half way between Pt. Barrow, Alaska and the North Pole

time to make 1 circuit: 5 years

time to traverse Transpolar Drift Stream: 3 years

area flux through Greenland-Spitsbergen Passage:
300 km^2/day or about 20% of the area of the basin per year.

This pattern of motion exists only as an average over several years. On shorter time scales there are departures from the long term pattern. Consider for example the trajectories plotted in figure 3 for the year 1979 and figure 4 for 1980. The trajectories are characteristically meandering and convoluted showing that on monthly time scales the ice motion differs markedly from the long term mean. On shorter time scales, not resolved in these figures, the motion is even more irregular. Notice the major anomaly which occurred in the summer of 1980 when the motion of several buoys for several months was in the opposite sense from the long term mean. These departures of the actual motion from the long term pattern in most cases represent the response of the ice to the passage of atmospheric systems.

If we ignore the forces and examine only the ice motion, the departures from the mean circulation appear aperiodic and chaotic. The departures can be thought of as random but they are not without structure. Our objective now is to clarify this structure.

5.3 Ice velocity

The ice velocity field can be defined by the relationship

$$u(x,t) = \lim_{h \to 0} \frac{x(t+h,X) - x(t,X)}{h} .$$

Here the particle label X plays no role.

This definition is meaningful only if the limit exists. From a practical point of view it is useful only if the limit exists and is approached when the interval h decreases to the time interval τ between observations.

In figure 5 several sets of observations of ice motion are plotted, showing the variation of one coordinate of position versus time. Successive data sets divide the sampling interval τ by 15 and improve space resolution by the same factor, giving a sequence of closer and closer perspectives on the motion. By constructing velocity estimates, $u_k(t) = [x(t+k\tau,X) - x(t,X)]/k\tau$ for k decreasing to 1, one can examine the limiting process. In the first two figures of the sequence, u_k continues to change appreciably for small k. In the last two figures, $u_k(t)$ at most times t becomes almost independent of k for small k, implying that on these time scales, $\tau \lesssim 15$ minutes, the ice indeed possesses a velocity.

Convergence of $[x(t+\tau,X) - x(t,X)]/\tau$ to a definite limit implies that the increment $x(t+\tau,X) - x(t,X)$ is proportional to τ for small τ. For random processes, a useful condition for convergence is mean squared convergence in which the variance of the increment becomes proportional to τ^2 for small τ. This can be readily tested for ice trajectories by plotting $E(x(t+\tau,X) - x(t,X))^2$ versus τ on a log-log plot, as is done in figure 6. The process is differentiable if the graph has slope of 2 for small τ.

From a practical point of view the process ceases to be differentiable at measurement intervals τ for which the slope of the graph departs appreciably from 2. The evidence in figures 5 and 6 implies that the ice does have a velocity and that it can be resolved with a sampling interval of about three hours.

Time averaged velocities can be defined without reference to the limiting process. Let $u(t,T,x)$ be the time averaged velocity at t.

$$u(t,T,x) = \frac{1}{T}\left[x(t+T/2,X) - x(t-T/2,X)\right] = \frac{1}{T}\int_{t-T/2}^{t+T/2} u(s,x)\,ds .$$

This quantity $u(t,T,x)$ and its properties depend on the duration T of the time averaging. For example, the variance of $u(t,T,x)$ will in general be less than the variance of $u(t,x)$ because the T average has suppressed contributions to the variance on shorter time scales. Also, from a dynamical point of view, the equations which $u(t,T,x)$ satisfies should involve T as a parameter. Different physical processes may be responsible for determining $u(t,T,x)$ for different values of T.

Typical ice velocities range from 0 to 20 cm sec^{-1}. An extreme velocity of 140 cm sec^{-1} has been observed. Two histograms of ice speed are shown in figure 7, one corresponding to a full year of observations, the other restricted to summer observations. The winter data contained several periods of essentially zero motion. During the summer the ice was never observed to stop.

In the following pages particular importance is attached to the time and space variability of the ice motion. We will often refer to the variance of velocity, $E((u-\bar{u})^2+(v-\bar{v})^2)=\rho^2$. This quantity has been evaluated from many observations; it varies appreciably with season and with location. Table II gives estimates of the velocity variance for each of the buoys shown in figure 3.

TABLE II

Variance of Velocity

1979 data, 1 point per day

Buoy ID	velocity variance	number of data points
1901	59 cm^2 sec^{-2}	342
1902	48	295
1903	50	284
1905	210	231
1906	81	299
1907	37	229
1908	174	61
1909	38	267
1911	19	62
1913	84	314
1914	83	282
1915	172	31
1916	57	172
1918	35	283
1917	29	219
1920	54	293
1923	63	302
1924	167	72
1925	67	280
1926	168	59
1927	62 (median)	311

5.3.1 Velocity time series

The ice velocities deduced from trajectories should be interpreted from the Lagrangian point of view since the measurements are made following the material particle. If many trajectories are measured simultaneously it is possible to obtain by interpolation velocity time series at fixed Eulerian points. Although the Lagrangian description is more directly measurable, it has the drawback of sampling both the time and space variations in velocity. The differences between the Lagrangian and Eulerian points of view is not of great practical importance in the motion of sea ice. This is because most of the variability in the ice motion is driven by the wind, and the space patterns in the wind field move across the basin so much faster than the ice moves, that all points, Lagrangian or Eulerian, experience essentially identical stochastic forcing. Consequently, Lagrangian and Eulerian time series of sea ice velocities look just about the same.

A typical velocity time series, taken from an ice station trajectory, say, will have a mean velocity usually less than 3 cm sec^{-1}, and it may show a trend. When these effects are removed from the time series what remains are the fluctuations with time scales longer than the sampling interval and shorter than the length of record T. The AIDJEX position data for instance, serve to resolve fluctuations on time scales from a few hours up to a few months, ($\tau \approx$ 1 hour, $T \approx$ 1 year). Over this range of time scales the ice velocity has a power spectral density as sketched in figure 8.

The power spectral density is plotted for positive and negative frequencies corresponding to counter-clockwise and clockwise rotations of the velocity vector. At the end of this section an algorithm is given for calculating the spectra of vector time series. We interpret the velocity vector time series $u(t, x)$ as a complex time series with the Fourier decomposition

$$u(t,x) = \int_{-\infty}^{\infty} a(\omega)\, e^{i\omega t} d\omega .$$

The power spectral density is the real function $S(\omega) = a(\omega)\, a^{*}(\omega)$, defined in the frequency range $-\frac{1}{2\tau} < \omega < \frac{1}{2\tau}$.

The integral of the spectral density over this frequency range is the variance $\frac{q^2}{T}$, and the integral over any frequency band is the part

of the total variance contributed by fluctuations with frequencies in that band. A useful way to summarize the information contained in the spectrum is to state the fraction of the total variance coming from frequencies greater than a certain value.

Table III Fraction of total variance exceeding certain frequencies

frequency:	1 cycle per month	2	4	15	30	60
period:	1 month	2 weeks	1 week	2 days	1 day	12 hours
	58%	45%	34%	12%	7%	3%

The equation of motion for sea ice balances the ice acceleration against air stress, water stress, pressure gradient forces due to the sloping sea surface, and internal ice stress gradients. While it is not the purpose here to examine the ice dynamics, it is useful to relate features of the ice velocity spectrum to these driving forces. In the central basin about 75% of the variance of the ice velocity can be explained by the local geostrophic wind (Thorndike and Colony, 1982). In fact, the ice velocity fluctuations are roughly proportional to the local wind fluctuations. This implies that the spectra of the ice velocity and of the wind should have approximately the same shapes (see figure 7).

The water stress depends on the difference in velocity between the ice and the upper ocean. If the ocean is at rest the water stress is simply a drag opposing the ice velocity and its only effect is to reduce the ice response near the inertial frequency. If the ocean is in motion, the ice will be carried along with it, and should acquire spectral traits similar to those of the ocean. Unfortunately the spectral signature of motion in the Arctic Ocean is not known. The long term circulation of the upper ocean appears to be similar to that of the ice, with a clockwise circulation in the Beaufort Sea and a transpolar current flowing from Siberia through the Greenland-Spitsbergen passage. It probably is not productive to ask whether the ice drives the long term ocean circulation or vice versa because, in the long term, the ice should be thought of as part of the upper ocean. In any case the long term ocean behavior does not affect the spectrum we are considering since we have subtracted out the long term mean velocity.

Fluctuations in ocean currents on shorter time scales have been observed but it is not yet possible to say how great their effect on the ice velocity may be. Some evidence for these variable currents is listed here.

1. Monthly variations are apparent in the currents deduced from wind and ice motion observations by Thorndike and Colony, 1982.

2. Subsurface eddies. Manley's (1981) study of subsurface eddies during AIDJEX described numerous features with velocity of about 50 cm sec^{-1}, a length scale of 10 kilometers, and a depth of 50-200 meters. He found no expression of these structures in the ice motion.

3. Inertial oscillations. The balance between the ice acceleration and the Coriolis force leads to oscillatory ice motion with a period which decreases from 12.77 hours at 70°N to 12 hours at 90°N. Inertial motions are always clockwise--hence the negative value for the frequency--in the Northern Hemisphere because the Coriolis force always accelerates the velocity to the right. Inertial motions in sea ice were first described by Hunkins (1967) and have received subsequent study by McPhee (1979) and Colony and Thorndike (1980). The amplitudes can reach 0.20 m sec^{-1} during summer when the ice pack is comparatively loose. Their effect on the summer ice velocity spectrum is striking (see figure 10).

4. Tides. Tidal currents in the central basin are small because of the great depth. Theoretical estimates are in the range of 1-2 cm sec^{-1}. Over the shallow continental shelves the amplitudes are predicted to be at least an order of magnitude greater (Kowalik and Untersteiner, 1978). These theoretical estimates are for the lunar semi-diurnal tide. Evidence from tide gauges around the basin summarized by Sverdrup (1926) implies that the lunar semi-diurnal (period 12.47 hr) and the solar semi-diurnal (12 hr) tides are the dominant tidal constituents in the Arctic Ocean.

The prediction of a large amplitude of the tidal current over the shelf is confirmed by Sverdrup's observations from the Maud; Nansen may also have observed tidal motion in the ice pack surrounding the Fram. Because the tidal and inertial periods are so close it may be difficult to diagnose observed motions correctly. Nevertheless there are several differences between the two kinds of motions which can sometimes be used to distinguish them. First the tidal vector traces out an ellipse during one period. An ellipse can be viewed as the sum of a clockwise circle and counter-clockwise circle. Thus, unless the tidal ellipse should happen to be exactly a clockwise circle, it should have some expression on the counter-clockwise

side of the spectrum. Inertial motion is strictly clockwise. Second, at a fixed point, tidal motions should have a fixed phase. Inertial motion on the other hand, acquires a new phase every time the ice receives a sudden impulse of momentum. Third, the phase of tidal motion should vary smoothly and slowly in space. Inertial motions at different points may have no fixed phase relationships.

The motion described by Sverdrup can hardly be mistaken for inertial motion. The smooth variations in phase as the Maud moved from Wrangel Island to the New Siberian Islands, and the clearly elliptical cycle described by the measured velocity vector are not compatible with inertial motions.

Most ice trajectories which have been analyzed in the western literature have been over the deep basin where the tidal motion is small. Careful observations and analysis would be required to detect a tidal component of order 1 cm sec^{-1} since it would be mixed with an inertial component which is often much larger and with a rich spectrum of other types of motions.

The Soviet literature contains many references to tidal motion in sea ice. Doronin and Kheisin (1977) and Zubov (1943) each devote several pages to the subject.

A consequence of the tidal motion is the associated cycle of convergence and divergence caused by the difference in phase of the tidal cycle at different points. Periodic opening and closing of the ice in the shallow seas has an effect on the heat exchange between the atmosphere and the ocean and on the rate of ice production. The theoretical calculations of Kowalik and Untersteiner indicate maximum divergence rates in the shallow seas exceeding $10^{-6} sec^{-1}$ which is enough to produce one percent opening during the tidal cycle. Their theoretical estimates of the divergence rate associated with tides over the deep ocean are three orders of magnitude smaller.

Calculation of cross power spectral density for two two-dimensional vector time series.

Given: two discrete complex time series u_i, v_i, $i = 1, \ldots, N$ with sampling interval τ.

Step 1. Select M, the number of lags; a good rule is $M < N/3$.

Step 2. Remove the mean and trend from each time series.

Step 3. Compute cross covariances

$$r_l = \begin{cases} \frac{1}{N} \sum_{j=1}^{N-l} u_{j+l} v_j^* & l = 0, 1, \cdots, M, \\ \frac{1}{N} \sum_{j=1-l}^{N} u_{j+l} v_j^* & l = -M, -M+1, \cdots, -2, -1. \end{cases}$$

Step 4. Define spectral window

$$w_\ell = \frac{1}{2}\left(1 + \cos\frac{\pi\ell}{M+1}\right) \qquad \ell = -M, \cdots, M .$$

Step 5. Calculate spectrum S and frequency ω

$$S_k = \tau \sum_{\ell=-M}^{M} w_\ell \tau_\ell e^{-\pi\ell k\sqrt{-1}/M}$$

$$k = -M, \cdots, M .$$

$$\omega_k = \frac{k}{2M\tau}$$

5.3.2 Velocity correlations in time.

An alternative characterization of a random function is its autocorrelation function. The discussion in the previous section of the power spectral density of the time function $u(t)$ at a fixed or moving point could have been given in terms of the autocorrelation function

$$R(\tau) = \frac{E\, u(t+\tau)\, u^*(t)}{E\, u(t)\, u^*(t)} = \frac{1}{\sigma^2} E\, u(t+\tau)\, u^*(t) .$$

The two functions $S(\omega)$ and $R(\tau)$ are Fourier transforms of each other and therefore contain equivalent information. Which description is the more useful depends on the application. The spectrum is useful for distinguishing physical processes with distinct characteristic frequencies; for example separating the free inertial oscillations from the wind forced motion. On the other hand the autocorrelation function is more useful for questions related to prediction or experiment design. For example the question: "How well can tomorrow's ice velocity be predicted on the basis of today's velocity," has an answer involving the autocorrelation function $R(\tau)$ evaluated at τ = 1 day.

The autocorrelation function is complex. Its real part contains information about the lagged correlations of the x component of velocity with itself

and the y component with itself. The imaginary part has information about the lagged correlations between the x and y velocity components. If the velocity of a piece of ice undergoing an inertial oscillation has a positive x component at a certain time, it will have a negative y component three hours later. The imaginary part of the correlation should have negative peaks at 3 hours, 15 hours, etc.

The autocorrelation function for the velocity time series at the AIDJEX ice station Caribou is shown in figure 11. The autocorrelation function estimated by the 1979 buoy data for the central basin is shown in figure 12. The real part of the correlation falls to about 0.7 after one day, 0.4 after two days, and decreases slowly at longer lags. The large correlation at lag one day indicates that persistence (the forecast strategy which predicts that the future will be the same as the present) will have some success for one day forecasts.

As expected the autocorrelation from Caribou has negative peaks in the imaginary part at 3 hours, 15 hours, etc. Generally though the imaginary part is small. If the inertial motions are not of interest in a particular application, the imaginary part of the autocorrelation function can safely be ignored. This is equivalent to treating the two velocity components as independent time series.

5.3.2.1 Application of the time autocorrelation function.

It is desired to estimate the ice velocity u at time t given observations z_j at times t_j, $j = 1, \cdots, N$. Suppose the observations have zero mean random errors $\varepsilon_j = z_j - u(t_j)$ which have covariance

$$E\varepsilon_j \varepsilon_k^* = \sigma^2 \delta_{jk} .$$

The delta function expresses the independence of errors at different times. Finally suppose the errors are independent of the actual velocities. Choose an estimator $\hat{u}$ which is a linear sum of the observations.

$$\hat{u} = \sum_{j=1}^{N} \alpha_j z_j$$

It is desired to find the complex constants α_j which give the best estimate $\hat{u}$ in the sense that $F(\alpha_1, \cdots \alpha_N) = E(\hat{u}-u)(\hat{u}-u)^*$ is minimized. This is accomplished by differentiating F with respect to the real and imaginary

parts of each α_j and equating to zero. The result is the system of complex equations for the unknowns $\alpha_1, \cdots, \alpha_N$:

$$\sum_j \alpha_j E z_j z_l^* = \left(E z_l u^*\right)^*$$

A further reduction is achieved by noting that

$$E z_j z_l^* = E u_j u_l^* + \sigma^2 \delta_{jl} \quad \text{and} \quad E z_l u^* = E u_l u^* \ .$$

Use of the matrix notation $Z = \{z_j\}$, $A = \{\alpha_j\}$, $M = \{E u_j u_l^* + \sigma^2 \delta_{jl}\}$, and $P = \{E u_l u^*\}$ gives the compact expressions

$$\hat{u} = A^T Z \quad \text{and} \qquad (1)$$
$$M^* A = P \ ,$$

which involve the autocorrelation function R and the measurement error variance σ^2. The estimation error is

$$F = q^2 - P^T M^{-1^T} P^* \ . \qquad (2)$$

With these two expressions we can answer a number of practical problems.

1. What sampling rate is required to insure good interpolation to the mid point between two observations? For given sampling interval τ and measurement error variance σ^2, we write eq. 1 as

$$\begin{pmatrix} q^2+\sigma^2 & q^2 R(\tau)^* \\ q^2 R(-\tau)^* & q^2+\sigma^2 \end{pmatrix} \begin{pmatrix} \alpha_1 \\ \alpha_2 \end{pmatrix} = \begin{pmatrix} q^2 R\left(\frac{\tau}{2}\right)^* \\ q^2 R\left(-\frac{\tau}{2}\right)^* \end{pmatrix}$$

The solutions for the α_j, which in this case are complex conjugates for reasons of symmetry, and for F are sketched in figure 13. The solution technique extends trivially to interpolation involving more points.

The optimal choice of the weights α_1 and α_2 is not $\alpha_1 = \alpha_2 = 1/2$. This linear interpolation between the two data points is the most natural scheme, and it is quite good for small τ, and small σ^2/q^2, but it is not the optimal interpolation. Especially at large τ, a smaller error variance is achieved by giving less weight to the observations. For very large τ the optimal estimate is simply $\hat{u}=0$, $(\alpha_1 = \alpha_2 = 0)$ since, in this case the two observations are so removed in time as to have no correlation with the desired velocity.

The measurement error σ affects α_j and F slightly. The dependence of F on the sampling interval τ is quite strong. It appears that if one needs to know each velocity component to $\pm$ 3 cm sec^{-1}, $F = F\varepsilon_u^2 + \varepsilon_v^2 =$ 18 cm sec^{-1}, a sampling interval of about six hours is required even with perfect measurements.

2. What errors are expected in forecasts based only on the present velocity? Here we obtain

$$\alpha = \frac{R(\tau)^*}{1+\sigma^2/q^2} \qquad (3)$$

$$F/q^2 = 1 - \frac{R(\tau)R(\tau)^*}{1+\sigma^2/q^2}$$

The forecast error is plotted for two values of initial error in figure 14.

The prediction error grows with time, approaching the velocity variance q^2 for large τ. From the sketch we see that an optimal 3 hour forecast captures about 75% of the velocity variance, an optimal one day forecast captures about 35% of the variance.

The velocity was assumed to have zero mean in this analysis and, in constructing the autocorrelation function (figures 11, 12), the long term mean was first removed from the data. In an actual application to a region where the mean is known the best forecast would be

$$\hat{u} = \bar{u} + \alpha(z - \bar{u}) .$$

Note that the best forecast is not simple persistence ($\alpha = 1$). For long forecasts, the best estimate is the mean ($\alpha = 0$), as equation 3 correctly indicates.

5.3.2.1 Acceleration

The time autocorrelation function for velocity, figures 11 and 12, behaves like $1 - \tau/c$ for small τ. It follows from this that the variance of the increment in velocity $u(t+\tau) - u(t)$ is proportional to τ (not τ^2). This implies that the velocity is not time differentiable in the mean square sense. Attempts to measure accelerations precisely by sampling over shorter and shorter time intervals may merely result in larger and larger estimates of acceleration. Of course, time averaged accelerations exist and have finite variance.

$$\sigma_a^2 = \mathrm{var}\left\{\frac{1}{T}\left[u(t+T) - u(t)\right]\right\} = \frac{2q^2}{T^2}\left(1 - R(T)\right)$$

which for small T is $2q^2/cT$ with $c \approx 10^5$ sec.

It is frequently claimed that the inertial forces due to acceleration of the ice are small compared to other forces acting on the ice. To support this claim a typical average acceleration σ_a is compared for instance, to a typical value of the Coriolis acceleration $f\sigma_u \approx 10^{-4}\,sec^{-1} \cdot 10\,cm\,sec^{-1}$. Using the above estimate for σ_a, and taking $\rho^2 = 100\,cm^2\,sec^{-2}$, we find $\sigma_a < f\sigma_u$ provided $T > 2\times10^3\,sec$. Thus, roughly a half hour time average is required to bring the acceleration down to the level of other terms in the momentum balance.

5.3.3 Velocity correlations in space

In earlier sections the emphasis has been on the structure of the complex function u of the real argument t, at a fixed or moving point. In this section, the emphasis is on u as a function of position for fixed time. Certain results are more easily expressed if u and x are regarded as two dimensional vectors rather than as complex numbers. The autocorrelation function

$$\rho^2 R(\underset{\sim}{x}_1, \underset{\sim}{x}_2) = E\,\underset{\sim}{u}(\underset{\sim}{x}_1)\,\underset{\sim}{u}^T(\underset{\sim}{x}_2) = \begin{pmatrix} E\,u(\underset{\sim}{x}_1)u(\underset{\sim}{x}_2) & E\,u(\underset{\sim}{x}_1)v(\underset{\sim}{x}_2) \\ E\,u(\underset{\sim}{x}_2)v(\underset{\sim}{x}_1) & E\,v(\underset{\sim}{x}_1)v(\underset{\sim}{x}_2) \end{pmatrix}$$

is a 2 x 2 matrix involving possibly four different functions, whereas the time autocorrelation function involves just two.

The structure of the spatial autocorrelation matrix for sea ice velocities reveals some of the properties of the velocity field. To establish the basic ideas we first determine the structure of the autocorrelation matrix for a homogeneous, isotropic, two dimensional velocity field, borrowing from Kolmogroff's (1941) classic discussion of three dimensional turbulence.

A random field is said to be homogeneous if its statistical properties are invariant under a translation of coordinates, and isotropic if they are invariant under rotations and reflections of coordinates. In particular the autocorrelation matrix for a homegeneous isotropic field must satisfy

$$R(\underset{\sim}{x}_1, \underset{\sim}{x}_2) = R(\underset{\sim}{x}_1 + \underset{\sim}{a}, \underset{\sim}{x}_2 + \underset{\sim}{a}) \qquad \text{for any } \underset{\sim}{a}, \text{ and}$$

$$\rho^2 R(\underset{\sim}{x}_1, \underset{\sim}{x}_2) = E\,\underset{\sim}{u}(\underset{\sim}{x}_1)\,\underset{\sim}{u}^T(\underset{\sim}{x}_2) = E\,M\underset{\sim}{u}(M\underset{\sim}{x}_1)\left[M\underset{\sim}{u}(M\underset{\sim}{x}_2)\right]^T$$

for any orthonormal matrix M. Multiplication by an orthonormal matrix

accomplishes an arbitrary rotation or reflection of coordinates. Note that the change of coordinates is applied to both the position and the velocity vectors. These definitions make precise the notions that the statistics do not depend on position or direction. By choosing the translation vector $\underset{\sim}{a}$ or the rotation and reflection matrix M suitably, we can see how these definitions of homogeneity and isotropy constrain the form of the autocorrelation matrix.

First, $R(\underset{\sim}{x}_1, \underset{\sim}{x}_2)$ depends only on the vector difference $\underset{\sim}{x}_2 - \underset{\sim}{x}_1$. To see this, take $\underset{\sim}{a} = -\underset{\sim}{x}_1$. Note that this does not imply that R depends only on the distance $\|\underset{\sim}{x}_2 - \underset{\sim}{x}_1\|$.

Second, R is symmetric. This requires using $\underset{\sim}{a} = -\underset{\sim}{x}_1$, $M = -I$ and $\underset{\sim}{a} = \underset{\sim}{x}_2$, to obtain this sequence of equalities:

$$E\,u(\underset{\sim}{x}_1)\,v(\underset{\sim}{x}_2) = E\,u(\underset{\sim}{0})\,v(\underset{\sim}{x}_2 - \underset{\sim}{x}_1) = E\big(-u(-\underset{\sim}{0})\big)\big(-v(\underset{\sim}{x}_1 - \underset{\sim}{x}_2)\big) = E\,u(\underset{\sim}{x}_2)\,v(\underset{\sim}{x}_1).$$

Third, $E\,u(0,0)\,v(x,0) = 0$. Here use the reflection invariance in the definition of isotropy by taking

$$M = \begin{pmatrix} 1 & 0 \\ 0 & -1 \end{pmatrix}$$

which changes the sign of the y axis. Then

$$E\,u(0,0)\,v(x,0) = E\,u(0,-0)\,[-v(x,-0)] = -E\,u(0,0)\,v(x,0)$$

which is only true when $E\,u(0,0)\,v(x,0) = 0$.

Consequently the autocorrelation function evaluated at $x_1 = (0,0)$, $x_2 = (r,0)$ has the form

$$R\big((0,0),(r,0)\big) = \frac{1}{q^2}\begin{pmatrix} E\,u(0,0)\,u(r,0) & 0 \\ 0 & E\,v(0,0)\,v(r,0) \end{pmatrix} = \begin{pmatrix} B_{\parallel}(r) & 0 \\ 0 & B_{\perp}(r) \end{pmatrix} = \mathbb{B}(r)$$

involving only two function of distance. $B_{\parallel}(r)$ is the correlation between the components of velocity parallel to the line joining two points separated by a distance r. $B_{\perp}(r)$ is the correlation between the components of velocity perpendicular to that line.

More generally if $\underset{\sim}{x}_1$ and $\underset{\sim}{x}_2$ are arbitrary points with $r^2 = (x_1 - x_2)^2 + (y_1 - y_2)^2$, $\cos\theta = (x_2 - x_1)/r$ and $\sin\theta = (y_2 - y_1)/r$, then

$$\underset{\sim}{u} = \begin{pmatrix} u \\ v \end{pmatrix} = A \begin{pmatrix} u_{\parallel} \\ u_{\perp} \end{pmatrix} = A\,\tilde{\underset{\sim}{u}} \quad \text{where} \quad A = \begin{pmatrix} \cos\theta & -\sin\theta \\ \sin\theta & \cos\theta \end{pmatrix}.$$

Then $R(\underset{\sim}{x}_1, \underset{\sim}{x}_2) = \frac{1}{q^2} E\,\underset{\sim}{u}(\underset{\sim}{x}_1)\,\underset{\sim}{u}^T(\underset{\sim}{x}_2) = \frac{1}{q^2} E\,A\,\tilde{\underset{\sim}{u}}(\underset{\sim}{x}_1)\left(A\,\tilde{\underset{\sim}{u}}(\underset{\sim}{x}_2)\right)^T = A\,B(r)\,A^T$ or

$$R(\underset{\sim}{x}_1, \underset{\sim}{x}_2) = \begin{pmatrix} \cos^2\theta\, B_{\parallel}(r) + \sin^2\theta\, B_{\perp}(r) & \cos\theta\sin\theta\,\left(B_{\parallel}(r) - B_{\perp}(r)\right) \\ \cos\theta\sin\theta\left(B_{\parallel}(r) - B_{\perp}(r)\right) & \sin^2\theta\, B_{\parallel}(r) + \cos^2\theta\, B_{\perp}(r) \end{pmatrix} \qquad (4)$$

which is the general form for the autocorrelation matrix for a homogeneous, isotropic two dimensional velocity field. It involves two functions, $B_{\parallel}$ and $B_{\perp}$, which we will estimate below from observations. Further it involves the separation r and the orientation θ of the two points $\underset{\sim}{x}_1$ and $\underset{\sim}{x}_2$ at which the autocorrelation is being evaluated. It may seem strange that θ enters the statistics for an isotropic field. The condition of isotropy does not imply that $E\,u(0,0)\,u(r,0)$ equals $E\,u(0,0)\,u(0,r)$ however. A rotation of coordinates affects both the velocity and the position vectors. A valid statement is $E\,u(0,0)\,u(r,0) = E\,v(0,0)\,v(0,r)$ See figure 15.

There is another constraint on the spatial correlation function. Let $\underset{\sim}{u}_i = (u_i, v_i)$ be the velocities at any set of points $\underset{\sim}{x}_i$, $i=1,\cdots,N$ and let γ_i, η_i be arbitrary real numbers. Then the linear sum

$$S = \sum_{i=1}^{N} \gamma_i u_i + \eta_i v_i$$

has a variance which can be expressed in terms of R. The added constraint is that $\mathrm{var}(S) \geq 0$ for all choices of $\underset{\sim}{x}_i$, γ_i, and η_i. This requires that the matrix consisting of the correlations of the velocity component at any set of points $\{\underset{\sim}{x}_i\}$ must be positive definite (all positive eigenvalues), and is equivalent to the condition that the two dimensional spatial power spectrum of velocity be positive for all pairs of wave numbers (n_x, n_y).

Contradictions can arise if correlation functions are used which do not satisfy this constraint. For example, suppose we wish to consider a velocity field for which $B_{\parallel}(0) = 1$, $B_{\parallel}(L) = 0.9$ and $B_{\parallel}(2L) = 0.5$. The attempt to evaluate the variance of $S = u(0,0) - 1.3\,u(L,0) + 0.4\,u(2L,0)$ in terms of these correlations produces a negative result. Since variance is intrinsically positive, we must conclude that no velocity field could have the presumed correlations.

As an example of an analytical form for R which satisfies the positive definite constraint and bears some resemblance to reality, define

$$B_{\parallel}(r) = e^{-(r/A)^2} \quad , \quad B_{\perp}(r) = \left(1 - 2\left(\frac{r}{A}\right)^2\right) e^{-(r/A)^2} \quad , \quad A \sim 900\ \text{km}$$

This example was constructed by taking a stream function Ψ with the positive definite correlation function $R(r) = e^{-r^2/A^2}$. The corresponding power spectrum is the Hankel transform of e^{-r^2/A^2} . This is $\pi A^2 e^{-\omega^2 A^2/4}$ $\left(\omega^2 = n_x^2 + n_y^2\right)$, which is always positive. Now define velocity components $u = -\partial\Psi/\partial y$, $v = \partial\Psi/\partial x$ and deduce $B_{\parallel}(r) = -\frac{1}{r}\frac{\partial R(r)}{\partial r}$ and $B_{\perp}(r) = -\frac{\partial^2 R(r)}{\partial r^2}$.

5.3.3.1 Estimates of the autocorrelation functions.

In order to estimate the autocorrelation matrix, simultaneous velocity observations are required at pairs of points separated by distances ranging from roughly 1 to 10^3 kilometers. We present data from the 1979 buoy program and from AIDJEX which define the functions $B_{\parallel}$ and $B_{\perp}$ only for distances exceeding 100 kilometers. The 1979 data were first interpolated to give velocity estimates at a uniform grid in space and time.

$$u_{ijk} = u(x_i, y_j, t_k) \quad , \quad \Delta x = \Delta y = 400\ \text{km} \ , \ \Delta t = 1\ \text{day} \ , \ i = 1, \cdots N_x \ , \ j = 1, \cdots, N_y \ , \ k = 1, \cdots, N_t \ .$$

The mean velocity over all points i,j,k was removed. Then for lags ℓ, m, n the lagged correlations were found using

$$R_{\ell,m,n} = \frac{1}{N_x N_y N_t} \sum_{i=1}^{N_x - \ell} \sum_{j=1}^{N_y - m} \sum_{k=1}^{N_t - n} \underset{\sim}{u}_{i+\ell,\, j+m, k+n} \ \underset{\sim}{u}^{T}_{ijk}$$

For these calculations $N_x = 7$, $N_y = 4$, and $N_t = 200$. The results are sketched in figure 16 for the lags $\ell = 1, \ldots, 7$, $m = n = 0$, and $\ell = n = 0$, $m = 1, \ldots, 4$. The results show that $E\,u(0,0)\,u(\tau,0)$ and $E\,v(0,0)\,v(0,\tau)$ are similar functions of τ , and that $E\,v(0,0)\,u(\tau,0)$, $E\,u(0,0)\,v(0,\tau)$, $E\,u(0,0)\,v(\tau,0)$, and $E\,v(0,0)\,u(0,\tau)$ are all small. These observations are roughly consistent with the assumption that the field is homogeneous and isotropic. We will proceed then on the assumption, supported by these data, that the ice has a homogeneous, isotropic velocity field with the functions $B_{\parallel}$ and $B_{\perp}$ empirically determined from figure 16 .

Correlations for the AIDJEX data were constructed by choosing two of the ice camps, resolving their velocities into components parallel and perpendicular to the line joining the camps, and correlating these components.

These correlations are also plotted in figure 16.

5.3.3.2 Applications of the space correlation.

The spatial autocorrelation function is the basis for sound experiment design and data processing. For instance, suppose observations of velocity $\underset{\sim}{u}_i$ are made at N points $\underset{\sim}{x}_i$ with independent zero mean errors having variance σ^2. Estimates of velocity are to be made at arbitrary points $\underset{\sim}{x}$ using these observations. What is the maximum estimation error? We use the tools developed earlier. To estimate the u component of velocity at $\underset{\sim}{x}$, we use the observations $\underset{\sim}{u}_1, \cdots, \underset{\sim}{u}_N$ and construct the matrices

$$\begin{pmatrix} R_{u_1u_1}+\sigma^2 & R_{u_1v_1} & R_{u_1u_2} & \cdots & R_{u_1v_N} \\ R_{v_1u_1} & R_{v_1v_1}+\sigma^2 & R_{v_1u_2} & & \\ R_{u_2u_1} & R_{u_2v_1} & & & \\ \vdots & & & & \\ R_{v_Nu_1} & \cdots & & & R_{v_Nv_N}+\sigma^2 \end{pmatrix} \begin{pmatrix} \alpha_1 \\ \beta_1 \\ \vdots \\ \alpha_N \\ \beta_N \end{pmatrix} = \begin{pmatrix} R_{uu_1} \\ R_{uv_1} \\ R_{uu_2} \\ \vdots \\ R_{uu_N} \\ R_{uv_N} \end{pmatrix}$$

where $R_{u_iv_j} = E\, u(\underset{\sim}{x}_i)\, v(\underset{\sim}{x}_j)$ etc. as given by Eq. 4. The estimation error variance is given by Eq. 2. Figure 17 shows how the maximum estimation error depends on the separation between measurement stations and on the measurement accuracy. The curve labelled $\sigma^2/\phi^2 = 0$ refers to the idealized condition in which the measurement errors are zero. Thus it represents the interpolation error which is due to the intrinsic spatial variability of the velocity field.

The standard deviation of the ice velocity itself is about $\phi \sim 10$ cm sec^{-1}. A reasonable observational goal is to keep the interpolation errors below 2 or 3 cm sec^{-1}. This can be achieved if the raw measurements of velocity are good to about 3 cm sec^{-1} and the grid spacing is about 400 km. At larger grid spacings the interpolation accuracy deteriorates rapidly.

5.4 Deformation

The differences in velocity from place to place are responsible for the characteristic morphology of the ice. When the velocity difference between neighboring pieces of ice is such that they tend to move apart, a lead forms and widens exposing the ocean surface to the atmosphere. During the winter, ice growth is rapid over open leads. If the motion changes--perhaps because

of a change in the winds--so that these pieces of ice move toward each other, the open lead will close, and any new ice which formed there will need to rearrange itself to occupy a smaller area. Typical mechanisms for this rearrangement are rafting where one part of the new ice sheet overrides the other, and ridging where the ice is crushed into pieces which pile into ridges rising a meter or two above and sometimes many meters below the surrounding ice. Ridging and rafting are not restricted to thin ice. If the closing motion continues, the original pieces of ice come in contact and one may override the other or, by grinding together, pieces may break off and pile up and down to form a ridge. The essential ideas here are that the ice accommodates divergent motion by increasing the area of open water rather than by stretching and thinning. It accommodates convergent motion by reducing the area of open water and by ridging and rafting. These processes link the morphology of the ice, characterized by such features as floes, ridges, and leads, to the spatial differences in the ice velocity. By studying the spatial variations in velocity we may be able to understand better why the ice pack has the form it does.

There is a second reason for studying the deformation of sea ice. As the ice pack deforms, stresses develop within it which tend to oppose the deformation. These stresses figure into the local balance of forces and therefore affect the motion of the ice. To be more precise, the balance of forces equation contains terms of the form $\partial\sigma_{ij}/\partial x_i$ where σ_{ij} is the stress tensor. The stresses may in turn be related to the ice motion by a constitutive law

$$\text{stress} = F(\text{deformation}).$$

One of the motivations for AIDJEX was to investigate the function F from a theoretical point of view and by using observations of the deformation and indirect estimates of the stress (see Rothrock et al., 1980).

The concepts which have been applied to the study of the spatial variations in ice velocity are those appropriate to the analysis of the deformation of a continuum. The fundamental concepts are the partial derivatives of $u(x,y,t)$ and $v(x,y,t$ with respect to x and y. The line of thought is that a description of the large scale deformation in terms of large scale average derivatives should give some idea of how much opening and closing is going on on smaller scales and some idea of the state of stress. For

example under a purely divergent motion only leads are formed. During a purely convergent motion no leads are formed. On a small scale, shearing along a crack is of no morphological consequence. But large scale shearing is often expressed locally by opening at some cracks and closing at others.

Mathematical formulation of these ideas requires two steps. Required first is an appropriate quantitative description of the large scale deformation in terms of observable parameters. The second requirements is for a functional relationship giving the opening, closing, or state of stress in terms of the observable parameters.

Current practice is to describe the motion in terms of the large scale strain rate invariants, which themselves are constructed from the large scale velocity derivatives. The first invariant

$$E_I = \frac{\partial u}{\partial x} + \frac{\partial v}{\partial y}$$

quantifies the large scale divergence and convergence, and the second invariant

$$E_{II} = \left[\left(\frac{\partial u}{\partial x} - \frac{\partial v}{\partial y} \right)^2 + \left(\frac{\partial u}{\partial y} + \frac{\partial v}{\partial x} \right)^2 \right]^{1/2}$$

quantifies the rate of shearing. A useful alternative pair of invariants is $(|E|, \theta)$, where

$$|E| = \left[E_I^2 + E_{II}^2 \right]^{1/2}$$

expresses the total rate of deformation and

$$\theta = \tan^{-1} \frac{E_{II}}{E_I} \qquad 0 \le \theta < \pi$$

indicates whether the motion is predominantly divergence $\theta \sim 0$, shear $\theta \sim \pi/2$ or convergence $\theta \sim \pi$.

In the theory presented by Thorndike et al., 1975, opening and closing are assumed to be known functions of θ and proportional to $|E|$.

$$A = \text{total opening} = |E| \, \alpha_o(\theta) ,$$

$$C = \text{total closing} = |E| \, \alpha_c(\theta) .$$

The functions α_o and α_c which give the total opening and closing in terms of the strain rate invariants may have a form somewhat as sketched in figure 18. Some constraints on the shapes of these functions have been deduced by Nye, 1975 and by Rothrock and Hall, 1975. From pairs of Landsat images of the ice these investigators were able to measure the strain invariants and the total opening and closing.

C-2

The functional relationships for A and C in terms of $|E|$ and θ can only be regarded as approximate since they do not take into account the actual geometry of the floes in the region being considered. Different regions with different geometries will respond differently to similar large scale strain rates.

In practical applications of these ideas the procedure has been to take measured velocities at several points in a region of interest--perhaps the three corners of a 100 km triangle. Velocity derivatives are estimated from the measured velocities. The estimated velocity derivatives are combined to form the strain rate invariants $|E|$ and θ, and these are used to find the rates of opening and closing A and C, and the state of stress σ.

In the following sections we reexamine some of these ideas, particularly the notion of velocity derivatives, the influence of the ice pack geometry on opening and closing, and the difficulties in basing inferences about these quantities on small numbers of measurements.

5.4.1 Velocity derivatives

Since the ice pack is made up of discrete pieces moving relative to each other, the variations in velocity have two types:

1) for any $\underset{\sim}{x}_1$ and $\underset{\sim}{x}_2$ on the same rigid piece, the linear relation

$$\underset{\sim}{u}(\underset{\sim}{x}_2) - \underset{\sim}{u}(\underset{\sim}{x}_1) = \begin{pmatrix} \cos\omega & -\sin\omega \\ \sin\omega & \cos\omega \end{pmatrix} (\underset{\sim}{x}_2 - \underset{\sim}{x}_1)$$

must hold, where ω is a constant related to the rate of rotation of the rigid piece.

2) for $\underset{\sim}{x}_1$ and $\underset{\sim}{x}_2$ on separate pieces,

$$\underset{\sim}{u}(\underset{\sim}{x}_2) - \underset{\sim}{u}(\underset{\sim}{x}_1)$$

is arbitrary.

If we select a random point (x,y) on an ice floe, the partial derivative of velocity,

$$\frac{\partial u}{\partial x}(x,y,t) = \lim_{h\to 0} \frac{u(x+h,y,t) - u(x,y,t)}{h}$$

is well defined because for small enough h, (x,y), and $(x+h,y)$ almost always lie on the same floe and the linearity of the first type of motion mentioned above implies the existence of the limit. Thus the partial derivative exists, but it describes only the rigid body rotation of a floe. It

says nothing about the relative motion between floes which is after all the motion causing the opening and closing and the exchange of momentum between floes.

To include the effect of velocity differences between floes we cannot let h become arbitrarily small. Consider the velocity increment $u(x+h,y,t) - u(x,y,t)$ where (x,y) is fixed and h begins at 100 km and decreases to the smallest value h_o such that $(x+h_o, y)$ and (x,y) lie on separate floes. This increment captures the variation in velocity from floe to floe and has nothing to say about the rigid rotation of the floe (x,y) lies on. The velocity increment will generally decrease as h approaches h_o, and we can examine the characteristic rate of decrease by evaluating the variance $E\left(u(x+h,y,t) - u(x,y,t)\right)^2$. If this quantity is proportional to h^2 for small h, the velocity at least has a derivative in the mean square sense.

The best data available for examining the variance of velocity increments for a range of spacings were extracted from SEASAT synthetic aperture imaging radar by Hall and Rothrock, 1981. By comparing two images separated by three days, they were able to measure the displacement of enough ice features to resolve considerable spatial detail in one dimension of the ice motion. After interpolating to evenly spaced points x_i their data have the form

$$\left\{ u(x_i) \;,\; v(x_i) \right\} \qquad i = 1, \cdots, N \;, \quad \Delta x = 2 \text{ km}.$$

For $h = 1, \ldots,$ the h-increments were defined as

$$I_u(h,i) = u(x_{i+h}) - u(x_i)$$
$$I_v(h,i) = v(x_{i+h}) - v(x_i).$$

The variance of the increments was estimated from the $\left\{ I_u(h,i), I_v(h,i) \right\}$, $i = 1, \cdots N-h$ with the results plotted in figure 17. The linearity of the log-log plot for small h supports a power law relationship with $\text{var}\,(I(h)) = c\,h^{\alpha}$ with α in the neighborhood of 1.1 to 1.3. It appears then that the increments do not decrease as fast as h^2, and therefore the velocity does not have a derivative in the mean square sense.

The statement just made for the variance of increments can be recast in terms of the autocorrelation function. It implies that for small τ

$$B_{\parallel}(\tau) \;,\; B_{\perp}(\tau) \;\sim\; 1 - \frac{c}{2}\tau^{\alpha}$$

thus helping to define the shape of $B_{\parallel}$ and $B_{\perp}$ at $r=0$. At $r=c$, $B_{\parallel}$ and $B_{\perp}$ have the value unity, are continuous, have a continuous first derivative of zero, but fail to have a second derivative.

5.4.2 Velocity differences

The definition of the derivative as a limit could be discarded in favor of a velocity difference over a finite distance,

$$u_{x,L}(x,y,t) = \frac{1}{L}\left[u(x+L,y,t) - u(x,y,t)\right]$$

and similar definitions for $u_{y,L}$, $v_{x,L}$, and $v_{y,L}$.

There is no question about the existence of these differences. Definitions for strain rate invariants follow naturally by associating $u_{x,L}$ with $\partial u/\partial x$ etc. in the earlier definitions. When L is chosen to be of order 100 km, these definitions can be used to describe the large scale deformation.

There are several problems with this approach. First, the L-differences carry no information about smaller scales. Second, no basis has been given for choosing a particular value for L. Third, measurements of velocity are rarely available at uniformly spaced points. Still most analyses of sea ice strain have been done with a length scale implicitly fixed by the scale of the observations. To interpret these analyses we must determine the role played by L.

Consider the covariances between the various L-differences. These follow from the covariance structure of the velocity itself. For example

$$E\, u_{x,L}(0,0,t)\, u_{x,L}(r,0,t) = \frac{1}{L^2} E\Big(u(L,0,t)-u(0,0,t)\Big)\Big(u(r+L,0,t)-u(r,0,t)\Big)$$

$$= -\frac{a^2}{L^2}\left[B_{\parallel}(r+L) - 2B_{\parallel}(r) + B_{\parallel}(r-L)\right] . \qquad (5)$$

To interpret this equation, suppose the L-difference $u_{x,L}$ is measured at two points separated by a distance r along the x axis. The right hand side of equation 5 approximates the second derivative of $B_{\parallel}$ at r. For small r, $B_{\parallel}$ is concave down so the two L-differences are positively correlated. At some value of r, $B_{\parallel}(r)$ has an inflection point. Over such a distance the L-differences become uncorrelated; at longer distances the L-differences are negatively correlated. This example has been worked

for the $u_{x,L}$ component at points separated along the x-axis, but the same procedure can be used to correlate any two first velocity differences at any two points.

It is apparent from this and figure 16 that quantities related to the L-differences are highly correlated in space only over distances of less than about 400 km. Furthermore this statement is not sensitive to the choice of L, since the expression 5 will change sign at approximately the same r, independent of L. The correlation length scale for velocity by comparison is roughly twice as large (see figure 16).

The ice velocities are well correlated at distances of up to 1000 km, as evidenced by the patterns in the long term ice motion (figures 2-4) and in shorter term motions (see Thorndike and Colony, 1980 for instance). It may seem surpising not to find similar patterns in the strain fields. The reason why such patterns are not found is that the strain field has, by equation 5, and figure 16, a correlation length scale of only a few hundred kilometers. Measurement arrays like the 1979 and 1980 buoy arrays with a buoy spacing of roughly 500 kilometers are too coarse to resolve patterns in the strain field.

For the example just worked we can find the variance of the L-difference by setting $r = 0$.

$$E\, u_{x,L}^2 = \frac{2q^2}{L^2}\left(1 - \beta_{\parallel}(L)\right).$$

The symmetric matrix of covariances between pairs of L-differences at the same point is

	$u_{x,L}$	$v_{y,L}$	$u_{y,L}$	$v_{x,L}$
$u_{x,L}$	$\frac{2q^2}{L^2}\left[1-\beta_{\parallel}(L)\right]$	$-\frac{q^2}{2L^2}\left[\beta_{\parallel}(\sqrt{2}L)-\beta_{\perp}(\sqrt{2}L)\right]$	$\frac{q^2}{L^2}\left[1+\overline{\beta}(\sqrt{2}L)-2\overline{\beta}(L)\right]$	0
$v_{y,L}$		$\frac{2q^2}{L^2}\left[1-\beta_{\parallel}(L)\right]$	0	$\frac{q^2}{L^2}\left[1+\overline{\beta}(\sqrt{2}L)-2\overline{\beta}(L)\right]$
$u_{y,L}$			$\frac{2q^2}{L^2}\left[1-\beta_{\perp}(L)\right]$	$-\frac{q^2}{2L^2}\left[\beta_{\parallel}(\sqrt{2}L)-\beta_{\perp}(\sqrt{2}L)\right]$
$v_{x,L}$				$\frac{2q^2}{L^2}\left[1-\beta_{\perp}(L)\right]$

where $\overline{\beta} = \frac{1}{2}\left(\beta_{\parallel}+\beta_{\perp}\right)$.

This matrix can be evaluated at L = 400 km for example by reading points from the plotted functions $\beta_{\parallel}$ and $\beta_{\perp}$ in figure 16.

	$u_{x,L}$	$v_{y,L}$	$u_{y,L}$	$v_{x,L}$
$u_{x,L}$	$3.9\times10^{-14}\,sec^{-2}$	$-0.8\times10^{-14}\,sec^{-2}$	$1.4\times10^{-14}\,sec^{-2}$	0
$v_{y,L}$		$3.9\times10^{-14}\,sec^{-2}$	0	$1.4\times10^{-14}\,sec^{-2}$
$u_{y,L}$			$6.1\times10^{-14}\,sec^{-2}$	$-0.8\times10^{-14}\,sec^{-2}$
$v_{x,L}$				$6.1\times10^{-14}\,sec^{-2}$

$L = 400$ km
$\frac{q^2}{T} = 10^2\,cm^2\,sec^{-2}$

The covariance matrix for the L-differences illustrates several properties of the way the ice deforms. Notice that the variances of the parallel differences $u_{x,L}$ and $v_{y,L}$ are smaller than the perpendicular differences $u_{y,L}$ and $v_{x,L}$. The parallel differences relate to the linear stretching and contracting of the ice pack. The perpendicular differences relate to shear and rotation. Apparently the second type of motion is greater, but recall the word of caution given earlier that the interpretation of this kinematic evidence is ambiguous. We cannot say whether the observed motion reflects some property of the ice pack or some characteristic of the driving forces.

With the L-differences one could define L-strains in a natural way. The statistics in Table IV of the L-strains follow from the above matrix. These values predict, on the basis of the spatial correlations above, that the large scale divergence will typically be smaller than the vorticity and shear, a prediction verified by many different sets of observations.

TABLE IV

Typical strain rates as a function of gauge length L.

L-strain		variance	L-strain in percent per day for various L, using $\frac{q^2}{T} = 10^2\,cm^2\,sec^{-2}$			
			L: 100 km	200 km	400 km	800 km
divergence	$u_{x,L}+v_{y,L}$	$\frac{q^2}{L^2}\left[4-4B_{\parallel}(L)-B_{\parallel}(\sqrt{2}L)+B_{\perp}(\sqrt{2}L)\right]$	1.6	2.2	2.2	1.6
vorticity	$u_{y,L}-v_{x,L}$	$\frac{q^2}{L^2}\left[4-4B_{\perp}(L)+B_{\parallel}(\sqrt{2}L)-B_{\perp}(\sqrt{2}L)\right]$	4.3	3.7	3.2	2.2
shear	$u_{x,L}-v_{y,L}$	$\frac{q^2}{L^2}\left[4-4B_{\parallel}(L)+B_{\parallel}(\sqrt{2}L)-B_{\perp}(\sqrt{2}L)\right]$	3.1	3.0	2.6	1.8
	$u_{y,L}+v_{x,L}$	$\frac{q^2}{L^2}\left[4-4B_{\perp}(L)-B_{\parallel}(\sqrt{2}L)+B_{\perp}(\sqrt{2}L)\right]$	3.4	3.1	2.8	2.0

5.4.3 Deformation measurements

Several studies have been made over the past decade or so using observations of velocity at an array of stations, with the objective of monitoring the large scale deformation of the region covered by the array. While it is never stated just this way, the implicit definition of large scale deformation appears to involve spatially averaged derivatives over the region,

$$\overline{\frac{\partial u}{\partial x}} = \frac{1}{A} \int_R \frac{\partial u}{\partial x} \, da$$

where A is the area of the region R sampled by the array. Similar expressions define the other large scale average velocity gradients. Application of the Green-Gauss theorem implies

$$\overline{\frac{\partial u}{\partial x}} = \frac{1}{A} \oint_C u \, \underset{\sim}{n} \cdot \underset{\sim}{\hat{i}} \, dl \qquad (6)$$

where $\underset{\sim}{n}$ is the outward normal to the perimeter C of R, and $\underset{\sim}{\hat{i}}$ a unit vector in the x direction.

Note the difference between the L-difference and the large scale average derivative. The former can be measured exactly as $u(x+L,y) - u(x,y)$; the latter requires measurements at every point around a closed curve. In the next section we will discuss how many measurements are required to achieve a desired accuracy in the large scale deformations. But first we review some of the results of the studies just alluded to.

In these studies the deformation estimates were made by finding the linearly varying velocity field which most closely fit the observed velocities at an array of points within R.

$$\underset{\sim}{u}(\underset{\sim}{x}) = \underset{\sim}{u}_0 + M \underset{\sim}{x}$$

where the matrix M contains the four large scale average velocity partial derivatives. M and $\underset{\sim}{u}_0$ are determined using a least squares fit of the observed velocities $\underset{\sim}{u}$ and positions $\underset{\sim}{x}$. The strain rate invariants were then computed from the elements in M.

The values, given in Table V, confirm some of the results deduced above from the observed spatial correlation functions. For example the standard deviations of vorticity and shear are generally larger than the standard deviation of divergence. Note also that the mean divergence is small compared to the mean vorticity and shear.

TABLE V

Statistics of Sea Ice Deformation.

All deformations are expressed in per cent per day. ($1\%/d = 1.16\times10^{-7}\ s^{-1}$)

Length scale diameter (km)	Season	Divergence		Shear		Vorticity		Strain magnitude	Experiment
		mean	st.dev.	mean	st.dev.	mean	st.dev.	mean	
20	spring	---	0.65	--	0.86	--	1.1	--	AIDJEX 1972
100	spring	--	0.43	--	0.54	--	0.61	--	AIDJEX 1972
200	winter	0.07	1.0	1.6	1.6	-0.52	2.0	2.1	1975 AIDJEX manned array
	summer	-0.03	1.6	3.5	2.2	--	--	--	
800	winter	0.02	0.56	1.0	0.86	--	--	1.3	1975 AIDJEX buoy array
	summer	0.16	1.0	1.6	0.86	--	--	2.2	
800	winter	0.07	0.58	0.77	0.54	--	--	1.1	1962-64 T3, NP-10, Arlis II
	summer	0.06	0.80	1.0	0.68	--	--	1.5	
1000	winter	0.02	0.45	0.95	0.82	-0.78	1.5	1.1	1979 buoys
	summer	-0.11	0.76	1.5	0.95			1.9	

Sources: Hibler, et al., 1974; Colony and Thorndike, 1981; Maykut, 1982.

The distribution of the invariant θ is plotted in figure 20. Note that nearly always $\pi/4 < \theta < 3\pi/4$. In this range, the two principal values of the strain rate tensor have opposite signs. The figure indicates that it is almost always the case that when the ice pack is extending in one direction, it is contracting in the perpendicular direction. Hibler et al., 1974 also comments on this for strain measurements on a 20 kilometer scale.

It is also evident from Table V that the summer values are usually somewhat greater than the winter-spring values. Presumably the ice pack is weaker and offers less resistance to deformation in the summer. (The alternative hypothesis, that the driving forces are larger in the summer, is not true.)

The mean quantities in Table V produce large strains over the course of a year. The year long deformations at the AIDJEX arrays are shown in figure 21. The region experienced a net clockwise rotation of about 35°. The principal deformation involved a stretching of about 90% in the east-west direction and a contraction of about 40% in the north-south direction. The net divergence was not significantly different from zero. The two nested arrays experienced similar deformations.

Deformation estimates at a number of points in the central basin for the years 1979 and 1980 are presented in figure 22. The strain ellipses typically show large shear and small divergence. The only pattern evident in the figure is the similar alignment of the major principal axis of shear for the five points closest to the pole. Perhaps we should not expect to see any patterns in the deformation displayed on this scale. Recall that the spatial correlation function for L-differences of daily velocities has a length scale of only about 400 kilometers. The deformations at points separated by greater distances should evolve more or less independently. Conceivably there may be some underlying spatial pattern to the deformation rate which is small on a daily basis but which accumulates to a large spatially organized strain over the course of a year. The strain ellipses for 1979 and 1980 do not support this idea. On the other hand the long term average vorticity is clockwise throughout the central basin. It amounts to about 40° per year.

5.4.4 Interpretation of deformation measurements

A number of authors have confronted the difficulties of describing the deformation of this discontinuum. Nye (1973) for instance, puts forward a definition of "strain on a length scale L." By first smoothing the velocity field using a kernel of length scale L, he obtains a new velocity field

which is differentiable and for which the usual notions of deformation based on partial derivatives are valid. Papers by Hibler et al., 1974 and Thorndike and Colony, 1977 take a similar point of view by attempting to partition the ice deformation into two parts. The first part is assumed to be associated with the spatial variation of the atmospheric and oceanic forcing fields and with the geometry of the basin, to have a characteristic length of 10^3 km, and to be differentiable. The second part is associated with the irregular, discrete geometry of the ice pack. It has length scales less than 10 km and is characterized by discontinuous variations in velocity. In these papers, the first kind of variation is referred to as the large scale, underlying, continuum, or linear part of the velocity field, while the second is referred to as the small scale, local, perturbation, fluctuating, or non-linear part. Velocity variations of the first type are regarded as signal and those of the second type as noise. This nomenclature reflects the hope that any physical process of interest can be parameterized in terms of the large scale signal, with small scale noise only making it difficult to measure the signal well.

This convention obscures the true nature of the velocity field which is that it has variations on all length scales, with a smooth decrease in amplitude for decreasing length scales. There is no clear division between large and small scale. Furthermore there is no clear reason to associate large scale with signal and small scale with noise. For studies involving the actual opening and closing of leads, the small scale phenomena may indeed be the signal. Further we must be prepared for the possibility that the small scale phenomena cannot be parameterized in terms of the large scale motion.

Perhaps a better conceptual model of the spatial structure of the ice velocity is a system which accepts a smooth input and produces a discontinuous output. (A simple example of such a system is the greatest integer function:

$[x]$ = greatest integer less than or equal to x .)

—— The shift in emphasis from the earlier model is this. The earlier model viewed the velocity as the sum of separate contributions, one smooth, one discontinuous. The alternative views the velocity as a discontinuous response to a smooth input. This point of view may lead more naturally to phenomenological descriptions of the properties of the ice pack, through a comparison of the input and output fields. To my knowledge this has not been attempted because data with adequate spatial resolution of the velocity field are still too scarce. Such a study would not explain why the velocity field had certain properties. That explanation must be based on rather deeper understanding of the geometry of the ice pack and the forces which act between floes than we have at present. Still it would be useful to compare some of the properties of the ice velocity with properties of the external driving forces, i.e., the geostrophic wind and the ocean currents.

5.4.5 . Errors in estimating the large scale deformation

The large scale deformation estimates of the previous section are subject to sampling variations since they depend on the particular array of measurements points. There have been several attempts to quantify the sampling errors. Hibler et al., 1974; Nye, 1975; and Thorndike and Colony, 1977 examined the departures of the measured velocities from the best fit linear relationships. These departures, called residuals, homogeneity variations, or nonlinear fluctuations, represent the variability of the actual velocity field on scales smaller than the diameter of the region of interest.

From observations over a 20 km scale taken during the spring of 1972, Hibler et al. found root-mean-square velocity residuals of 0.06 cm sec^{-1}, compared to typical linear changes in velocity $\left(L\overline{\partial u/\partial x}\right)$ over 20 km of 0.14 cm sec^{-1}. Thorndike and Colony used observations from a 100 km scale taken during the spring of 1975 and found rms residuals of 0.4 cm sec^{-1} and typical linear changes over 100 km of 1.1 cm sec^{-1}. Their summer values were somewhat larger: 1.1 cm sec^{-1} and 1.8 cm sec^{-1} for the nonlinear and linear contributions. These residuals can be regarded as errors with respect to the large scale average derivatives for the region. When the number of observations is small, the estimated large scale deformations are strongly contaminated by these errors.

Using what we know about the correlation functions for velocity, we can profitably address the sampling question from a different angle. Taking the line integral definition for the large scale velocity derivatives, we ask: how many points around the perimeter of the region must be sampled to resolve the integral to some desired accuracy? Intuition suggests that the measurements should be spaced closely enough to permit good interpolation but not so closely as to be highly redundant. A correlation between velocities at neighboring measurement points of 0.5 might be a fair guess; this would indicate a spacing of about 400 km.

To get a better answer, we estimate the line integral in equation 6 around a circular region of radius r as

$$D_M = \frac{1}{\pi r^2} \sum_{i=1}^{M} u_i \cos\theta_i \frac{2\pi r}{M} \quad , \quad \theta_i = (i-1)\frac{2\pi}{M} \quad , \; i = 1, \cdots, M .$$

Then as the number of measurements M increases, D_M approaches $\overline{\partial u/\partial x}$. Since D_M is a linear combination of velocity components, we can find its

variance in terms of the variances and covariances of the velocity components at all M points, and these can be evaluated in terms of the correlation functions $B_{\parallel}$ and $B_{\perp}$. Let $\underset{\sim}{U}$ be the vector involving all 2M velocity components, $\underset{\sim}{A}$ be the vector of coefficients, and R be $E\underset{\sim}{U}\underset{\sim}{U}^T$. Then $D_M = \underset{\sim}{A}^T \underset{\sim}{U}$ and $E D_M^2 = \underset{\sim}{A}^T R \underset{\sim}{A}$. This calculation has been done for $M=60$ which was large enough to resolve $\overline{\partial u/\partial x}$. The dependence of $(E D_{60}^2)^{1/2}$ on the radius r is shown in figure 23a.

This curve depends on $B_{\parallel}$ and $B_{\perp}$ which for this purpose were taken to be $(1-r/a)\exp-(r/b)^2$ with a = 2000 km, b = 1300 km for $B_{\parallel}$ and a = 900 km, b = 1000 km for $B_{\perp}$. These functions incorporate the features of the observed correlations in figure 16. The leading factor $(1-r/a)$ makes the assumed functions vary linearly near $r=0$. The behavior of the correlation functions near $r=0$ is related to the variance of increments by

$$\mathrm{Var}\left(u(r+\Delta) - u(r)\right) = 2q^2\left(1 - B_{\parallel}(\Delta)\right)$$

$$\approx 2q^2\Delta/a \qquad \text{for small } \Delta$$

which is a rough approximation to figure 19 where the variance of increments is seen to be proportional to $\Delta^{1.3}$. The results in figure 23 are quite sensitive to the behavior of the correlation functions. They should not be taken too seriously until more is known about $B_{\parallel}$ and $B_{\perp}$ near $\Delta=0$.

With some caution then we interpret figure 23a as follows. Typical values for the large scale average derivatives are 1% per day decreasing somewhat with the size of the region over which the average is taken. The derivatives $\overline{\partial u/\partial y}$ and $\overline{\partial v/\partial x}$ are generally larger than $\overline{\partial u/\partial x}$ and $\overline{\partial v/\partial y}$ as a consequence of $B_{\perp}$ falling off more rapidly than $B_{\parallel}$.

The variance of the error in estimating $\overline{\partial u/\partial x}$ using only M points, $E(D_M - D_{60})^2$ can be calculated in the same manner simply by redefining the coefficients in the vector $\underset{\sim}{A}$. These results are presented as a fraction of the signal variance $E(D_{60}^2)$ in figure 23b. When M is 3, as was the case for AIDJEX 1972, the 1975-76 manned AIDJEX array, and LOREX 79, the ratio of estimation error variance to signal variance was about 0.7.

With six measurements around the circumference of the region, the average derivations are resolved fairly well, and only small improvement is realized by adding more measurements. The results are insensitive to

the size of the region. The broad curves in figure 23b contain results for discs ranging in radius from 100 to 500 km.

In this section we have asked how many measurement stations are needed to provide good estimates of the large scale average velocity derivatives. This is a different issue than how densely must one sample in space to resolve the spatial patterns in the deformation. Observations from a 500 km grid can be expected to give fairly good estimates of the average deformation, but will not resolve the spatial pattern very well.

5.4.6 The relationship between measured large scale deformation and total opening and closing

Suppose a region of interest is intersected by a number of cracks, each of which is opening or closing at some rate. If the rates were known, the total rates of opening and closing for the region could be found. In practice we are not able to measure the motion at each crack, but only the motion of a few points in the region. How are we to use these few measurements to estimate the opening and closing?

In an analogous situation in one dimension, we have k cracks each with opening or closing rate u_i $i=1,\cdots,k$. We can imagine the velocity u to be a random function of x having random discontinuities at random points and being constant between the points. Suppose we have measured only the motion at the end points of the region, an interval of length L . Then

$$\begin{aligned} A &= \text{total opening} = \sum_{i=1}^{k} \max(u_i, 0) \quad , \\ C &= \text{total closing} = \sum_{i=1}^{k} \min(u_i, 0) \quad , \\ U &= \text{net opening or closing} = A + C = \sum_{i=1}^{k} u_i \quad , \end{aligned} \tag{7}$$

and the problem is to estimate A and C given U . At first sight the situation seems hopeless. U clearly contains information about the net opening or closing but not about the total opening and closing. However, knowledge about the random variables $k, u_1, u_2, \cdots, u_k$ can be used to make probabalistic statements about the opening and closing. Suppose for instance k has the Poisson distribution with parameter λ . This means that λL is the average number of cracks in an interval of length L . Then the probability of finding k cracks in a random interval of length L is

$$p(k;\lambda,L) = (\lambda L)^k e^{-\lambda L} / k! \quad .$$

If $\lambda L = 0.1$, for instance, the probability of getting $k = 0$ is 0.9051, $\text{prob}(k=1) = 0.0905$, and $\text{prob}(k>1) = 0.0045$. Therefore, with high probability, there is either no crack or just one in the interval and the observed value of the velocity difference u would itself indicate the total opening and total closing. Of course for larger λL it becomes more likely that several cracks intersect the test interval, in which case the observed u cannot separate the opening from the closing.

A similar approach for the two dimensional problem is to imagine the ice pack to be crisscrossed by a family of random cracks, defined by the random straight lines

$$x \cos\theta_i + y \sin\theta_i = r_i$$

where each θ_i has the uniform distribution on $(0, 2\pi)$ and the normal distances r_i from the origin to each line form a sequence of Poisson points. Imagine that associated with each crack is a velocity discontinuity $\underline{u}_i$ having the Gaussian distribution. This describes a random vector field having structure akin to the velocity field of sea ice. The observations of Hall and Rothrock can be used to estimate the parameters in the Poisson and Gaussian distributions. These random fields have the following properties. They consist of discrete rigid floes. The floes have a distribution of sizes determined by the Poisson field of lines. The Poisson lines are isotropic and homogeneous. The velocity difference between any two points is the vector sum of the velocity discontinuities encountered getting from one point to the other.

At each crack the opening or closing is determined by the projection of the velocity difference vector onto the normal to the crack.

$$\text{opening} = \max\left(0,\ u_i \cos\theta_i + v_i \sin\theta_i\right)$$

$$\text{closing} = \min\left(0,\ u_i \cos\theta_i + v_i \sin\theta_i\right)$$

Thus it is a simple matter to evaluate the total opening and closing for any realization of the random field.

Of course one can also imagine measuring the velocity at a few points and constructing the L-strain rate invariants from the observed velocities. In this way one can test for a relationship between the L-strain rate invariants calculated from a few sampled velocities and the total opening and total closing found by tallying up the activity at every crack.

In an attempt to carry out this program, parameter values were taken to be $\lambda = 0.08\,\text{km}^{-1}$, $\mu = 0$, $\sigma^2 = 1$ (arbitrary units)^2. An $L = 100$ km triangle was used to simulate the sampling procedure used during AIDJEX. A large number of random fields were generated.

Each realization of the random field is defined by the sequences of random numbers $k, \theta_i, u_i, v_i, r_i$ for $i = 1, \cdots, k$. Here the θ_i are drawn independently from the uniform distribution on $(0, 2\pi)$. The values for r_i form a Poisson process with parameter λ. This is achieved by drawing the increments $\Delta = r_{i+1} - r_i$ independently from the exponential distribution with density $\lambda e^{-\lambda\Delta}$. The process is terminated as soon as r_k exceeds 100 kilometers since none of the subsequent lines would intersect the 100 kilometer region. Finally the u_i and v_i were drawn independently from the normal distribution with zero mean and unit variance.

For each field the velocity was measured at the three specified points and the L-strain rate invariants $|E|$ and θ were evaluated. Also for each field the total opening and closing were evaluated using eq. 7. These were normalized by $|E|$ and displayed versus θ in figure 24. For each realization of this random field two points are plotted, $(\theta, A/|E|)$ and $(\theta, C/|E|)$. From the plot it is clear that there are not unique values of $A/|E|$ and $C/|E|$ corresponding to a given θ. Instead there is a distribution of values for $A/|E|$ (and for $C/|E|$), and this distribution changes with θ. The distributions, sketched in figure 25, are broad in the sense that probable departures from the mean are at least as large as the mean.

The interpretation of this exercise is that the total opening and closing are only weakly determined by the L-strain rate invariants based on three measurements 100 kilometers apart. Had the relationship been a strong one the distributions in figure 25 would have been narrower, or to say it differently, the points in figure 24 would have clustered more closely around curves like those in figure 18. It may still be useful to imagine these smooth curves but only with the recognition that the actual opening and closing scatter widely about the imagined curve:

$$A/E = \alpha_0(\theta) + \text{random error}$$

$$C/|E| = \alpha_\pi(\theta) + \text{random error}$$

where the random terms and the θ-dependent terms make roughly equal contributions to the total opening and closing.

Some of the scatter in these figures arises from having used only three points to estimate the deformation invariants. With more than three points, the errors in the invariants could be reduced, somewhat as shown in figure 23. But even if the invariants are determined without error, scatter will remain in figures 24 and 25. This is because many different fields of motion with different total opening and closing could have exactly the same large scale average deformation.

The total opening and closing are an essential part of the theory of the ice thickness distribution. The above results suggest that it may not be satisfactory to represent the total opening and closing as functions of the large scale average velocity derivatives. When many velocity measurements are available in a region, it is possible to estimate more of the spatial structure than simply the average velocity derivative. An attempt to estimate the variability of velocity within the region may help to reduce the scatter which is anticipated on the basis of figure 24. Or perhaps it will be enough to assume that the variability is constant in time. One might then drive the thickness distribution calculations with opening and closing time series which have the right statistical properties even if they may have large errors on a day to day basis. The statistical properties can be inferred from figure 24. Of course this figure is the consequence of a particular conceptual model motivated by a limited data set--the SEASAT SAR data from early October 1978. More data need to be collected and studied before these ideas can be extended to other times and places with confidence.

5.4.7 The relationship between kinematics and stress

Kinematic data can be used for studying the relationship between stress and strain for sea ice. Suppose for instance that the state of stress tensor σ suitably averaged over some region, is related to kinematic quantities ε and the ice geometry s by some expression of the form

$$\sigma = F(\varepsilon, s) \, .$$

Although σ cannot be measured directly, its divergence $\nabla \cdot \sigma$ can be inferred indirectly from the observed momentum balance when all the other terms in that balance are known. If a particular function F is hypothesized, it can be tested by evaluating both sides of the equation $\nabla \cdot \sigma = \nabla \cdot F(\varepsilon, s)$, the left hand side as a residual from the momentum balance and the right hand side in terms of observed kinematic and ice geometry quantities. This

was one of the objectives of AIDJEX (Maykut et al., 1972). In practice the test is difficult to make since neither $\nabla \cdot \sigma$ nor $\nabla \cdot F$ can be determened very accurately from observations. See Rothrock et al., 1980.

Under special circumstances, meaningful tests may be possible, however. When the ice deformation is strongly divergent, ice floes tend to move apart. With no floe-to-floe contacts there can be no $\nabla \cdot \sigma$ forces. The left hand side should differ from zero only by measurement error. These errors are probably small enough to permit a useful test.

Another special situation of interest is when the ice is being forced up against the coasts by the wind. As the ice moves toward the coast it converges, becomes stronger, and eventually becomes strong enough to resist further deformation. If the on shore winds persist, a zone of motionless ice can widen to several hundred kilometers (Pritchard, 1977). In this situation, intuition suggests that the $\nabla \cdot \sigma$ vector should point off shore and should increase in time until it balances the on shore wind stress. With simultaneous ice trajectories at 100, 200, 300 and 400 km from the coast, it should be possible to observe the amount of convergence required to produce the required resistance to the wind.

At greater distances from the coasts, there is evidence that the ice stresses embodied in $\nabla \cdot \sigma$ are usually small. Little success is anticipated in trying to observe them. Any stress-strain law which provides adequate resistance to deformation near the shore is probably adequate for full basin dynamic modeling. The observations may never be adequate to discriminate very selectively between candidate stress-strain laws.

5.5 Discussion

I have tried in this paper to bring together some of what is known about the motion of sea ice. The emphasis has been on the departures of the true motion from the long term mean circulation. This is a comparitively new topic, the investigation of which has only recently been made possible, mainly by the developments of satellite positioning techniques. Perhaps because of its newness, the field lacks a clear agenda of questions to be answered. Instead we are still trying to characterize the motion, to determine the magnitude of the motion on different scales and to identify motions which have some intrinsic interest or are related to other phenomena of interest.

The time and space correlations have been used extensively here for several reasons. First they give a compact description of the motion. In

principle, the correlation function involves one time and two space variables, but in practice a great deal of information can be extracted from three functions, each of a single variable: $R(\tau)$, $\beta_{\parallel}(r)$ and $\beta_{\perp}(r)$. Second, these three functions are accessible to observation. Third, properties of many kinematic quantities can be deduced from these functions, as illustrated in the text. Fourth, these functions form the rigorous basis for answering questions related to interpolation, prediction, and experiment design.

Many of the results presented here are based on sample autocorrelation functions deduced from limited data. The data available for estimating correlations at small space lags (less than 100 km) are meagre indeed. More work along the lines of Hall and Rothrock would help to resolve this part of the correlation function. The behavior of the correlation functions $\beta_{\parallel}(r)$ and $\beta_{\perp}(r)$ in the limit of small r is an important property of the motion related to the granular nature of the ice pack.

As mentioned in the text, care must be exercised in choosing correlation functions or contradictions (negative variances) can occur. In fact this has happened in some of the calculations done using the correlations tabulated in Table VI with linear interpolation to intermediate distances. This means that the piecewise linear function defined in the table is not positive definite. A useful objective would be to find a positive definite analytical form which approximates the observed correlations including the behavior as r approaches zero.

The Poisson-Gauss model, presented as a way to study the relationships between the local opening and closing and the large scale deformation, has suggested that the relationship may be weak. Observations against which to test this suggestion are sorely needed.

Table VI. Spatial correlation functions for sea ice velocity.

Distance (km)	$\beta_{\parallel}$	$\beta_{\perp}$
0	1.00	1.00
100	.98	.95
200	.91	.84
400	.68	.51
800	.37	.06
1200	.19	-.09
1600	.10	-.10
2000	.01	-.06
2400	.00	.00

Acknowledgment. This work was supported by the National Oceanic and Atmospheric Administration Grant NA80-AA-D-00015, which was funded in part by the Global Atmospheric Research Program and the Office of Climate Dynamics, Division of Atmospheric Sciences and the Meteorology Program, Division of Polar Programs, of the National Science Foundation, and the Office of Naval Research, Arctic Programs. The paper also reports on work supported by the Office of Naval Research Contract N00014-79-C-0418.

Some of the ideas discussed here grew out of informal discussions with Drew Rothrock and with Roger Colony. I take this opportunity to acknowledge their contributions and to thank them.

References

AIDJEX Staff, 1972. Station positions, azimuths, weather, 1972 AIDJEX Pilot Study, Preliminary data, AIDJEX Bulletin No. 14, 63-208.

Colony, R. and A. S. Thorndike, 1980. The horizontal coherency of the motion of summer arctic sea ice. J. of Phys. Oceanography, 10(8), 1281-1289.

Colony, R. and A. S. Thorndike, 1981. Sea ice strains during 1979. Proceedings of the 6th International Conference on Port and Ocean Engineering Under Arctic Conditions, Quebec City, Quebec, 27-31 July 1981, 619-628.

Craig, L. W., 1972. High frequency accelerations of arctic pack ice. Master's thesis, Department of Civil Engineering, University of Washington, Seattle.

Doronin, Yu. P. and D. E. Kheisin, 1975. Morskoi Led. (English translation, Sea ice, 1977. Amerind Publishing Co. Pvt. Ltd., New Delhi.) 323 pp.

Hall, R. T., 1980. AIDJEX modeling group studies involving remote sensing data. Sea Ice Processes and Models, R. S. Pritchard, Editor; University of Washington Press, Seattle.

Hall, R. T. and D. A. Rothrock, 1981. Sea ice displacement from SEASAT synthetic aperture radar. J. of Geophys. Res., 86(C11), 11078-82.

Hastings, A. D. Jr., 1971. Surface climate of the Arctic Basin. Report ETL-TR-71-5, Earth Sciences Division, Geographic Sciences Laboratory, U.S. Army Engineer Topographic Labs, Fort Belvoir, VA.

Hibler, W. D. III, W. F. Weeks, A. Kovacs, and S. F. Ackley, 1974. Differential sea-ice drift. I. Spatial and temporal variations in sea ice deformation. J. of Glaciology, 13(69), 437-455.

Hunkins, K., 1967. Inertial oscillations of Fletcher's Ice Island (T-3). J. of Geophys. Res., 72(4), 1165-73.

Hunkins, K. and J. Hall, 1971. The navigation of Fletcher's Ice Island (T-3). AIDJEX Bulletin No. 7, 47-58.

Hunkins, K. T. Manley, and W. Tiemann, 1979. Observations of position, ocean depth, ice rotation, magnetic declination and gravity taken at the Fram I drifting ice station. CU-1-79 Technical Report No. 1, Office of Naval Research, Department of the Navy, 60 pp.

Kolmogoroff, A., 1941. The local structure of turbulence in incompressible viscous fluid for very large Reynolds numbers. Comptes Rendus (Doklady) de l'Academie des Sciences de l'URSS, 30(4), 301-305.

Kowalik, Z. and N. Untersteiner, 1978. A numerical study of the M_2 tide in the Arctic Ocean. Deutsche Hydrographische Zeitschrift, Vol. 31, 216-229.

Manley, T., 1981. Eddies of the western Arctic Ocean: their characteristics and importance to the energy, heat and salt balance. Doctoral dissertation, Columbia University, 212 pp.

References, continued

Martin, P., C. R. Gillespie, A. S. Thorndike, D. Wells, 1978. Position measurements of AIDJEX manned camps using the Navy Navigation Satellite System. AIDJEX Bulletin No. 40, 83-102.

Maykut, G. A., 1982. Large scale heat exchange and ice production in the central arctic. To appear in J. of Geophys. Res.

Maykut, G. A., A. S. Thorndike, and N. Untersteiner, 1972. AIDJEX scientific plan. AIDJEX Bulletin No. 15, 67 pp.

McPhee, M. G., 1978. A simulation of inertial oscillations in drifting pack ice. Dynamics of Atmospheres and Oceans, 2, 107-122.

Nye, J. F., 1973. The meaning of two-dimensional strain-rate in a floating ice cover. AIDJEX Bulletin No. 21, 9-17.

Nye, J. F., 1975. The use of ERTS photographs to measure the movement and deformation of sea ice. J. of Glaciology, 73(15), 429-436.

Nye, J. F., 1975. A test of the ice thickness distribution equations by measurements of ERTS pictures. AIDJEX Bulletin No. 28, 141-150.

Nye, J. F., 1976. A coordinate system for two dimensional stress and strain rate and its application to the deformation of sea ice. AIDJEX Bulletin No. 33, 131-143.

Popelar, J., J. Kouba, and D. Wells, 1981. LOREX Satellite Positioning, Draft report, Earth Physics Branch, Department of Energy, Mines and Resources, Ottawa, Ontario, Canada.

Pritchard, R. S., 1977. An estimate of the strength of arctic pack ice. AIDJEX Bulletin No. 34, 94-113.

Rothrock, D. A., 1979. Modeling sea ice features and processes. J. of Glaciology, 24(90), 359-375.

Rothrock, D. A., R. Colony, and A. S. Thorndike, 1980. Testing pack ice constitutive laws with stress divergence measurements. Sea Ice Processes and Models, R. S. Pritchard, Editor; University of Washington Press, 102-112.

Rothrock, D. A. and R. T. Hall, 1975. Testing the redistribution of sea ice thickness from ERTS photographs. AIDJEX Bulletin No. 29, 1-20.

Sverdrup, H. U., 1926. Dynamics of tides on the north Siberian shelf, results from the Maud expedition. Geofysiske Publikajoner IV(5), 75 pp.

Tabata, T., T. Kawamura, and M. Aota, 1980. Divergence and rotation of an ice field off Okhotsk Sea Coast of Hokkaido. Sea Ice Processes and Models, R. S. Pritchard, Editor; University of Washington Press, 273-282.

References, continued

Thorndike, A. S., 1973. An integrated system for measuring sea ice motions. In Ocean 73, IEEE International Conference on Engineering in the Ocean Environment, IEEE Publ. No. 73 CHO 774-0, 490-499.

Thorndike, A. S. and J. Y. Cheung, 1977. AIDJEX measurements of sea ice motion 11 April 1975 to May 1976. AIDJEX Bulletin No. 35, 1-149.

Thorndike, A. S. and J. Y. Cheung, 1977. Measurements of sea ice motion 14 May 1976 to 30 November 1976, October 1975 to December 1976, and January 1977 to September 1977. Unpublished data reports, available from the authors.

Thorndike, A. S. and R. Colony, 1977. Estimating the deformation of sea ice. In Proceedings of the Fourth Annual Conference on Port and Ocean Engineering under Arctic Conditions, Vol. 1, D. B. Muggeridge, ed., 506-517. Memorial University of Newfoundland, St. John's.

Thorndike, A. S. and R. Colony, 1980. Large scale ice motion in the Beaufort Sea during AIDJEX, April 1975 to April 1976. In Sea Ice Processes and Models, R .S. Pritchard, ed., University of Washington Press, 249-260.

Thorndike, A. S. and R. Colony, 1980. Arctic Ocean Buoy Program, data report, 19 January 1979-31 December 1979. University of Washington, 131 pp.

Thorndike, A. S. and R. Colony, 1981. Arctic Ocean Buoy Program, data report. 1 January 1980-31 December 1980. University of Washington, 127 pp.

Thorndike, A. S. and R. Colony, 1982. Sea ice motion in response to geostrophic winds. To appear in J. of Geophys. Res.

Thorndike, A. S., D. A. Rothrock, G. A. Maykut and R. Colony, 1975. The thickness distribution of sea ice. J. of Geophys. Res., 80(33), 4501-4513.

Tucker, W. B., W. F. Weeks, A. Kovacs, A. J. Gow, 1980. Nearshore ice motion at Prudhoe Bay, Alaska. In Sea Ice Processes and Models, R. S. Pritchard, ed., University of Washington Press, 261-272.

Zubov, N. N., 1943. L'dy arktiki (Arctic ice), Glavsev-morput (Northern Sea Route Administration), Moscow. Translation 1963. U.S. Navy Hydrographic Office Translation 217, available as AD-426-972, from NTIS, Springfield, VA.

Fig 1 no legend.

AST

Figure 2. The general circulation of ice in the Arctic Ocean (from Doronin and Kheisin).

Figure 3. Buoy trajectories in 1979. The numbers indicate the months in which each buoy was deployed and failed. Trajectories ending in an arrow continued to operate in 1980. Plotted points correspond to the beginning of each month.

Figure 4. Trajectories for drifting buoys during a) 1980, and b) 1981.

Figure 5. (a) Latitude of ice station Caribou, versus time, 2 Sept-16 Nov 1975. NavSat data, sampling interval, 2.5 days.
(b) Latitude of ice station Big Bear, versus time, 2-5 Sept 1975. NavSat data, sampling interval, 4 hours.
(c) Arbitrary y-coordinate of Big Bear, versus time, 2-3 Sept 1975. Acoustic tracking data, sampling interval 15 minutes.
(d) Arbitrary x-coordinate of Big Bear, versus time, 2 Sept 1975. Acoustic tracking data, sampling interval one minute.
Only in (d) is the measurement error visible (±3 m).

Figure 6. (a) The variance of the increments $x(t+\tau) - x(t)$ and $y(t+\tau) - y(t)$ for ice station Caribou 1975-76. x and y are arbitrary Cartesian coordinates.
(b) As in (a) using precise acoustic tracking at ice station Big Bear, an 8-day period, late summer 1976.

Figure 7. Velocity histograms (from Thorndike and Colony, 1980).

Figure 8. The power spectral density of the velocity of ice station Caribou 1975-76. The units of spectral density are velocity^2/frequency, cm^2 sec^{-1}. The total velocity variance for these data is 145 cm^2 sec^{-2}.

Figure 9. The power spectral densities of the geostrophic wind and the ice velocity, from drifting buoy 1901 during 1979. The units of spectral density are cm^2 sec^{-1}. The variance of the wind is 53 m^2 sec^{-2}. The variance of the ice is 59 cm^2 sec^{-2}.

Figure 10. The power spectral density of the velocity of ice station Big Bear during summer 1975. The variance is 173 cm^2 sec^{-2}. Units of spectral density are m^2 s^{-1}. (Linear frequency scale, from Colony and Thorndike, 1980).

Figure 11. The complex time correlation function for ice station Caribou, 1975-76. The velocity variance is 145 cm^2 sec^{-2}.

Figure 12. The time correlation function for the u and v components of velocity from 28 grid points in the central part of the Arctic Basin, from drifting buoy data collected during 1979. The cross correlation between u and v is negligible. Variance of u = 23 cm^2 sec^{-2}; variance of v = 22 cm^2 sec^{-2}.

Figure 13. (a) The real and imaginary parts of the weight α to be used for interpolating to the mid point of a time interval of duration τ. The ratio of the measurement error to the standard deviation of velocity is σ/φ.
(b) The variance of the interpolation error expressed as a fraction of the variance of the ice velocity. Data from figure 11 were used here. Logarithmic time scale.

Figure 14. (a) The weight α for prediction over time τ.
(b) The prediction error variance versus prediction time. See Figure 13 also.

Figure 15. A schematic representation of the x and y components of velocity at the points $(0,0)$, $(\tau,0)$, $(0,\tau)$. Isotropy implies $E_{ac} = E_{bf}$, $E_{bd} = E_{ae}$, and $E_{ae} = E_{df}$, but does not imply equality between E_{ac} and E_{ae} or E_{bf} and E_{bd}.

Figure 16. Observed correlations between velocity components as functions of distance.

Figure 17. The variance of the interpolation error as a function of the grid spacing, L, and the measurement error, σ^2.

Figure 18. The strain rate invariant θ indicates whether the motion is dominated by divergence, shear, or convergence. The total opening and closing are sometimes treated as functions of θ.

Figure 19. The variance of velocity increments versus interval length, from SeaSat synthetic aperture radar data, 3-5 October 1978, Beaufort Sea.

Figure 20. Histograms of the strain rate invariant θ. Solid line is for drifting buoy data from 1979, grid spacing about 500 km (Colony and Thorndike, 1981). Dots are for AIDJEX manned camp data, spacing 100 km (Nye, 1976). Bin width: 20°.

Figure 21. Strain ellipses for the AIDJEX buoy array, 800 km diameter (a); and for the AIDJEX manned camp array, 200 km diameter (b). The ellipses show the deformation of a circular region on 1 May 1975, to the date indicated. The principal axes of the ellipse are the principal strains. The angle from the horizontal broken line to the major axis is the principal direction. The rigid body rotation is indicated by the arc from □ to *. Data from the Beaufort Sea, roughly a 500 km radius about 74°N, 145°W. (From Thorndike and Colony, 1980.)

Figure 22. Strain ellipses from 1979 (solid line) and 1980 (broken line) drifting buoy data, showing the year long deformation of an initial circle (drawn over Greenland).

Figure 23. (a) The standard deviations of the large scale average velocity derivatives, as a function of radius of the averaging region. ($q^2 = 50\ cm^2\ sec^2$).
(b) The ratio of the variance of the error in estimating average velocity derivatives to the variance in the derivatives themselves, as a function of the number of measurements. The dependence on the radius of the averaging region is indicated by the shaded width of the curves.
These curves are sensitive to the assumed correlation functions, as discussed in the text.

Figure 24. The total opening and closing versus θ. 10^3 realizations of the random field with Poisson parameter $\lambda L = 8$. The velocity discontinuities were drawn independently from the unit normal distribution.

Figure 25. Distributions of the total opening for several ranges of θ. Data taken from figure 24.

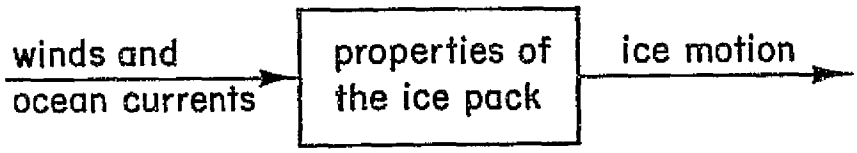

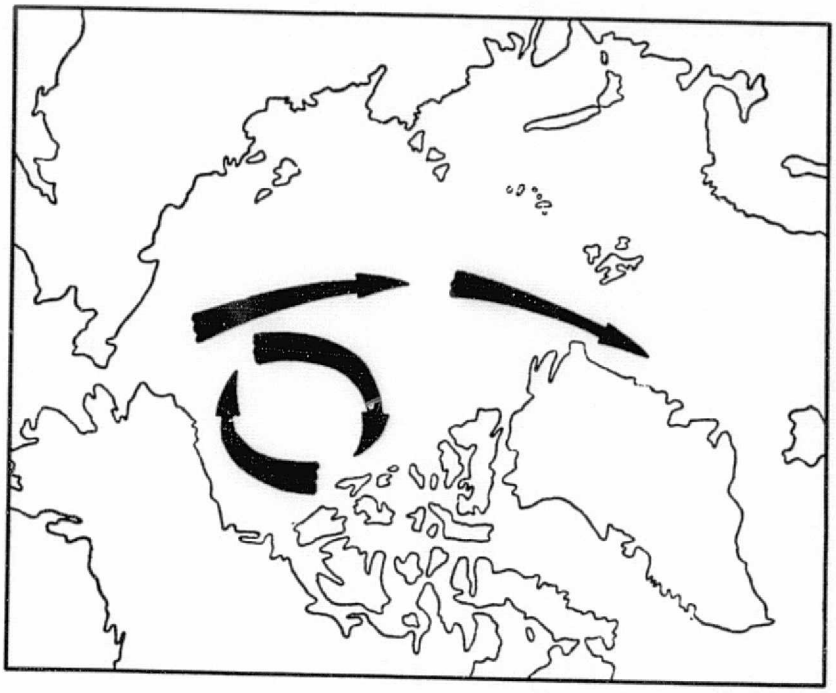

2

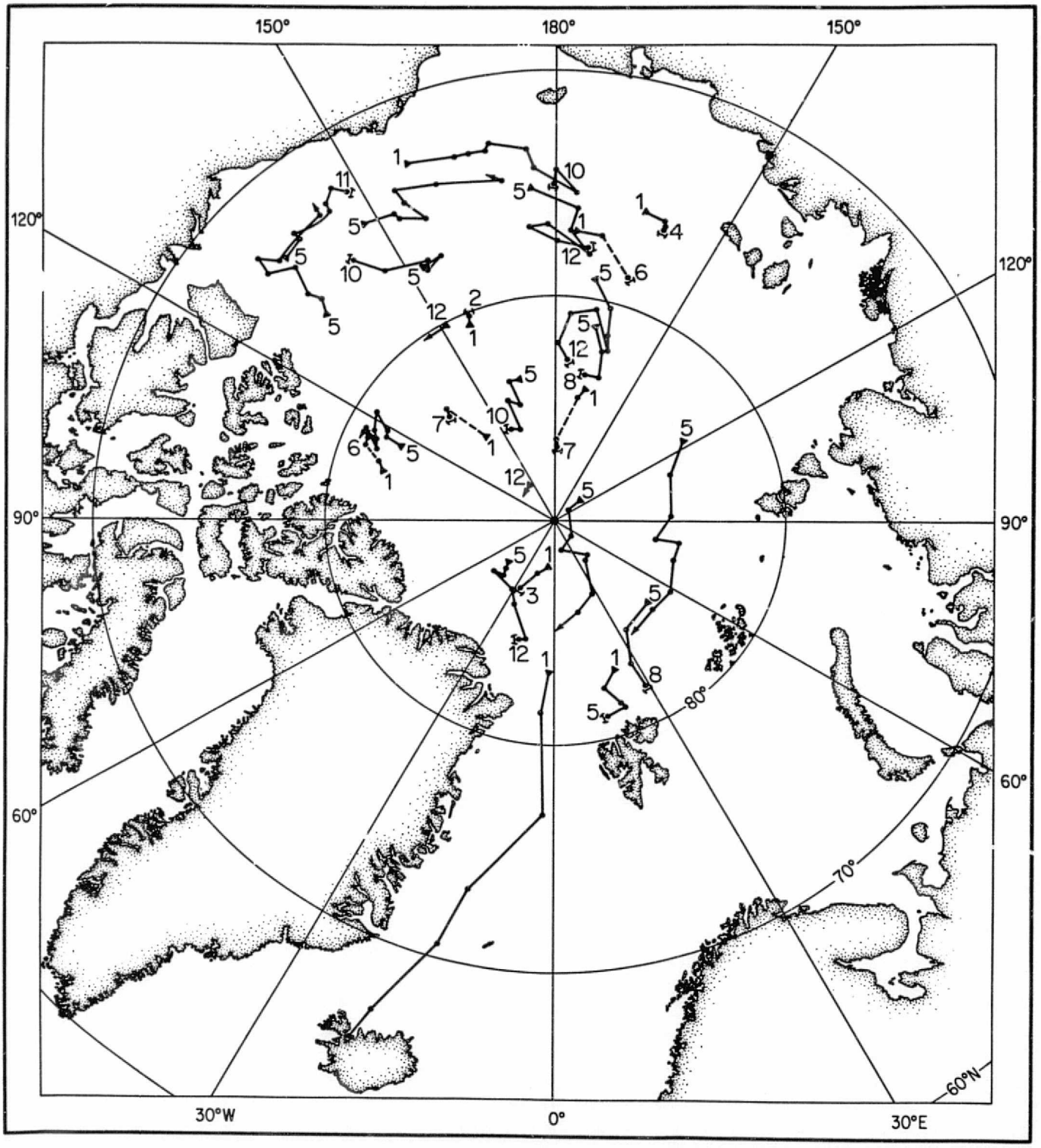

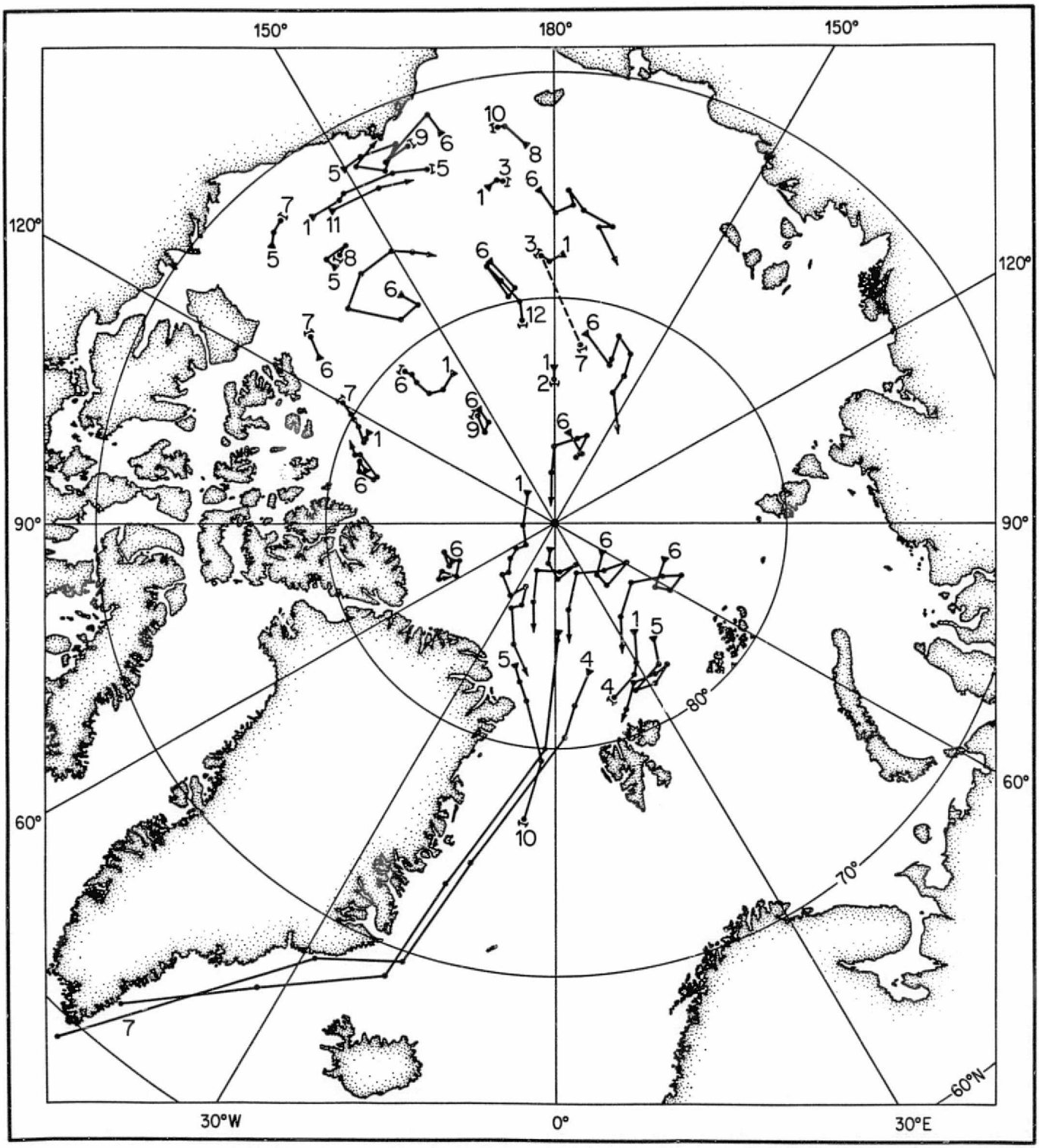

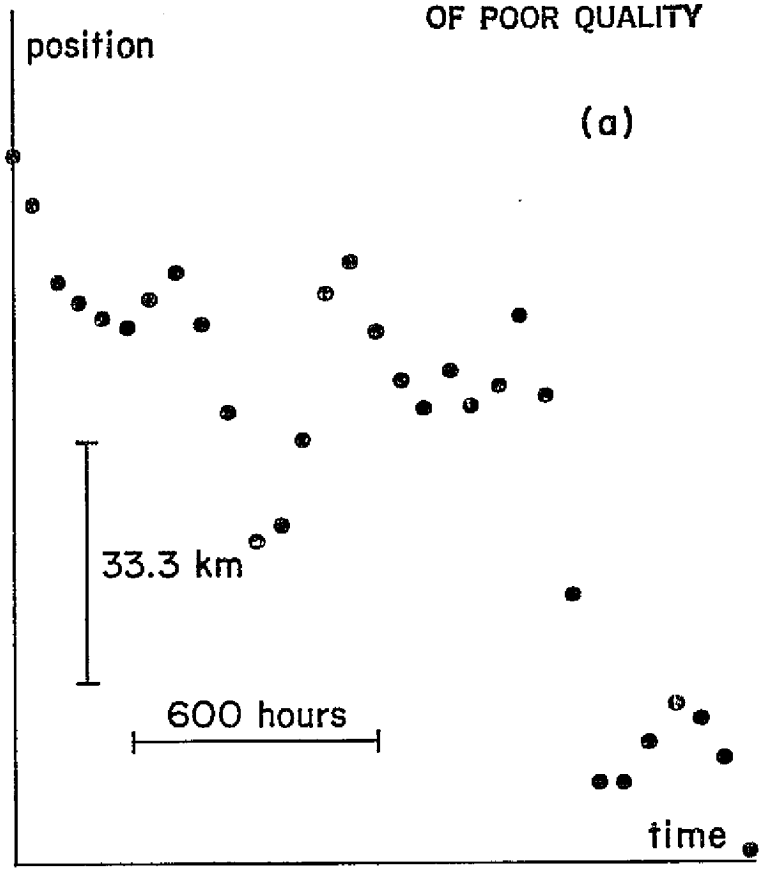

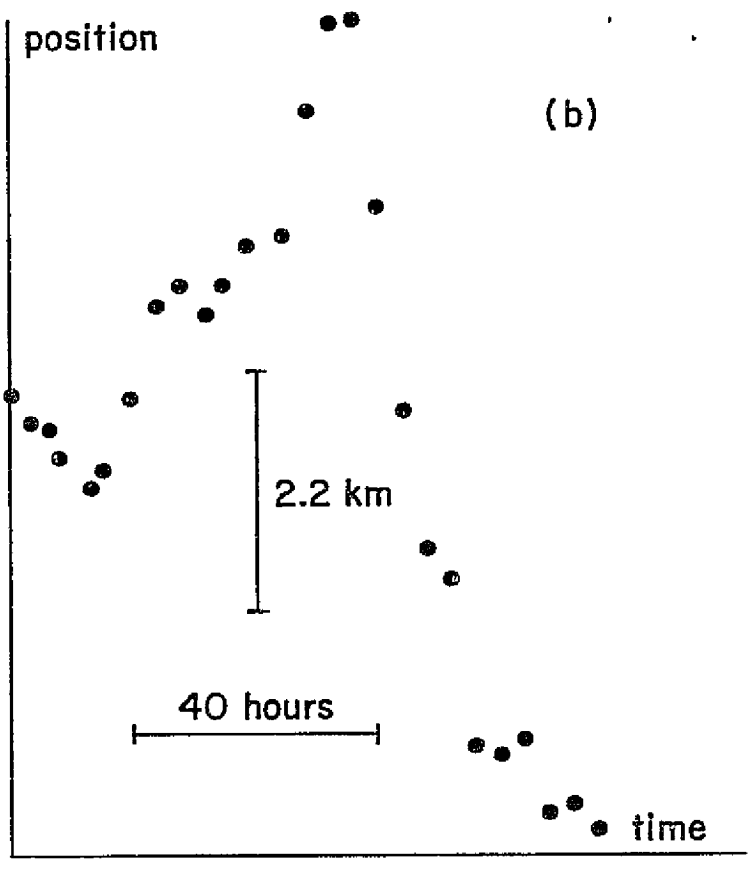

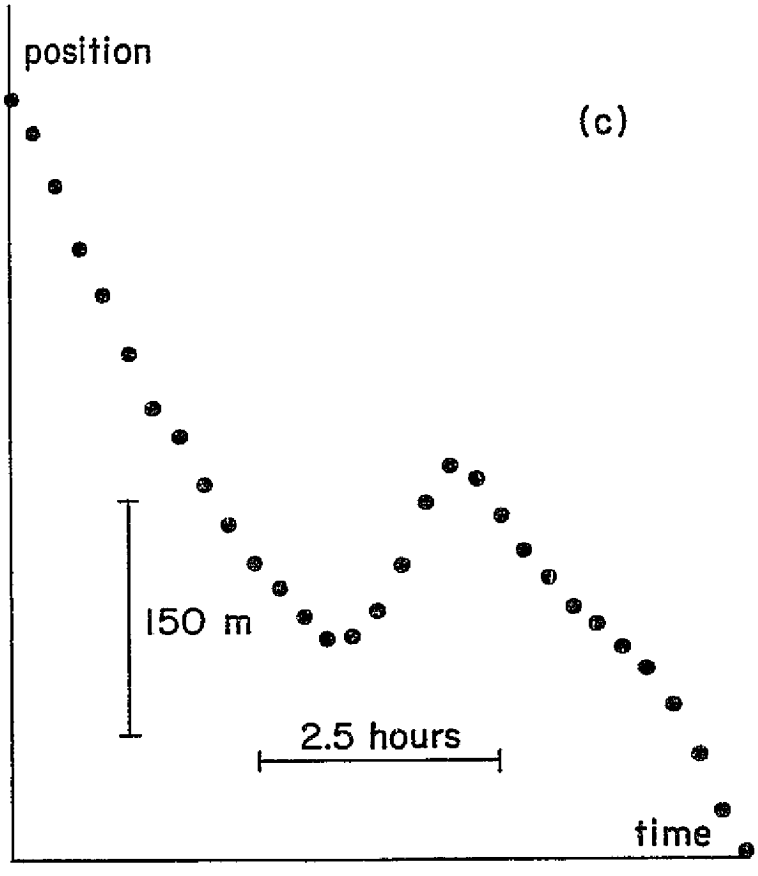

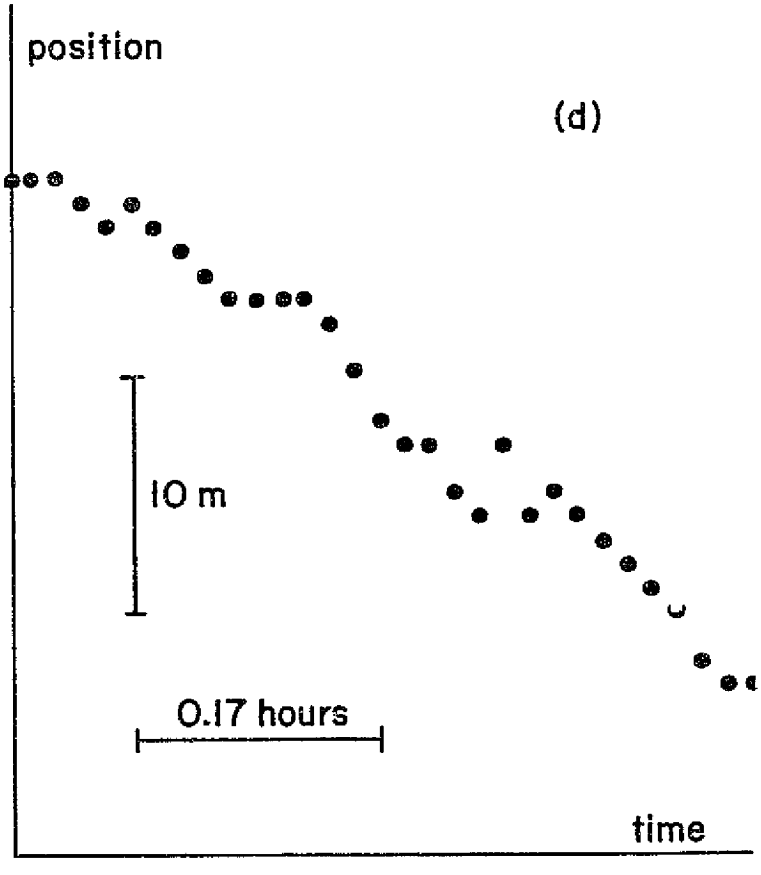

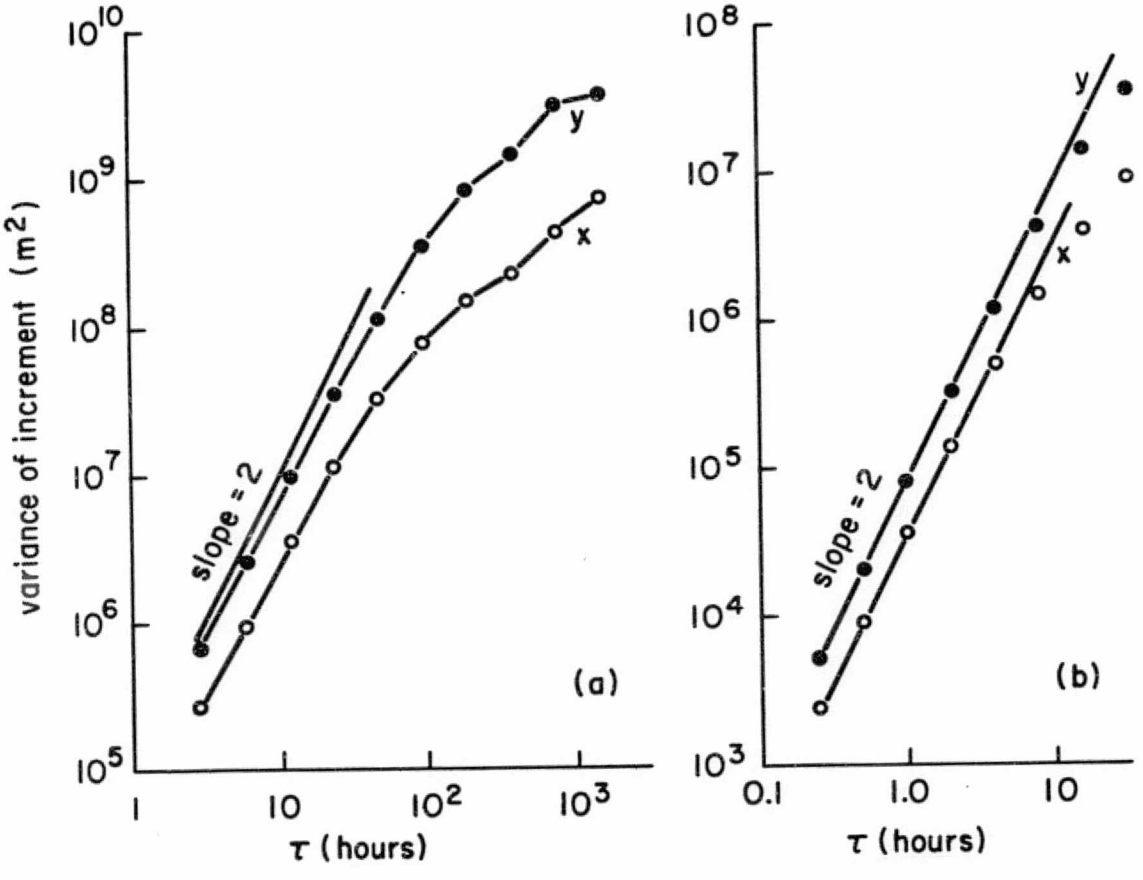

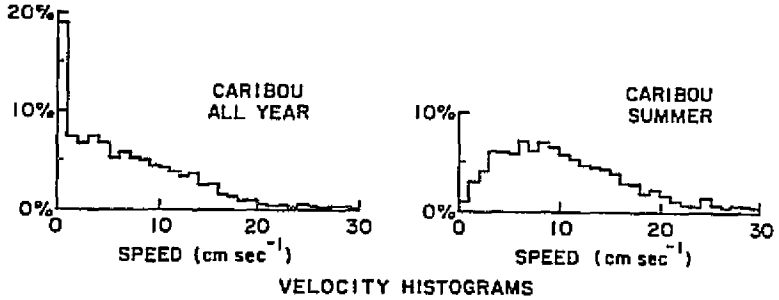

VELOCITY HISTOGRAMS

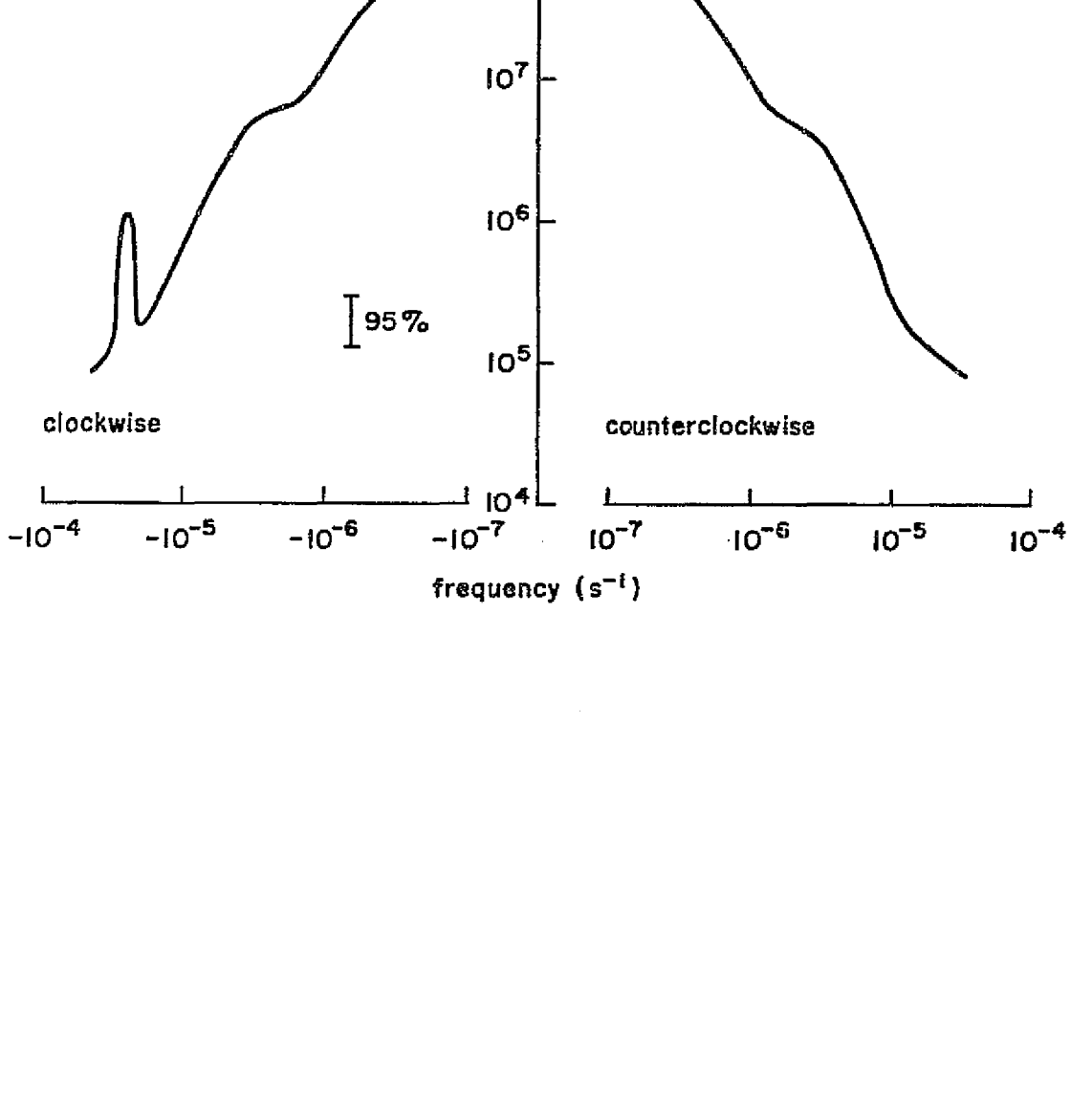

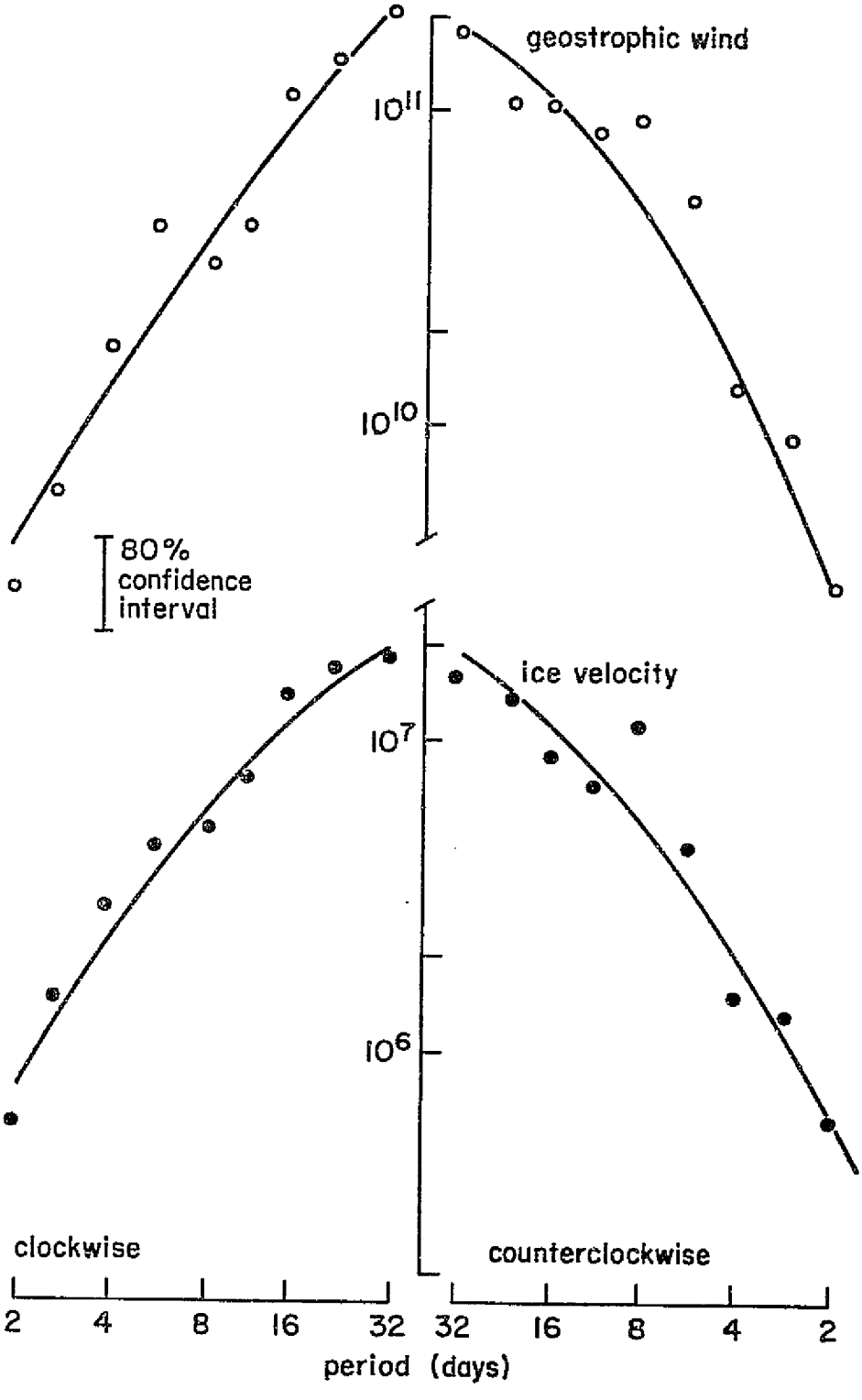

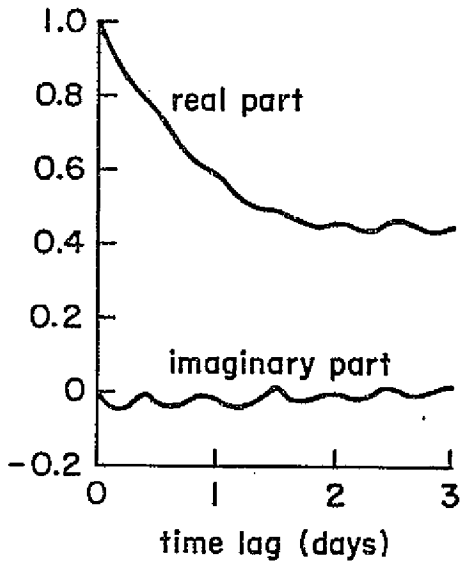

11

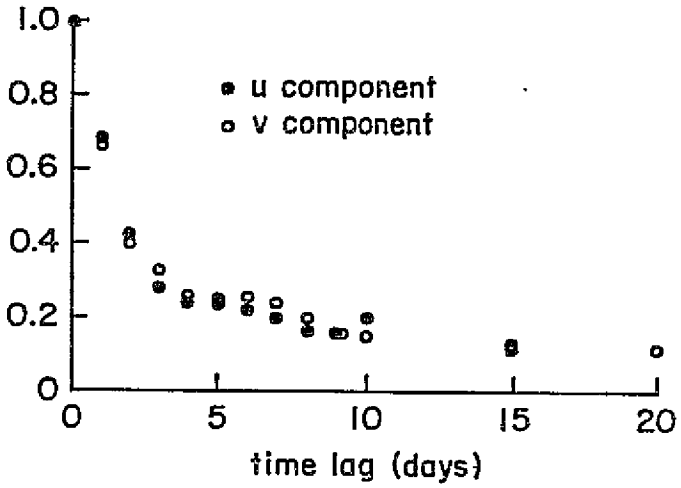

12

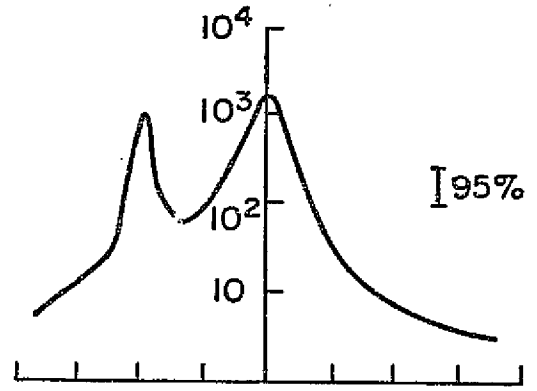

10

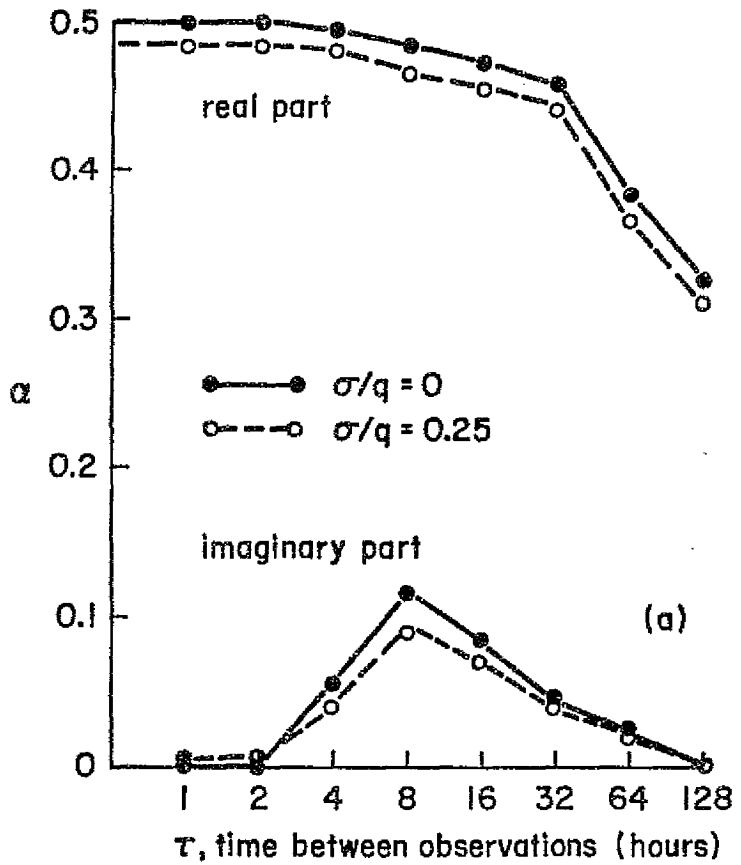

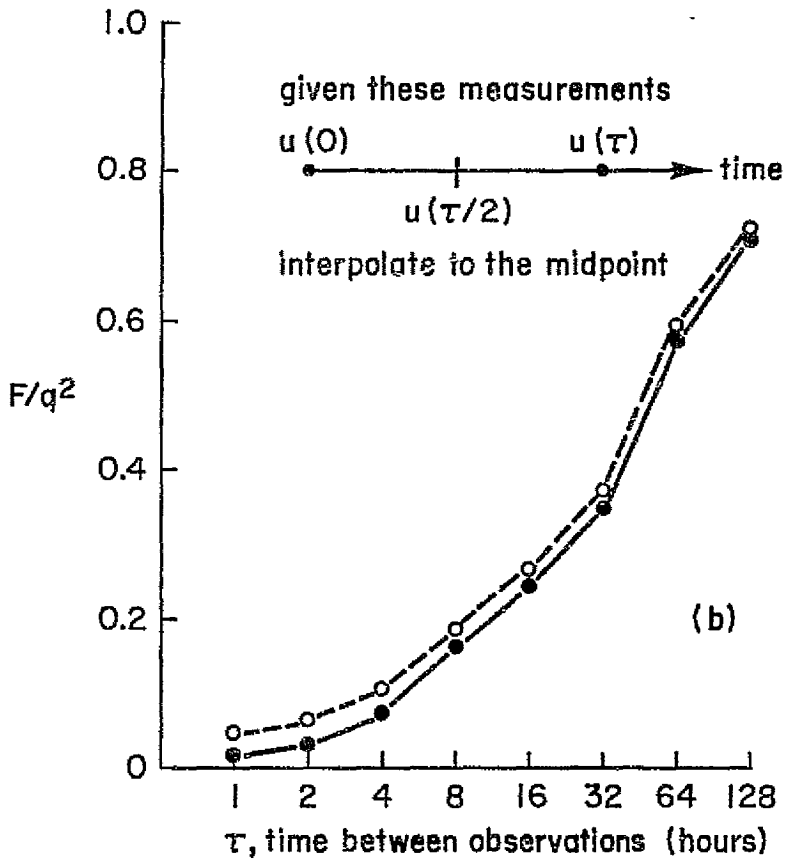

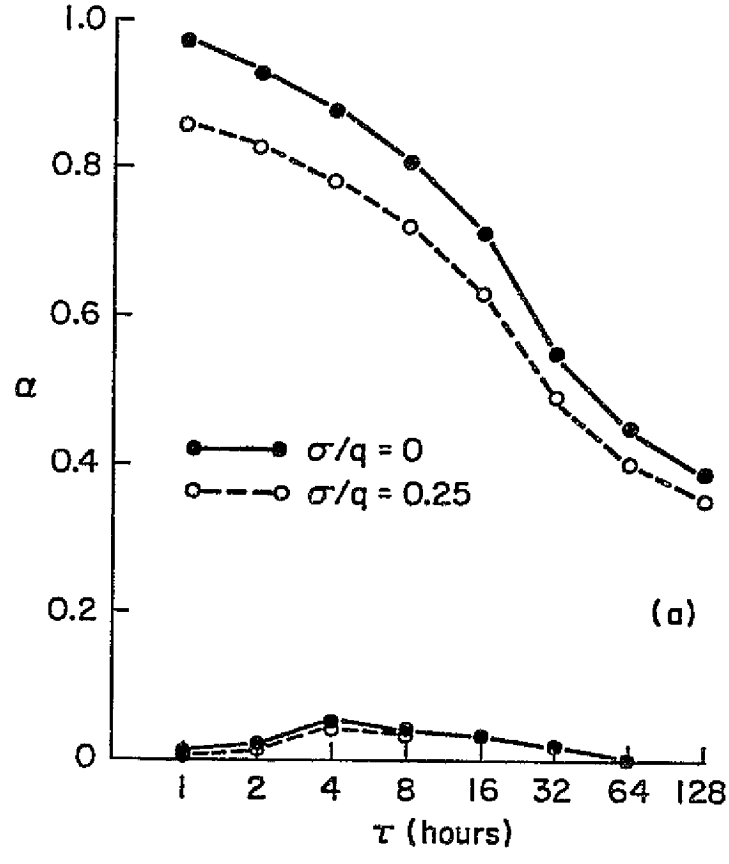

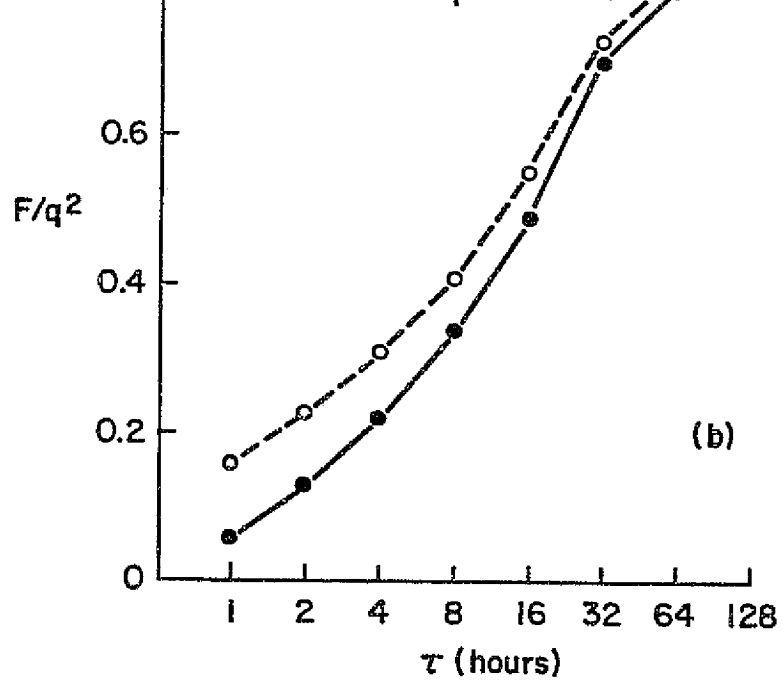

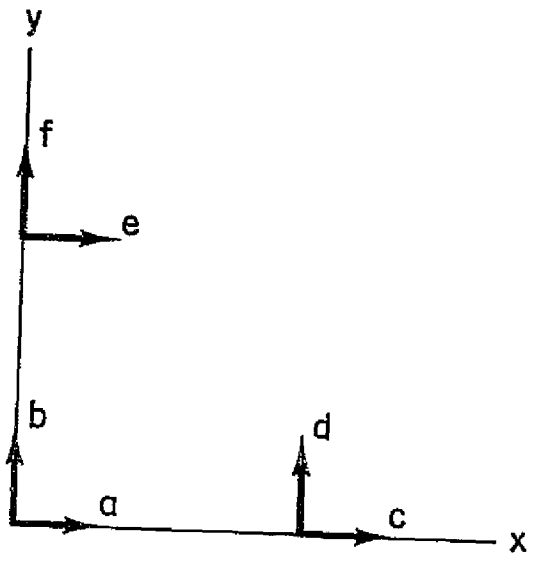

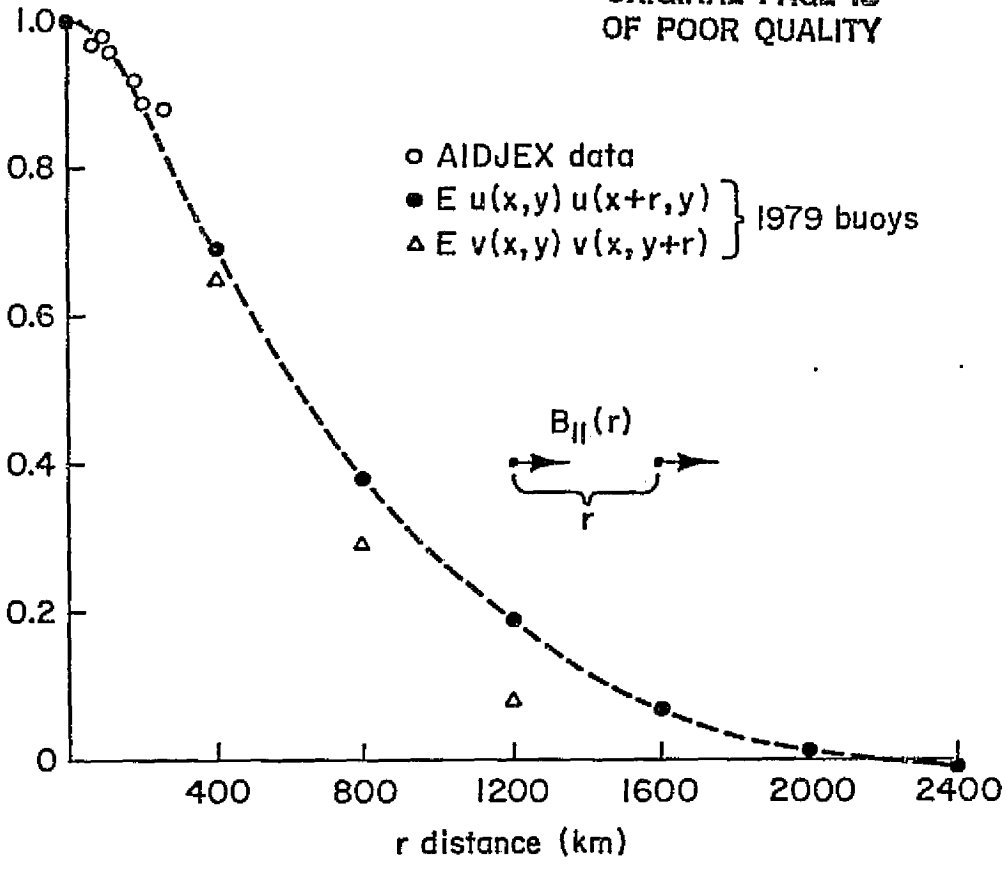

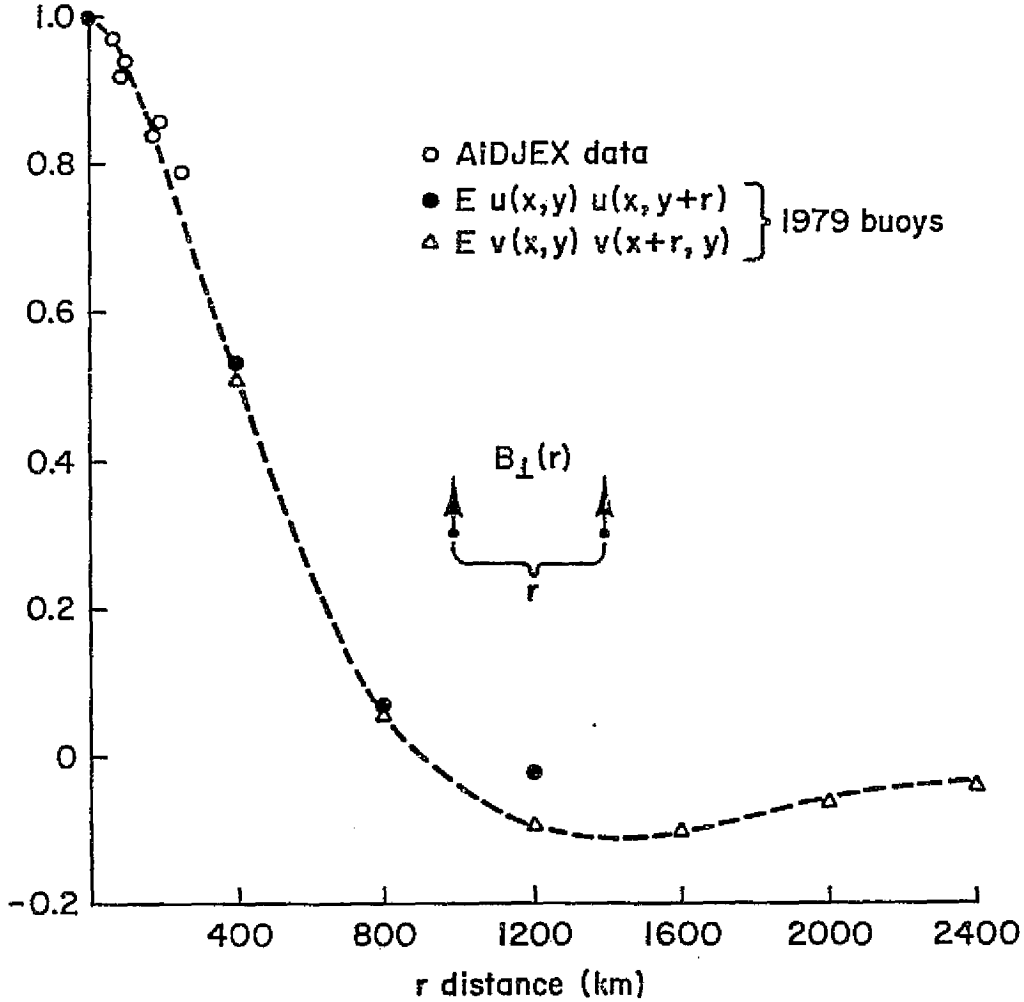

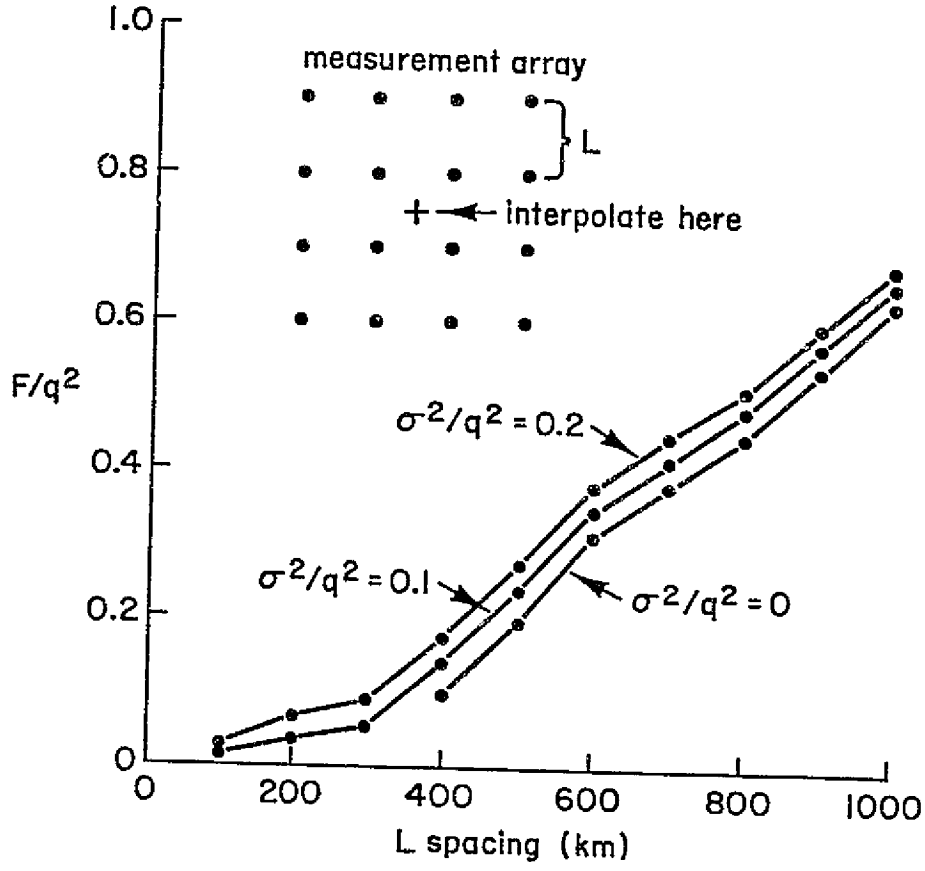

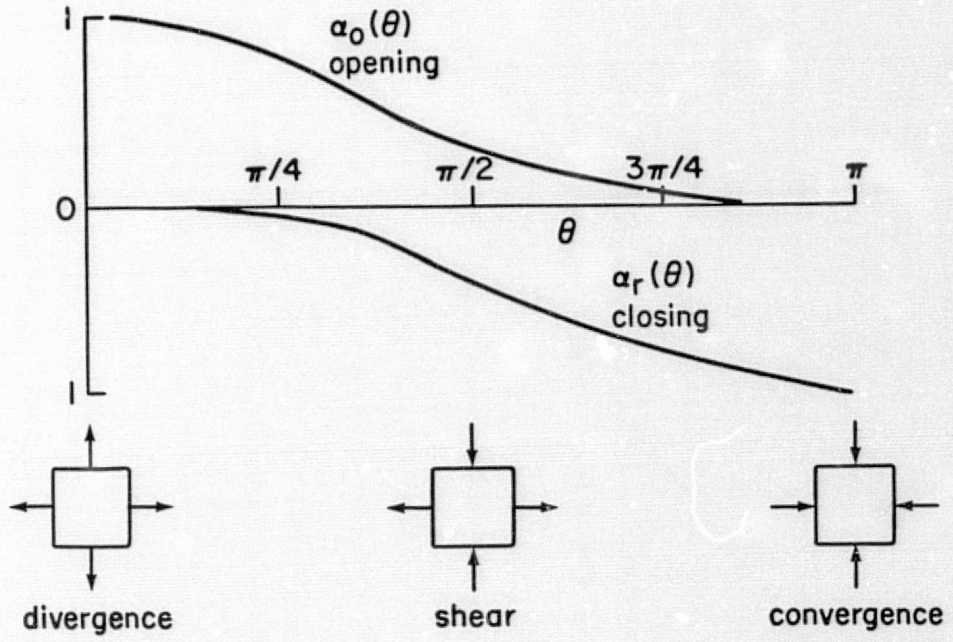

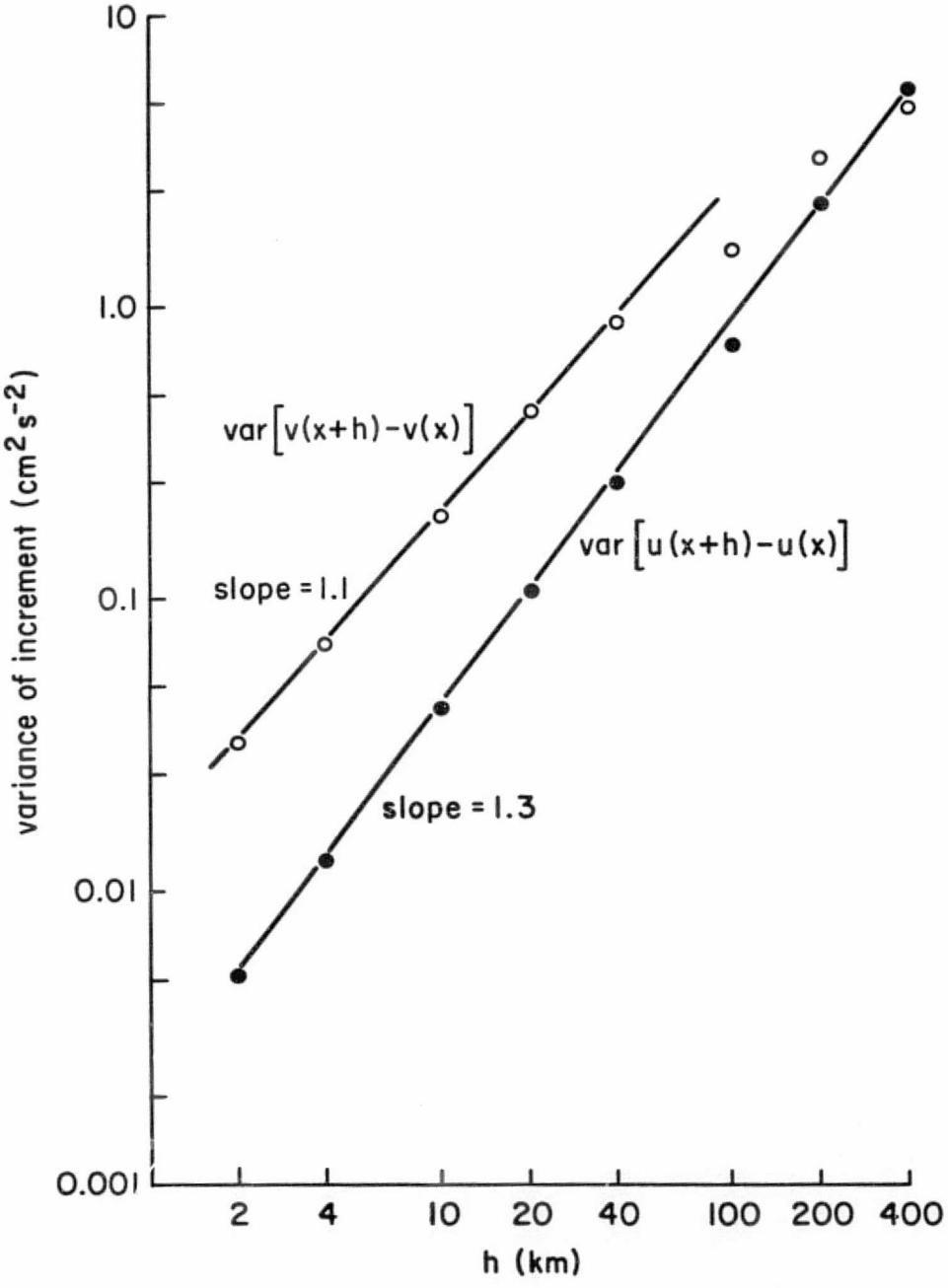

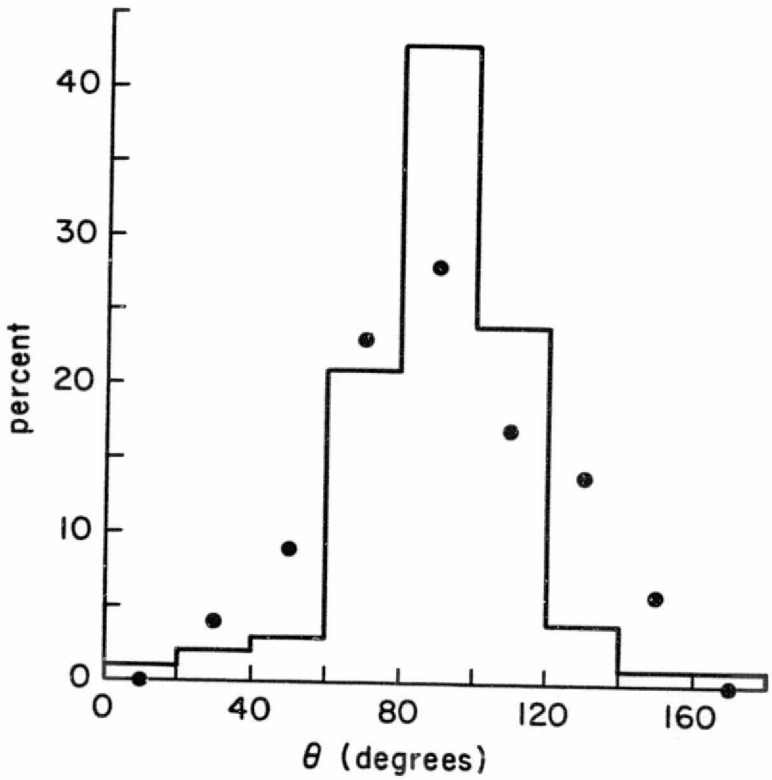

(a)

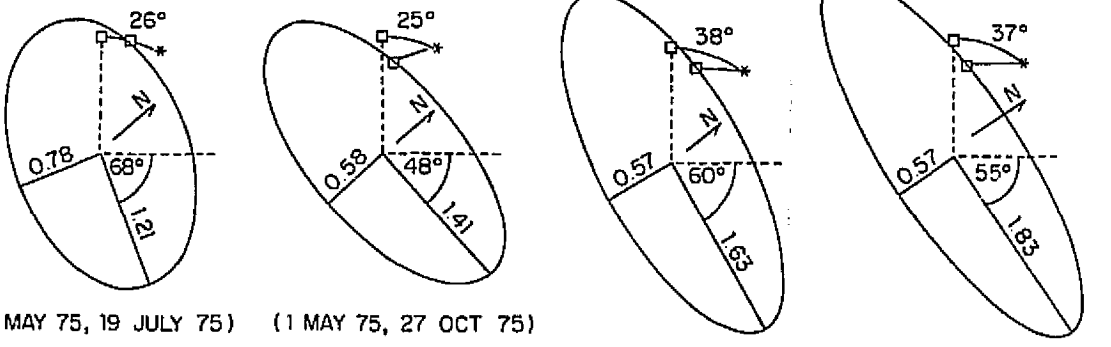

(1 MAY 75, 19 JULY 75) (1 MAY 75, 27 OCT 75) (1 MAY 75, 4 FEB 76) (1 MAY 75, 24 APR 76)

(b)

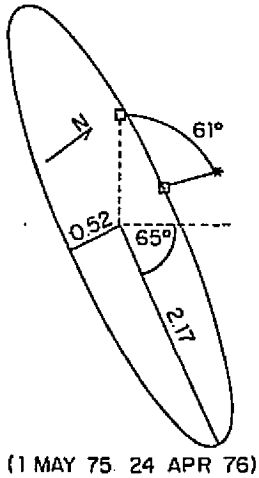

(1 MAY 75 24 APR 76)